Department of Physics and Astronomy

University of Heidelberg

Master thesis

in Physics

2017

submitted by

Thomas Theodor Rudzki

born in Villingen-Schwenningen

Commissioning and testing of large-area GEM-based readout chambers for the high-rate ALICE TPC

This Master thesis has been carried out by Thomas Theodor Rudzki

at the

Physikalisches Institut Heidelberg and GSI Helmholtzzentrum für Schwerionenforschung Darmstadt

under the supervision of

Prof. Silvia Masciocchi

Inbetriebnahme und Überprüfung großflächiger, auf GEMs basierenden, Auslesekammern für die ALICE TPC bei hohen Raten:

Diese Arbeit beschreibt die Inbetriebnahme und die Überprüfung der ersten zwei, auf GEMs (Gas Electron Multipliers) basierenden, Auslesekammern für das ALICE TPC Upgrade-Projekt, welche am GSI zusammengebaut wurde. Beide Kammern wurden auf die Homogenität des Verstärkungsfaktors und des Ionenrückflusses, die Energieauflösung und die Stabilität bei hohen Raten überprüft. Die Messungen der Homogenität zeigten, dass für beide Kammern die Verhältnisse von quadratischem Mittel zum Mittelwert des Signals unter der Obergrenze von 20 %, wie auch der Ionenrückfluss unter dessen Grenze von 1 % lagen. Es stellte sich heraus, dass der Einfluss des Strahleneintrittsfensters auf die Homogenität vernachlässigbar ist und eine Scanschrittweite von 25 mm und ein Kollimator mit $\varnothing = 10\,\mathrm{mm}$ für die Messungen am besten geeignet sind. Die Energieauflösung der ersten Kammer überschritt die Obergrenze von $\sigma_E/E \leq 12\,\%$, während die Auflösung der zweiten Kammer ungefähr bei dieser Grenze lag. Beide Kammern hielten Röntgenstrahlung stand, bei der der gemessene Strom an der Ausleseebene den Erwartungen für den Betrieb am LHC entsprachen. Zudem bestätigte eine Kammer ihre Stabilität, indem sie beim ALICE-Experiment nahe des Wechselwirkungspunkts betrieben wurde. Abschließend lässt sich sagen, dass sowohl das Testverfahren der Kammern etabliert wurde als auch die Funktionalität der zusammengebauten Kammern gezeigt werden konnte.

Commissioning and testing of large-area GEM-based readout chambers for the high-rate ALICE TPC:

This work presents the commissioning and testing of the first two GEM-based (Gas Electron Multiplier) readout chambers for the ALICE TPC upgrade project which were assembled at GSI. Both chambers were tested for their gain and ion backflow uniformity, energy resolution and stability at high rates. The uniformity measurements showed that the RMS/mean value of the signal was inside the limit of 20 %, likewise the ion backflow below the limit of 1 % for both chambers. It was found out that the influence of the entrance window on the uniformity is negligible and a scan step size of 25 mm and a $\varnothing = 10\,\mathrm{mm}$ collimator suit best for the measurements. The energy resolution of the first chamber exceeded the limit of $\sigma_E/E \leq 12\,\%$, while the resolution of the second one was around this limit. Both chambers sustained x-ray irradiation resulting in a pad current which is expected for the operation at the LHC. In addition, one chamber proved its stability placing it in the ALICE cavern close to the interaction point. In conclusion, the testing procedure of the chambers was well established and the assembled readout chambers proved their functionality.

Contents

I Introduction **7**

1 Physics motivation **8**
1.1 Quark-gluon plasma 8
1.2 Measuring the QGP 9
1.3 Phenomena of the QGP 9

2 ALICE experiment **10**
2.1 Detector system of ALICE 10
2.2 Measurement concept of ALICE 11
2.3 Limitations of the current ALICE TPC 13

3 Introduction to gaseous detectors and motivation for the ALICE TPC upgrade **15**
3.1 Particle properties 15
3.2 Drift chambers 16
3.3 Time Projection Chamber (TPC) 16
3.4 Multi-Wire Proportional Chambers (MWPCs) 18
3.5 Gas Electron Multiplier (GEM) 19
3.6 Applications of GEMs 20
3.7 Upgrade of the ALICE TPC readout chambers 21

4 GEM OROCs in the ALICE TPC **23**
4.1 GEM foil design 24
4.2 Readout chamber 26
4.3 Powering of GEMs 26
4.4 Gas mixture 28
4.5 Expected radiation 29

II OROC commissioning and testing **30**

5 OROC production flow **31**

6 GEM quality assurance **33**
6.1 Test procedure 33
6.2 Results 34

7 Gas tightness test **37**

8 OROC commissioning **39**
8.1 Powering via voltage dividers . . . 39
8.2 Charging up effect . . . 39
8.3 Bad segment survey . . . 40

9 Gain curve and energy resolution **44**
9.1 Gain curves . . . 44
9.2 Measuring method . . . 44
9.3 Gain curve of OROC/0 . . . 44
9.4 Gain curve of OROC/1 . . . 46
9.5 Voltage dependence of rate . . . 46
9.6 Energy resolution . . . 48
9.7 Measuring method . . . 49
9.8 Energy resolution of OROC/0 . . . 49
9.9 Energy resolution of OROC/1 . . . 51

10 Gain and ion backflow uniformity test **53**
10.1 Test setup . . . 53
10.2 Measuring method . . . 53
10.3 Gain uniformity measurements . . . 54
10.4 Absorption of x-rays in the testbox wall . . . 60
10.5 Simulation of the signal deterioration by the test box . . . 65

11 Irradiation test **71**
11.1 Test setup . . . 71
11.2 Measurement method . . . 73
11.3 Results . . . 73

12 Operation in the ALICE cavern **76**

13 Test beam campaign of an IROC **78**

III Conclusion **79**

14 Conclusion **80**
14.1 GEM quality assurance . . . 80
14.2 Test setup . . . 80
14.3 Floating Segments . . . 80
14.4 Energy resolution . . . 81
14.5 Gain and ion backflow uniformity . . . 81
14.6 Stability at high rates . . . 82

IV Appendix 83

A Appendix 85
A.1 Radioactive source 85
A.2 Specification of x-ray tube “Svetlana” 85
A.3 Specification of x-ray tube “Mini-X” 85

B Bibliography 87
B.1 List of Figures 90
B.2 List of Tables 92

Part I

Introduction

1 Physics motivation

1.1 Quark-gluon plasma

The experiments at the LHC at CERN focus on testing properties and limits of the Standard Model of Particle Physics. ALICE – A Large Ion Collider Experiment – is specialized on the study of the quark-gluon plasma (QGP) and the strong interaction. The QGP is a state of matter which forms at extremely high energy densities of at least $1\,\mathrm{GeV/fm^3}$ [1]. For comparison, the average density of nuclear matter is around $0.2\,\mathrm{GeV/fm^3}$. At this high energy scale, the coupling of the strong interaction is decreased and quarks and gluons start to behave as asymptotically free particles. Thus, the medium is believed to be deconfined with the consequence that its constituents carry color-charge. At lower energies, however, quarks are not freely moving but bound to color-neutral pairs or triples forming hadrons like nuclear matter. At the LHC, the QGP is generated in Pb-Pb collisions at ultrarelativistic energies. Heavy-ion collisions with a centre-of-mass energy in the TeV range per nucleon pair create a fireball with sufficiently high energy density.

The lifetime of the QGP in experiments at the LHC is very short, around $10 - 20\,\mathrm{fm}/c_0$ [2]. This time and the resulting length scale can not be resolved by any experiment. Once created, the QGP is expanding and thus cooling down (Fig. 1.1). Lattice calculations estimate that atthe critical temperature of 154(9) MeV the QGP undergoes a phase transition from deconfined to confined matter, a process called hadronization [3].

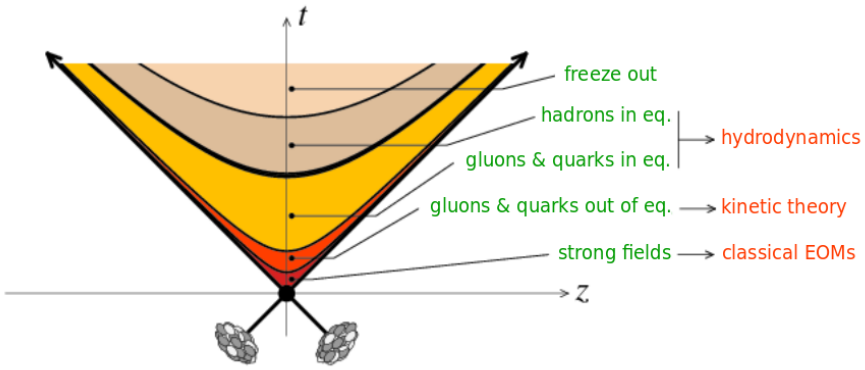

Figure 1.1: Schematic illustration of the collision of two nuclei in space-time picture [4].

1.2 Measuring the QGP

There are many challenges to approach measuring properties of the QGP. First of all, the Pb-Pb collisions at the LHC provide a very high multiplicity of particles which have to be detected. At a collision energy of $\sqrt{s_{NN}} = 5.02\,\text{TeV}$ typically around 2,000 particles are created in the 5 % most central collisions [5]. To study the QGP, the properties of these particles have to be determined. Thus, the detectors for such a heavy-ion experiment have to be characterized by high granularity and a good particle identification. The ALICE experiment has an optimized setup to meet these challenges. In contrast to the ATLAS and CMS experiments, which established in the meanwhile an own heavy-ion program, ALICE stands out due to its coverage of the low transverse momentum p_T regime down to 150 MeV/c because of a low magnetic field and the strong ability of particle identification [6]. Details of the ALICE detectors will be discussed in the next chapter.

1.3 Phenomena of the QGP

The open question is now: what are the fundamental properties of QCD matter and what happens in the QGP and how is this related to measurable observables?

The major difference between a regular p-p and a Pb-Pb collision forming a QGP is that in the second case there is a medium and particles formed in the collision are interacting with it. This medium is ruled by the strong interaction via gluons. Depending on the binding energy, this implies that created quark anti-quark pairs might not "see" each other because of color screening and form no bound states. High-momentum partons coming from hard parton-parton collisions can loose a significant amount of their energy to the medium via interaction. This results in the expectation that the momentum distribution of particles differs for the two collision types.

For Pb-Pb collisions, an enhanced production of strangeness is observed due to the higher energy density. The appearance of heavy quarkonia like J/ψ ($c\bar{c}$) and Υ ($b\bar{b}$) is influenced by the QGP such that it is suppressed due to color screening. However, for sufficiently high energies, like the ones provided by the LHC, the number of produced charm quarks is increased such that the probability to form J/ψ is enhanced again [7]. The occurrence of these heavy-flavor particles is accessed by the measurement of their decay products, like the decay to two leptons, one example why particle identification is so important.

The high-momentum partons, mentioned before, can result in jets consisting of a directed set of hadrons. These jets are usually coupled to a partner jet or a high-energy photon in opposite direction balancing the tranverse momentum distribution. The partons responsible for jets can loose large parts of their momentum in the medium. This results in so called jet quenching whose strength is correlated to the density of the medium [8]. The quenching can be quantified by triggering on jets or high-energy photons and measure the occurance and energy of the opposing jet.

2 ALICE experiment

ALICE, A Large Ion Collider Experiment, is an experiment located at the Large Hadron Collider (LHC) at CERN (Fig. 2.1). The LHC is an accelerator at the border between Switzerland and France, close to Geneva. With its circumference of 27 km and collision energies of 13 TeV, it is currently the largest and most powerful collider in the world. ATLAS, CMS, LHCb and ALICE are the four major experiments at the LHC. In contrast to the other three experiments, ALICE focuses mainly on physics of heavy ions.

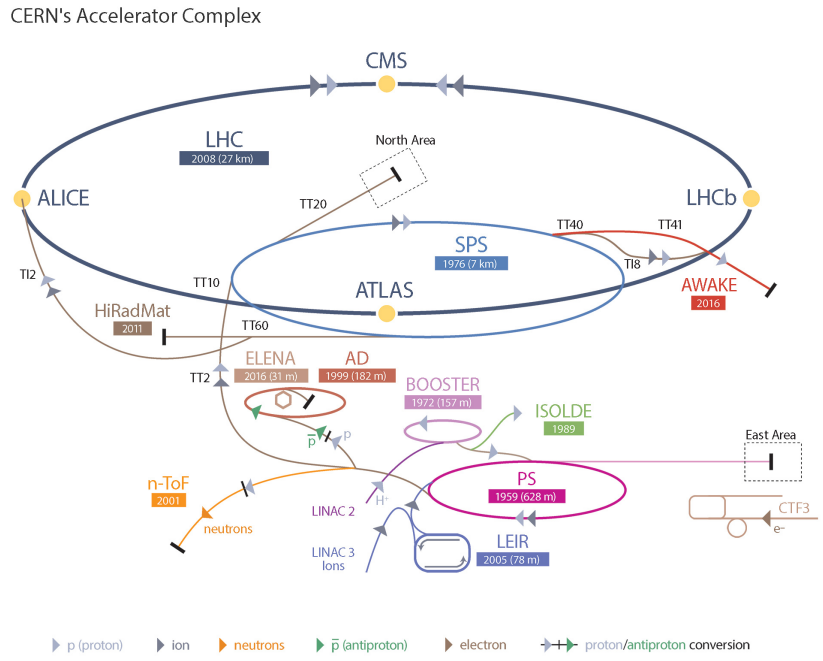

Figure 2.1: CERN accelerator complex [9].

2.1 Detector system of ALICE

The ALICE experiment consists of many different detectors. Each of them has specific functions to measure the products of the collisions. In Fig. 2.2 the structure of the experiment is displayed.

Most of the detectors are surrounded by the red L3 solenoid magnet providing a magnetic field of 0.5 T. Those are arranged in barrel-like manner around the beam pipe. The Inner Tracking System (ITS), consisting of two layers of silicon pixels,

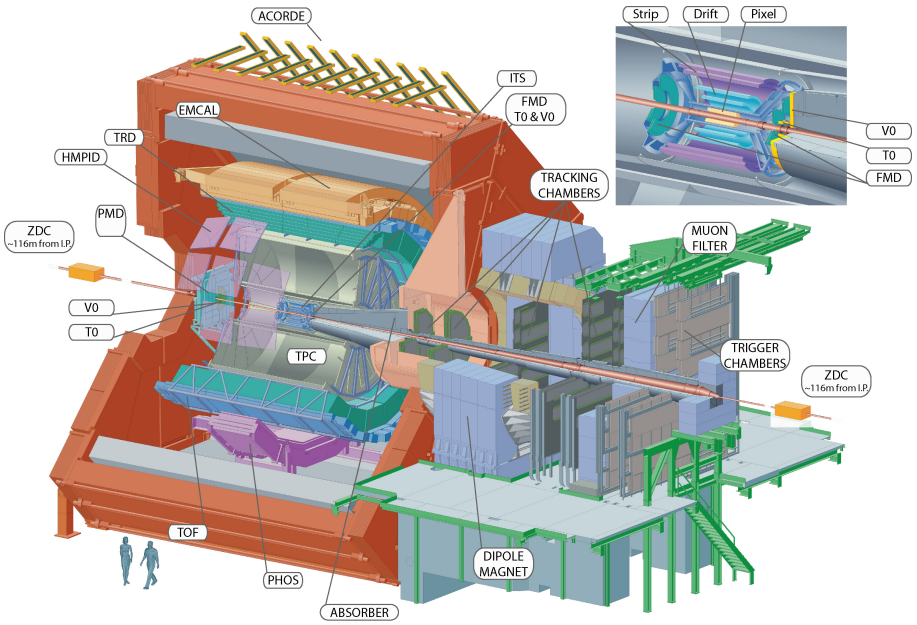

Figure 2.2: The ALICE detector system [10]

two layers of silicon drift detectors and two layers of double sided microstrips, forms the innermost system of ALICE. In forward and backward direction, there are the so called Forward Detectors (FWD): T0, V0 and FMD. These Cherenkov, scintillation and silicon strip detectors provide trigger and multiplicity information [11]. The ITS is followed by the Time Projection Chamber (TPC) and the Transition Radiation Detector (TRD). On top of the TRD, Time Of Flight (TOF) and a High Momentum Particle IDentification (HMPID) detectors are mounted. The last layer consists of the two calorimeters PHOS and EMCAL. Next to the magnet, a set of tracking and trigger chambers for muon detection at forward rapidity is placed (right side of Fig. 2.2).

2.2 Measurement concept of ALICE

ALICE is meant to study the QGP and the strong interaction. As outlined in the physics motivation, heavy-ion collisions with a resulting density of $1\,\mathrm{GeV/fm^3}$ are sufficient to form a QGP. The effects and the behavior of this state of matter are analyzed by comparing it to proton-proton collisions with equal center of mass energy per nucleon serving as reference measurements.

The major task of the detectors of ALICE is the reconstruction of particle tracks and identification of particles in a very high particle density environment. The tracking system of ALICE relies on the TPC and is complemented by the Inner Tracking System (ITS) and the Transition Radiation Detector (TRD). The TPC serves also as a main component for particle identification. The strong ability for particle identification and the coverage of low momentum particles down to $150\,\mathrm{MeV/c}$ due to

the low magnetic field are the unique features of the experiment at the LHC.

There are several possible methods for particle identification. One example is the energy loss of particles visualized by the PID plot of the TPC (Fig. 2.3). The energy loss dE/dx described by the Bethe-Bloch formula (2.1) differs for the particle species at same momentum due to their difference in the relativistic velocity β which is related to the particle masses.

$$-\frac{dE}{dx} = \text{const.}\ \frac{z^2}{\beta^2} \cdot \left[\ln\left(\text{const.}\ \frac{\beta^2}{(1-\beta^2)}\right) - \beta^2\right] \tag{2.1}$$

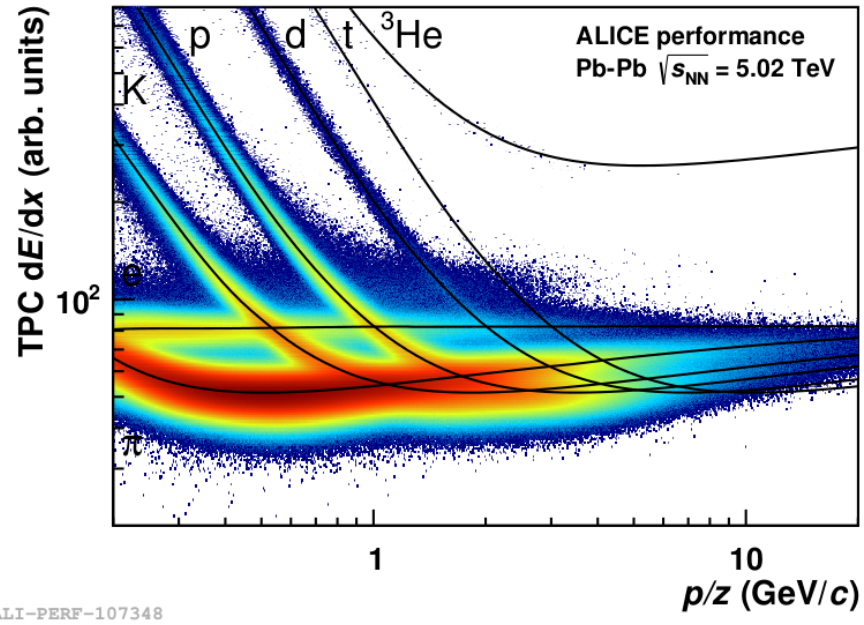

Figure 2.3: Particle Identification by the energy loss dE/dx in the ALICE TPC [12].

However, in case of crossing points of the curves or in the high-momentum regime, the discrimination via energy loss is not unambiguous. For better distinction of particles species in these regions, other PID detectors come into play. The TRD can distinguish directly electrons from pions since, in contrast to heavier particles, electrons produce transition radiation in the detector. In turn, pions and kaons can be distinguished by TOF measurements.

The experiment has several different modes of data taking. On the one hand, data taking can be performed without preselection of events. This mode is called minimum bias and records basically all kinds of collisions only restricted to the availability of the detectors and the limitation of the bandwidth for data transfer. On the other hand, a selective data taking mode is sustained using triggers. This implies that only events that fulfill specific characteristics are recorded. This selection is useful for certain physics questions where only distinct event structures are interesting. Examples for these triggers are the TRD, EMCal, muon and high-multiplicity

triggers. The TRD trigger can be used to select high-momentum electrons, nuclei or jets. High-momentum electrons, for example, are indicators for J/Ψ decays or other heavy-flavor particles. The EMCal can trigger for photons and jets above a certain energy threshold. The muon trigger is self-explanatory triggering for muons in an event. High-momentum muons produced in the collision are not affected by the strong interaction and can thus provide information about the early stage of the collision. The high-multiplicity trigger requires a certain amount of signals (firing pixels) in the Silicon Pixel Detector of the ITS and the V0 detector. High-multiplicity events are interesting for p-p collisions to investigate if the energy density can be sufficient for collective effects which can be observed in Pb-Pb collisions [6].

At the LHC, proton-proton campaigns occupy most of the LHC running time. The ALICE experiment uses them as reference measurements for the heavy-ion collisions since it is not expected that the energy density is sufficient enough to create a QGP. In addition, there are p-Pb collisions which investigate the behavior of single nucleons in a collision with heavy ions. They serve as a reference for Pb-Pb collisions and study cold nuclear matter effects like the modification of the parton distribution functions of nucleons inside a nucleus [13]. For the referencing, it is important that the collision energies per nucleon-nucleon pair are equivalent. In the current Run 2, there were Pb-Pb collisions with $\sqrt{s_{NN}} = 5.02\,\text{TeV}$ in 2015 at collision rates up to a few kHz.

2.3 Limitations of the current ALICE TPC

The TPC of the ALICE experiment (Fig. 2.4) is a central barrel detector that is filled with Ne-CO_2-N_2 (90-10-5). The sensitive volume covers $84.8\,\text{cm} < r < 246.1\,\text{cm}$ in radial and $\pm 250\,\text{cm}$ in z-direction [14]. Thus, with a volume of around $90\,\text{m}^3$, the ALICE TPC is the largest gas filled TPC in the world. On each side 18 outer (OROCs) and 18 inner (IROCs) readout chambers are mounted. The readout chambers are equipped with multi-wire proportional chambers (MWPCs) which have a limited readout rate of around 3 kHz.

From 2021 onward, the LHC will provide Pb-Pb collisions with rates up to around 50 kHz. This results in a possible integrated luminosity of $10\,\text{nb}^{-1}$ for Run 3 compared to 1-2 nb^{-1} expected in Run 2 [15]. The ALICE experiment has to be upgraded to cope with these high rates. In particular, the TPC is the rate limiting component with its limited readout rate. Thus, the current chambers will be exchanged by Gaseous Electron Multipliers (GEMs) which will be a topic of the next chapter (Section 3.7).

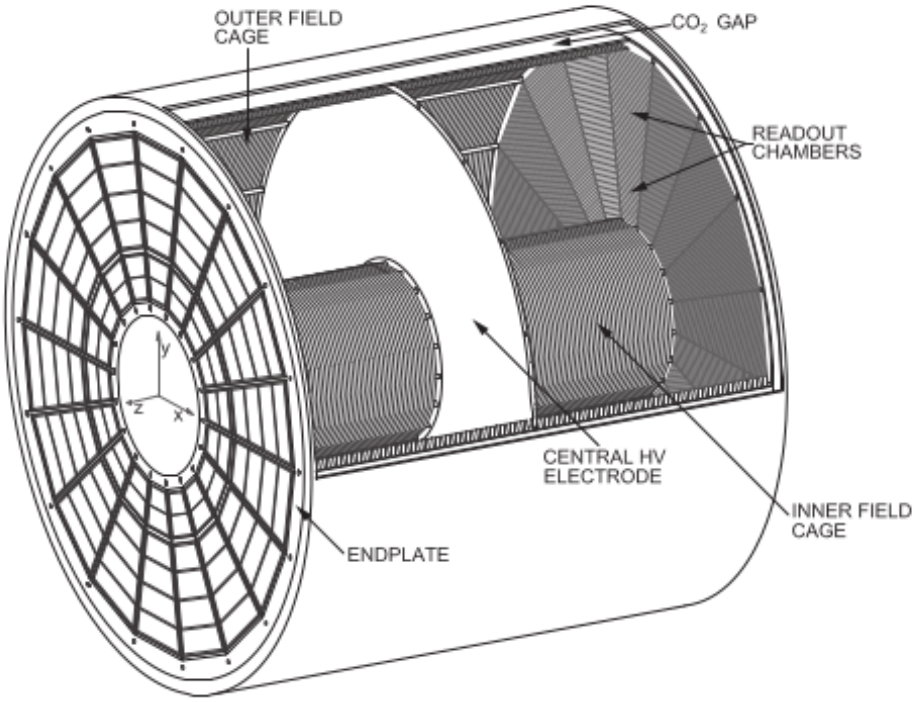

Figure 2.4: Schematic view of the ALICE TPC [14].

3 Introduction to gaseous detectors and motivation for the ALICE TPC upgrade

In the previous chapter, the upcoming upgrade of the ALICE TPC was introduced. The basics of the relevant gaseous detector types and details of the upgrade are the main topic of this chapter.

In a TPC, charged particles can be detected exploiting the fact that, when traversing its gas volume, they ionize its molecules and produce ion-electron pairs along their trajectory. The liberated charges are guided by an electric field and collected by the readout electronics of the detector.

3.1 Particle properties

In heavy-ion as in particle physics experiments the relevant observables are characteristics of the produced particles from a collision. This includes their momentum, mass, charge velocity and lifetime. In some cases, the obtained informations are sufficient to explicitly recover the particle identity.

In gaseous detectors which are operated in proportional mode[1], the energy loss is directly accessible via the number of produced ionization clusters. In combination with a homogeneous magnetic field of strength B the momentum p of charged particles can be recovered by reconstructing the curved track since the curvature R is linearly dependent on the momentum:

$$p_T = 0.3 \; z \; B \; R; \quad p = \frac{p_T}{sin(\theta)} \tag{3.1}$$

where z is the particle electric charge, p is the full and p_T the transverse momentum in GeV/c and θ the inclination angle of the track.

The velocity of a particle is obtained by measuring at least two time signals at points as far as possible from each other to minimize the influence of the resolution. The lifetime determination, in turn, requires either complete tracking data to identify the location of the particle decay or, for short living particles like B mesons, the ability to find secondary vertices close to the interaction point by backtracking the decay products.

[1] Range in which amplified signal is proportional to primary charge corresponding to a gain $\approx 10^3 - 10^5$ [16].

3.2 Drift chambers

A special kind of gas detector is the drift chamber. The thesis focuses on presenting this subcategory because it is the foundation of the detector (ALICE TPC) related to this work. A drift chamber is a detector which detects particles by recording the drifting electrons that were released by ionization. In general, drift chambers are divided in two main parts: In the first one – the drift volume – the signal generation takes place via ionization of the gas by charged particles. The liberated electrons from the ionization are moving in an electric field to the second part – the readout – where the electron signal is amplified and readout by wires and pads.

The drift volume of drift chambers is rather similar for different types of applications. The electric field is kept homogeneous such that the drifting electrons are not deflected on their way to the readout. This can be supported e.g. by a field cage around the gas volume. Thus, large sensitive detector volumes can be realized.

At the readout, dense electric fields are required to amplify the drifting charge, therefore here the field is no longer homogeneous. For this reason, a grid can be installed in the intermediate region that shields the drift region and shapes the field lines In the amplification process, ions and electrons are released in equal amounts. The ions will move in opposite direction back to the drift volume. This space charge accumulation should be prevented for large sensitive volumes with long drift times which can be achieved likewise by a grid. The signal amplification can be achieved by several methods. The most common are charged wires, either arranged in a grid or for small applications individually placed, focusing many field lines. There are also approaches using micro-pattern technologies like thin foils with holes of several µm [16].

In the next part, the focus shifts to a very specific drift chamber, namely the Time Projection Chamber.

3.3 Time Projection Chamber (TPC)

A Time Projection Chamber (TPC) is a special kind of drift chamber for three-dimensional reconstruction of particle tracks. It was developed in the 1970's to record multiple particle tracks and first operated in the PEP4 experiment at the PEP[2] storage ring [16].

In a TPC, the drift part is a large cylindrical or ashlar-formed gas volume surrounded by a field cage and divided by a central electrode in the middle. This is followed by endplates serving as the readout part (Fig. 3.1). The particles coming from the interaction point enter the gas volume and leave a track of ionized gas molecules and electron pairs. The ions are extracted by the central electrode while the electrons move to the endplates where the signal is first amplified, then recorded.

[2] **P**ositron **E**lectron **P**roject: electron positron collider with a center-of-mass energy of up to 29 GeV at SLAC (Stanford Linear Accelerator Center), California.

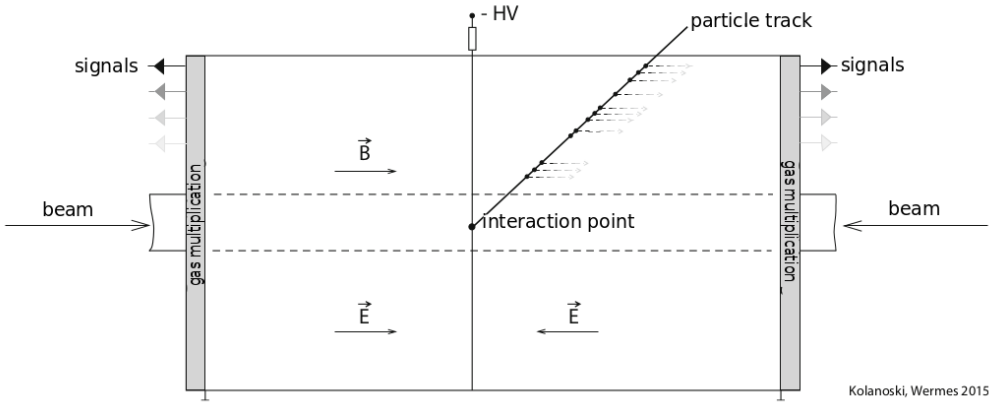

Figure 3.1: Schematic representation of a TPC. An exemplary particle coming from the interaction point traverses the gas volume ionizing it. The released electrons move to the endplates where the signal generated after gas multiplication. (Adopted with kind approval from Kolanoski and Wermes [16]; notes translated by the author)

The three-dimensional information is extracted on one hand by the location of signal generation. This corresponds to the original x- and y-position of the track since the electrons move straight to the readout plane. On the other hand, the z-position of the ionization point is obtained by the drift time information of the signal. To this scope, the start time information is provided by the collision itself. A three-dimensional reconstruction of the tracks can be computed. In addition, the amplitude of the signals can be recorded, which is proportional to the energy deposit of the particle along the ionization path. The measurement of the particle momentum with the magnetic field which surrounds the TPC is performed by measuring the radius of curvature of the track. This provides information about the particle identity (Section 3.1). The TPC provides a high granularity necessary to detect particles in high-density environments and reconstruct their trajectories also in high-multiplicity events. All individual tracks can be detected individually as long as they can be separated by the resolution power of the detector. For high-rate applications a central problem of the TPC are the long drift times in the often meters long drift regions [16]. The electrons drifting toward the amplification region need around 40 µs per meter. However, the ions created in the amplification region have a much lower velocity. They need about 60 ms to pass a distance of 1 m, in case of Ne[3] and a drift field of 400 V/m [14]. This leads to space-charge accumulation in the drift region that distorts the drifting electrons.

The natural limits of a TPC are therefore:

1. Granularity of the readout to distinguish close tracks.
2. Ion mobility or ion blocking affects rate capability.

[3]For comparison: the drift velocity of Ar is more than a factor 2 lower for this drift field [17].

In the following sections two different readout technologies for the TPC will be presented: the most common Multi-Wire Proportional Chambers (MWPCs) and the upcoming Gas Electron Multipliers (GEMs).

3.4 Multi-Wire Proportional Chambers (MWPCs)

The MWPC was invented in the 1960's by George Charpak at CERN [18]. He was later honored for his work on particle-detector development with the Nobel prize in 1992.

The readout of a MWPC consists of many parallel wires kept under high voltage. The electrons, released by ionization in the drift region, drift toward the closest wire. In its vicinity, they get accelerated and signal amplification takes place. The wires are usually operated in the proportional region of gas multiplication. The signal is produced either by the charge collected at the wire or by the signal induced by the charge cloud at a pad plane. In the second case the image charge is distributed over several pads, increasing the spatial resolution since the center of gravity method can be used [16].

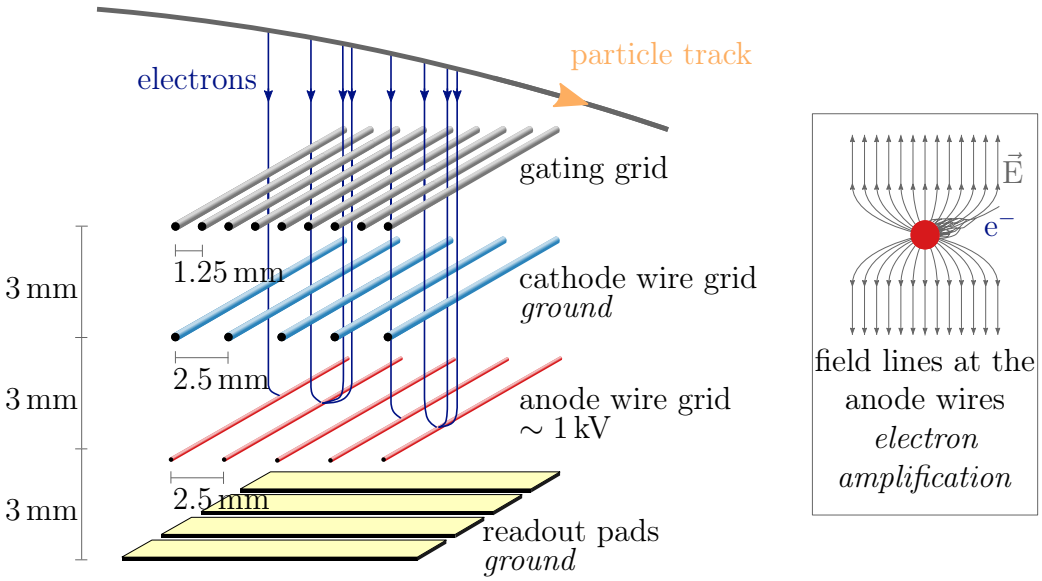

Figure 3.2: MWPC based readout of an OROC in the ALICE TPC. In an IROC the distance between pads and anode wires, as well as between anode and cathode wires is reduced to 2 mm. (Adopted with kind approval from Julius Gronefeld)

In case of MWPCs used for the readout in a TPC an intrinsic problem of the MWPCs shows up. The amplification process yields the same amount of ions as electrons. The ions are drifting back into the volume toward the cathode. The field inside the drift volume can be distorted by the accumulated space-charge in this way. In order to avoid this problem, a gating grid is inserted in the TPC. This is an

additional wire plane placed between the drift and the amplification regions. These wires help to focus the field such that the electrons drift to the anode wires as long the ionization and the drift of electrons takes place. During amplification the gating grid gets activated by applying a negative voltage to absorb the back flowing ions. All created signals in the TPC are not recorded in this time since also the electrons can not enter the amplification region. Therefore, the TPC is blind. The induced dead time strongly depends on the ion mobility in the gas which is typically in the region of $\mathcal{O}(1\,\mathrm{cm/ms})$.

In high-rate experiments, the dead time caused by the gating grid is a downside but it makes the detector operable at all since no space charge is accumulating in the drift volume. In an experiment where the dead time is no longer acceptable, another readout technology should be considered since opening the gating grid would cause deviations in the spatial resolution of several cm in a TPC (Section 3.7).

3.5 Gas Electron Multiplier (GEM)

GEMs, Gas Electron Multipliers, serve in gas detectors as amplification system. They are ∼50 µm thin kapton foils which are covered on both sides with a copper layer, into which small holes are etched with a density of 50-100 mm^{-2} (Fig.3.3(a)).

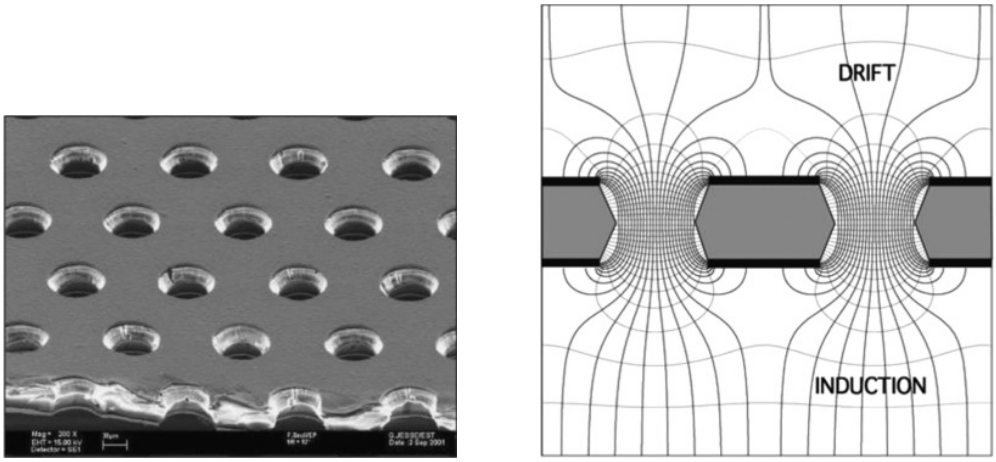

(a) Electron microscope image of a cut GEM with 50 µm thickness, 70 µm hole diameter and 140 µm pitch [19]

(b) Schematic representation of the electric field in the holes of a GEM foil [19].

Figure 3.3: Electrical field inside GEM holes and a microscope image of a cut GEM

GEMs were originally developed by Fabio Sauli in 1997 to serve as preamplifiers for the electron signal to decrease the gain below the critical level for discharges [19]. In particles physics, GEMs can be applied as full amplification system in drift chambers to detect high-momentum particles which are ionizing the gas molecules in the drift gas. The released electrons drift in a strong electrical field toward the foils. The

amplification process occurs inside the holes of the foils due to a potential difference of a few 100 V that is applied between the copper layers resulting in a strong field inside the holes (Fig. 3.3(b)).

The electrons gain energy by acceleration inside the field. In collisions with gas molecules further electrons are released. In a safe operating mode with moderate potentials, the ionization cascade inside one foil releases typically 5-7 electrons per incoming electron. This is a comparable low number comparing single GEMs to other amplification techniques in detectors. For efficient detection of electron clusters and precise location of the charge, a much higher amplification factor is necessary. This is obtained by stacking multiple GEMs. The amplification cascade which is started in the uppermost foil is then continuing through the underlying foils. This method enables a gain of the order of few 1,000 using three or four foils and simultaneously keeping the voltages on a moderate level. The comparable low voltages and the diffusion inside the stack reduce the local charge density, which could lead to a streamer shorting the two sides of the GEM, and therefore the probability of destructive discharges.

3.6 Applications of GEMs

To understand and follow the planned operation mode of the GEMs in the ALICE experiment, different forms of GEM detectors are presented.

Single photoelectron detection

GEM foils can be used to detect single photoelectrons in a Ring Imaging Cherenkov (RICH) detector. In a set-up where the uppermost GEM is coated with CsI serving as the photocathode, the released photoelectron is extracted by the GEM hole due to its high surface field. Low drift fields prevent ion and photon feedback as well as direct ionization in the gap.

There were prototype studies for a gaseous Cherenkov detector filled with CF_4 (refractive index: n = 1.0004823) for the Electron Ion Collider (EIC) using quintuple GEM stacks. Primary charges coming from charged tracks are rejected by a reverse bias. This setup aims for particle identification up to a momentum of 50 GeV and relies on the detection of a small number of Cherenkov photons created in the dilute medium [20].

COMPASS tracking detectors

In the COMPASS[4] experiment, GEM detectors are employed as tracking devices in a fixed-target experiment at the Super Proton Synchrotron (SPS). The experiment itself requires low material budget, because the deflection and deceleration of traversing particles should be kept to a minimum, and a dead-time free operation

[4] **CO**mmon **M**uon and **P**roton **A**pparatus for **S**tructure and **S**pectroscopy, located at CERN.

of all devices due to the high rate of $\sim 10^8$ particles per 5 s spill. The GEM chambers are built with a triple GEM configuration providing an almost discharge-free operation. The sensitive gas volume is 3 mm thick where the incoming particles are ionizing the gas. The GEM stack is amplifying this signal providing information about the x- and y-position of the track. The chambers are constructed such that each results in a radiation length of 0.7 % [21].

ALICE TPC

The ALICE TPC will be equipped with GEM readout chambers after the next upgrade. The setup is optimized for good energy resolution to allow particle identification and for a low ion backflow since the drift volume is very large. It will use quadruple GEM stacks with a high amplification in the last two foils to absorb the ions on their way through the stack [14]. The details of this application are discussed in the next section.

3.7 Upgrade of the ALICE TPC readout chambers

The ALICE TPC and its limitations were already introduced in Section 2.3. The interaction rates in Run 3 in Pb-Pb collisions will increase to 50 kHz and a continuous readout of the ALICE experiment is planned. which is not supported by a readout concept using MWPCs in combination with a gating grid.

To extend the rate capability, a naive approach would be to keep MWPCs without gating grid and to handle the distortions caused by space charge accumulating in the drift region by data processing. This scenario was tested in Run 2 (p-p collisions, 200 kHz) by taking data with an opened gating grid. The induced radial distortions were of the order of 10 cm, in the innermost region up to 20 cm [22]. Additionally, those distortions are not uniformly distributed and can fluctuate strongly. The higher luminosity in Run 3 will further aggravate this problem. This implicates that the MWPC as readout for a high-rate TPC is inadequate because for its functionality the gating grid is crucial. For this reason, opening the gating grid had to be excluded as solution for the rate capability problem.

This led to the necessity of a new readout system that can handle high particle rates, offers intrinsic ion blocking and comparable performance for the energy resolution and signal uniformity. In particular, the ion feedback is a complex topic since the electrons should enter the amplification region but ions should not escape. The problem is approached by a quadruple GEM detector tuned for a sufficient gain and a reduced transparency for back flowing ions. Studies with $10 \times 10\,\mathrm{cm}^2$ prototypes of GEM detectors revealed that quadruple GEM stacks can maintain the main properties of the MWPCs and provide a sufficiently low ion backflow of the order of 1 %. The space-charge distortions in radial and azimuthal direction using GEMs in Run 3 are expected to be comparable to those in Run 2 with opened gating grid, mentioned before [14]. By now, deviation of this size can be corrected which

enables the operation of a high-rate TPC at the LHC. According to that, a GEM based readout achieves the requirements of the previous readout chambers while accomplishing the aim to be operated in the high-luminosity LHC.

4 GEM OROCs in the ALICE TPC

The new GEM-based OROCs for the ALICE experiment resemble the old MWPC OROCs. The readout chambers will have the same size since they will be mounted inside the same frame of the TPC. During the Long Shutdown starting in 2019, the TPC will be taken out of the ALICE cavern, to the surface, and disassembled in a clean room. The old chambers will be one-by-one replaced by the newer ones.

The consequence of the barrel shape of the TPC is that the chambers have a trapezoidal shape to arrange them in a circle at the endplates of the TPC. Whereas for the IROC a GEM is roughly 400 mm long and between 280 mm and 460 mm wide to cover the area, the length of an OROC is 1000 mm and the width 460 mm to 800 mm [14]. This area could not be covered by a single stack of GEMs only considering the tension which would has to be applied on the foil to avoid sagging. The solution is to divide the area of the OROC to three parts called OROC1-3 (Fig. 4.1). In each area an individual GEM stack of four foils is mounted. The characteristics of the foils are described in the following section.

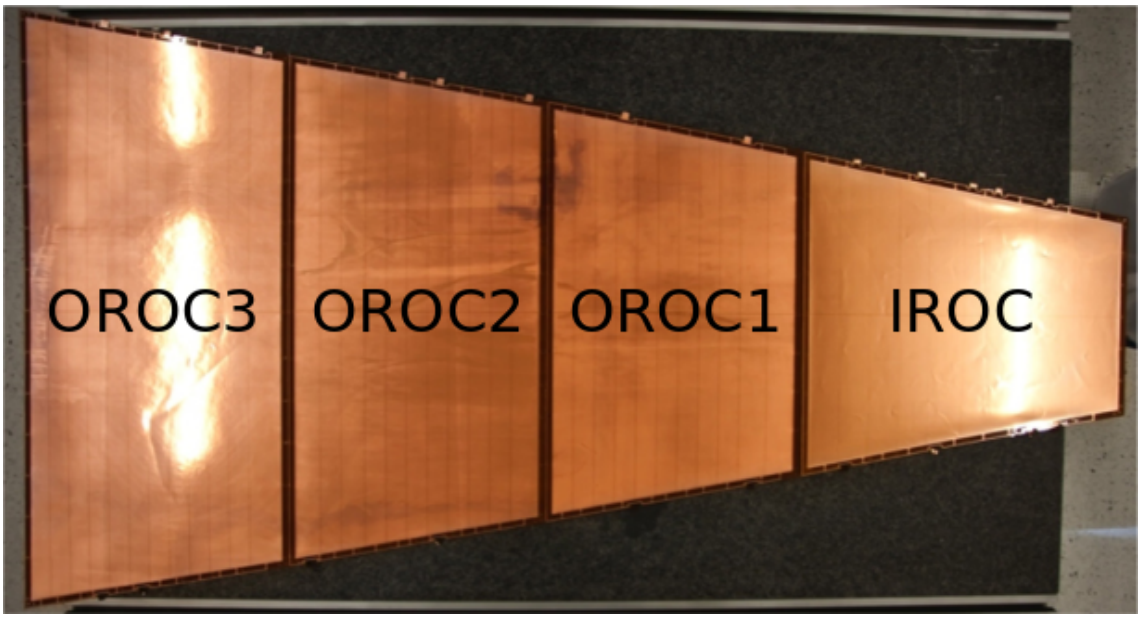

Figure 4.1: One full sector of the ALICE TPC (IROC and OROC) is equipped by four GEM stacks. [15].

During this thesis, two OROCs were mounted and tested at GSI. The first one had some minor difference from the final design and is referred to as OROC/0 or EDR OROC. The second chambers was already of final design and all foils underwent the full QA procedure. It is referred to as OROC/1 or PRR OROC.

4.1 GEM foil design

The GEM foils used for the TPC upgrade project have several common characteristics:

- foil thickness (50 µm Polyimide foil + 2-5 µm Cu layer on both sides)
- hole diameter (inner diameter ∼50 µm; outer diameter ∼70 µm; Fig. 4.2)
- one side (facing the drift volume) electrically divided in ∼100 cm^2 segments (Fig. 4.3)
- segments are connected to HV supply by a HV path over a resistor of 5 MΩ (Fig. 4.4)

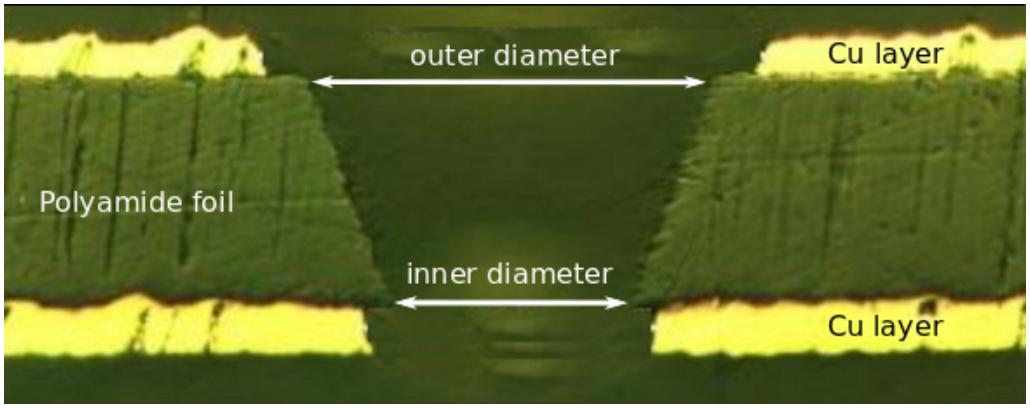

Figure 4.2: Cross section of a GEM foil where holes are etched with single-mask technique.

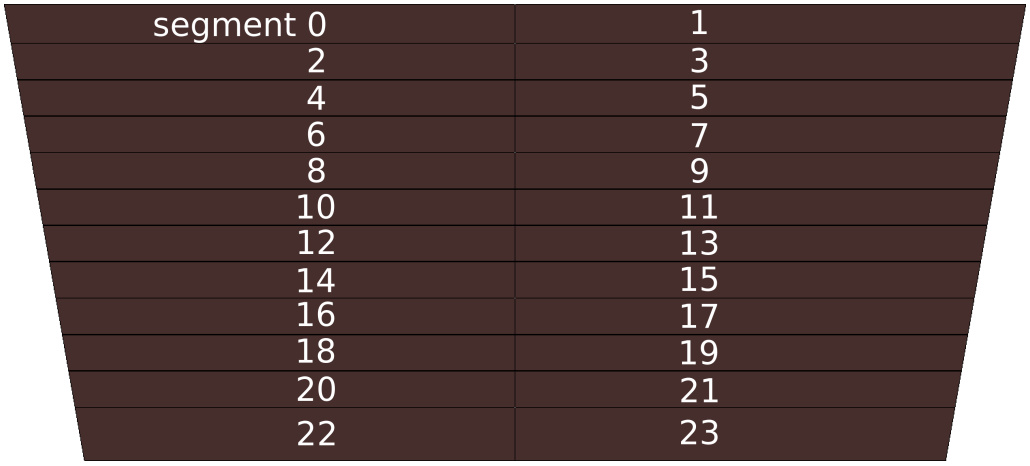

Figure 4.3: Segmentation of a OROC3 foil into 24 segments.

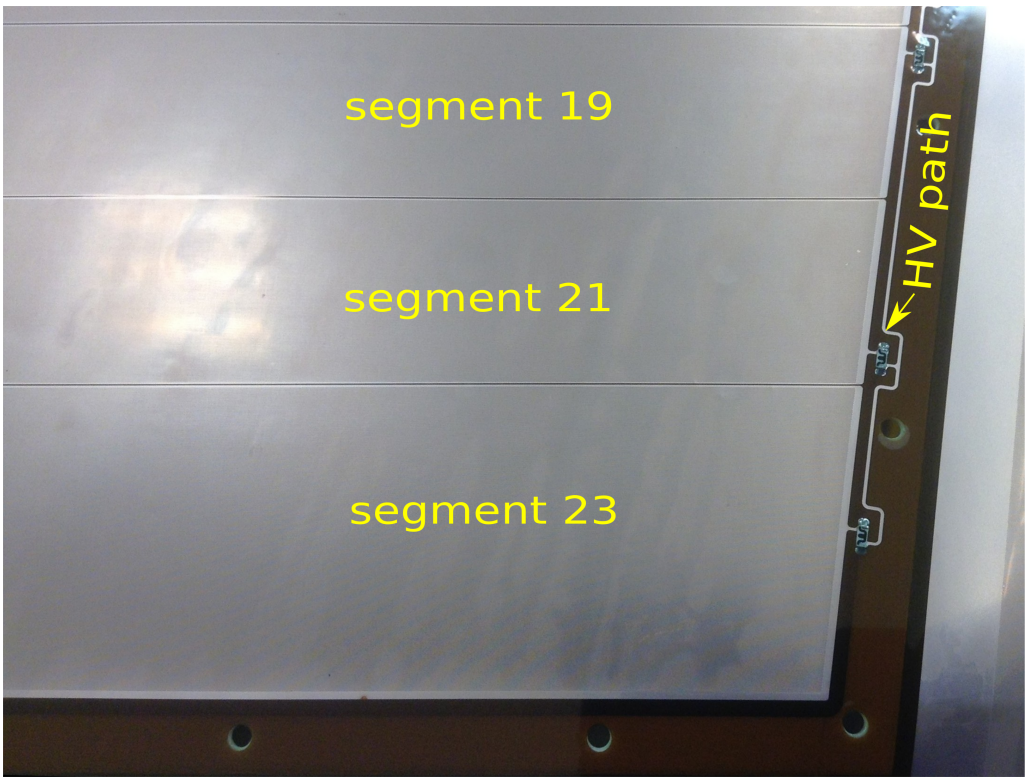

Figure 4.4: Part of segmented side of GEM foil of an OROC3 stack (3 of 24 segments partly visible). On the right side the HV path connected by resistors is visible. The supporting frame is adumbrated under the Kapton strip.

The segmentation reduces the impact of a potential short-circuit. In addition, in case of a discharge, the potential of the rest of the foil is not affected.

Foils within one stack are numbered GEM1-GEM4 (Fig. 4.5) The foils GEM1 and GEM4 have a hole pitch of 140 µm, whereas GEM2 and GEM3 have a double-pitch, meaning 280 µm. The large pitch in the two foils improves the ion blocking. Most of the ions are coming from the last amplification step in GEM4. Foils with larger pitch are still mostly transparent for the incoming electrons from the drift volume while it transparency for backflowing ions is limited. In addition, the orientation of the hole pattern is rotated from foil to foil such that the holes are not aligned with each other. This supports the absorption of ions, but also the spreading of the amplified electrons to decrease the charge density.

4.2 Readout chamber

The GEM foils are mounted on top of a chamber body. This consists of a massive aluminum frame in which all electric connections are embedded. On top of the frame, the pad plane is fixed. The pad design is similar to the one from the old readout chambers of the TPC since they provide sufficient resolution [14].

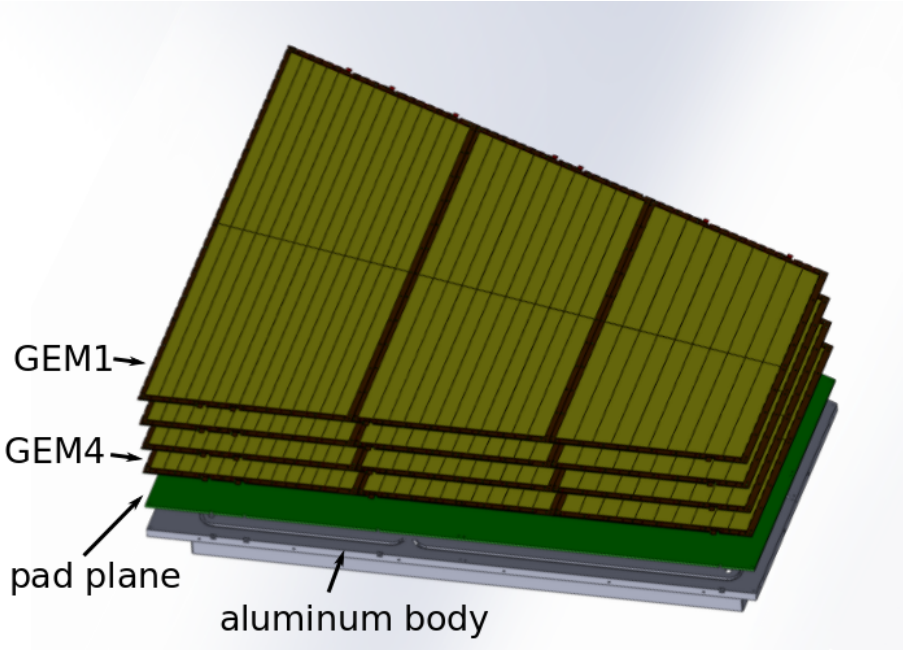

Figure 4.5: Exploded view of an OROC [14].

The GEM foils are stacked on top of the pad plane. A frame (Fig. 4.6) made of Vetronite EGS 103 supports the foils and defines the distance between them. The sagging of the foils is reduced by a 2 mm thick supporting cross that overlaps with the segment borders to minimize the dead area.

Installed in the TPC, the chambers will have the proper readout electronics attached. For testing the chambers in the assembly institute, it is sufficient to read the total currents of the pad plane and the cathode. This can be achieved by interconnecting all pads with each other via shorting cards (Fig. 4.7). Each shorting card covers 40 pads.

4.3 Powering of GEMs

The GEM potentials are chosen such that optimal ion backflow (IBF) and energy resolution settings are achieved. The survey for the best adjustment was performed with $10 \times 10\,\mathrm{cm}^2$ quadruple GEM prototypes in Munich. Various voltages for different foils were tested while the gain was held at 2,000. The ratio V_{GEM3}/V_{GEM3} is set to 0.8 and 0.95 respectively. Three different voltages for GEM2 are checked.

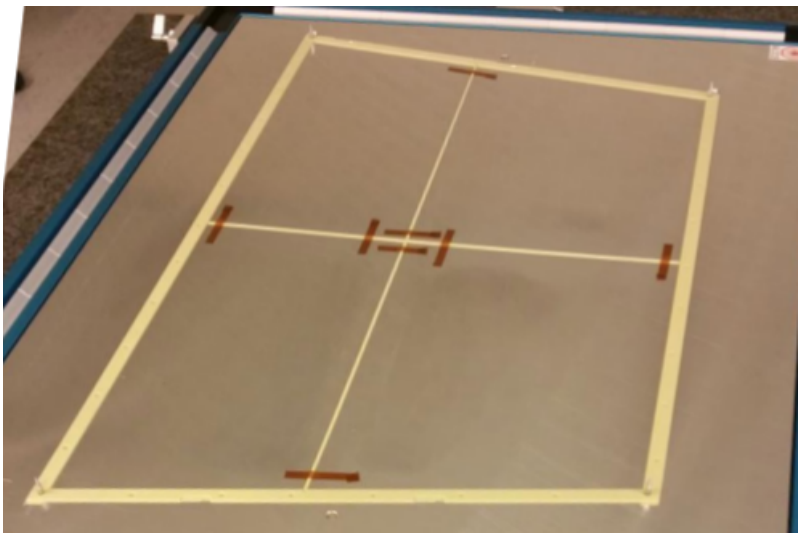

Figure 4.6: GEM frame for OROC1 foil with supporting cross. The frame is placed during assembly in a gluing frame.

In the measurements, the voltage applied to GEM1 is scanned (the gain is held by simultaneously adjusting the voltages of GEM3 and GEM4). In Fig. 4.8 the results of this measurement are displayed. One sees that a better energy resolution implies a worse IBF. The best IBF values are attained with low voltages for GEM1 and 2. A ratio of 0.8 between the GEM3 and GEM4 voltages is preferable as well. The test shows that with the right choice of voltage settings, values for the IBF of $\sim$0.7 % and a energy resolution of $\sim$12 % are reached [14][1].

All in all, this implicates different voltages for the individual foils but also a strong deviation of one transfer field from the standard value. These HV settings, called Settings A, are displayed in Table 4.1. The so called Settings B, where GEM3 and GEM4 voltages are similar will be discussed in Chapter 12.

Electrode	**Voltage**
Drift	400 V cm^{-1}
GEM1	270 V
Transfer 1	800 V
GEM2	230 V
Transfer 2	800 V
GEM3	288 V
Transfer 3	20 V
GEM4	359 V
Induction	800 V

Table 4.1: Voltage settings A of the OROC [23].

[1]The voltages were subject to further fine tuning after publication of [14].

Figure 4.7: Shorting cards, on the backside of the chamber body, connecting all pads of the OROC. The cable in green and yellow connects two rows with each other. The red cables in the back are the HV inputs for the GEMs.

The potential differences between top and bottom side of the GEMs are between 230 V and 290 V except for GEM4, in which the voltage is 359 V. These settings provide the highest amplification in the GEM4 foil in order to create most ions as far as possible from the drift region. The many ions moving back towards GEM3 are not guided into the holes for further amplification due to the low field between GEM3 and GEM4. The effect is intensified by the large pitch of GEM3.

4.4 Gas mixture

Currently, the ALICE TPC is operated with Ne-CO_2-N_2 (90-10-5), after using Ne-CO_2 (90-10) and Ar-CO_2 (90-10) in Run 1 and Run 2. The temporary choice for Ar was motivated by higher stability for the increased rates. Considering the TPC upgrade for Run 3 using GEMs, however, Ar is not the favorable choice anymore. The readout will be operated without a gating grid and a certain IBF will be accepted.

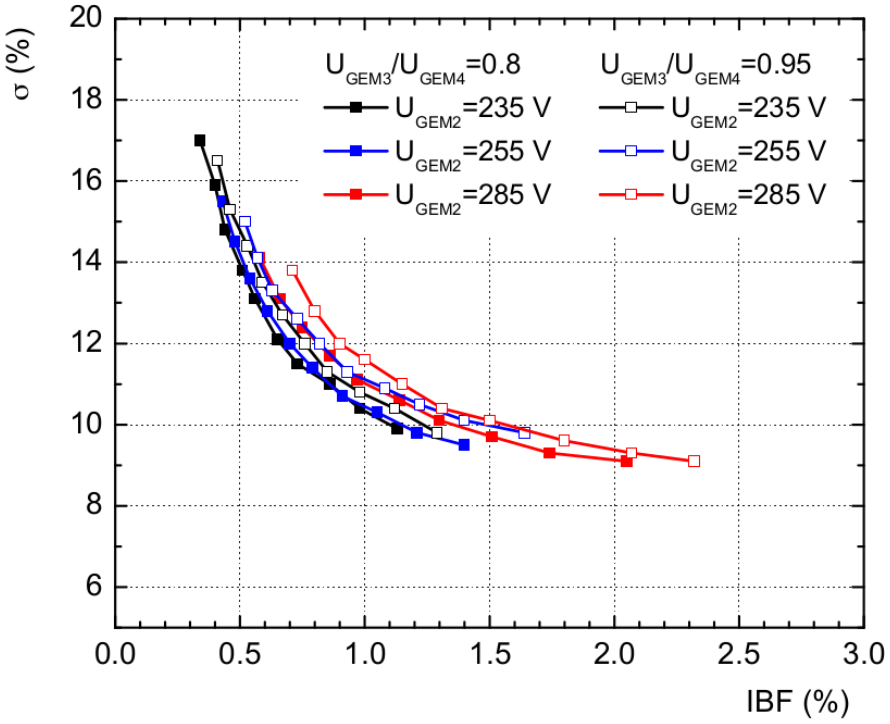

Figure 4.8: Relation between ion backflow and energy resolution for quadruple GEM stack in Ne-CO_2-N_2 (90-10-5). The GEM1 voltage was increased in steps from 225 V to 315 V from left to right. The voltages of GEM3 and GEM4 were adjusted to keep gain at 2,000 [14].

Since the ion mobility is about a factor three lower in Ar compared to Ne, the TPC will stay at the Ne gas mixture to keep down the space-charge [14].

The stability of Ne-CO_2 (90-10) against discharges at high rates is improved by the addition of N_2. Thus, the choice of gas in Run 3 is Ne-CO_2-N_2 (90-10-5).

4.5 Expected radiation

The stability of the detectors at high rates and high currents of electrons and ions in the amplification region are crucial at the LHC. From Run 3 on, the interaction rate of the experiment will be increased from 3.5 kHz to 50 kHz. The estimate of primary-ionisation cluster rate for the most inner and thus most occupied region of the TPC (r = 85 cm) is 100 kHz/cm^2. Assuming all particles to be minimum ionizing particles (MIPs), the total number of electrons per cluster liberated in Ne-CO_2-N_2 (90-10-5) is 36.1. Considering that the gain of the GEM stack is 2,000, the expected charge density is 1 nC/(cm^{2}s). This number is increased by a factor of 10 to an upper safety limit for irradiation tests which are discussed in Chapter 11. This accounts for the presence of highly-ionizing particles, background contributions and secondaries [14].

Part II

OROC commissioning and testing

5 OROC production flow

In order to efficiently use the capacities of the involved institutions, the individual OROC-production steps are performed at different places.

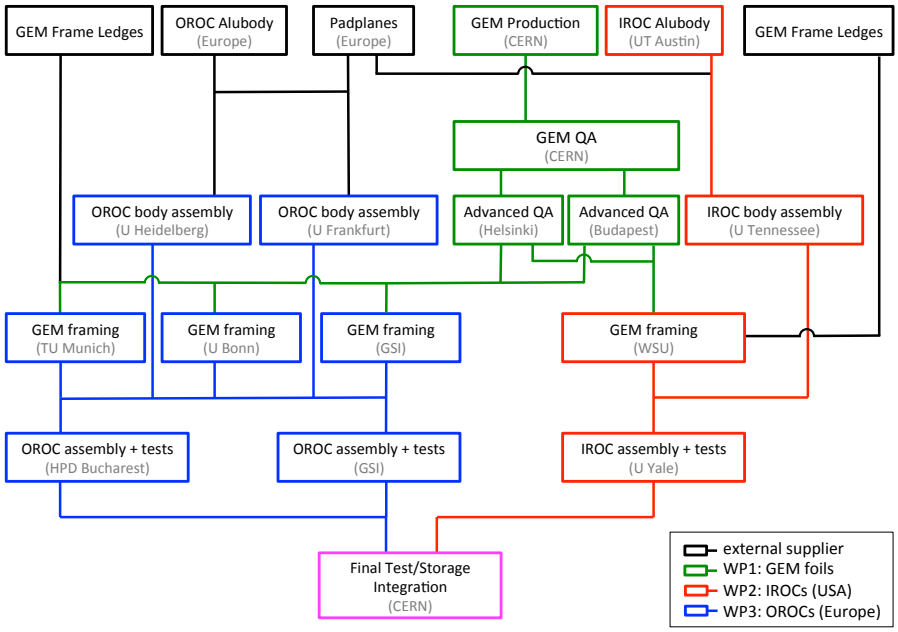

Figure 5.1: Material flow for the readout chambers in the ALICE TPC upgrade project

The GEM foils are produced in the PCB workshop at CERN. The ALICE TPCU group at CERN equips the foils with Optiguard frames and performs the first tests, including creating the defect and spark maps as well as measuring the loading resistors and the leakage current. Subsequently, the foils are sent to the Institute of Physics in Helsinki. Here, the foils are optically scanned and the hole size and defect maps are produced. A long term leakage current test is performed to check stable operation of the foil.

The OROC1, OROC2, and OROC3 foils are now sent to the framing facilities at the TU Munich, HISKP in Bonn, and GSI at Darmstadt, respectively. Upon arrival, a leakage-current test is performed. The foils are stretched and glued to a supporting frame. This is followed by another leakage-current test.

The framed foils are then sent to the assembly centers at GSI and IFIN-HH in Bucharest. Chamber bodies, equipped with pad planes and HV-wire feed-through

are provided to the assembly centers by PI Heidelberg and IKF Frankfurt. After checking again the GEM quality, the foils are trimmed and stacked on top of the pad planes of the OROC bodies. HV wires are soldered to the two GEM sides. The connections are checked by measuring the GEM capacitance.

The fully assembled OROC is attached to the test box and tested for its operational functionality. The testing procedures are:

1. gas tightness of the chamber,
2. gain curve,
3. energy resolution,
4. gain uniformity and ion backflow,
5. stability under full-area x-ray radiation

If a chamber fulfills all requirements of the above tests, it is ready to be operated in the ALICE TPC and thus sent to CERN. Some of these production steps will be closer discussed in the subsequent sections.

6 GEM quality assurance

The production cycle of the OROCs (Chapter 5) results in large traveling distances for the GEM foils. On their way, the foils have to be checked after each transportation step. An easy accessible observable to judge the quality of a foil is the leakage current between top and bottom side.

6.1 Test procedure

After arrival the foils are put into special dry cabinets. After at least one day of regeneration time, the foils are cleaned with a nitrogen gun and then put into a special drawer (Fig. 6.1) where the foils are sandwiched between two Plexiglas plates. The bottom plate defines the GEM position, the top one has pins which provide HV connection. Every segment of the foil is connected individually to the power supply via one pin, the HV path is connected as well via aits own pin. The bottom side of the GEM is connected to ground using a copper plate which is again in contact with a separate pin. The drawer is then put in the test box, a lockable system to guarantee stable test conditions. The pins are connected to the power supply via links at the test box.

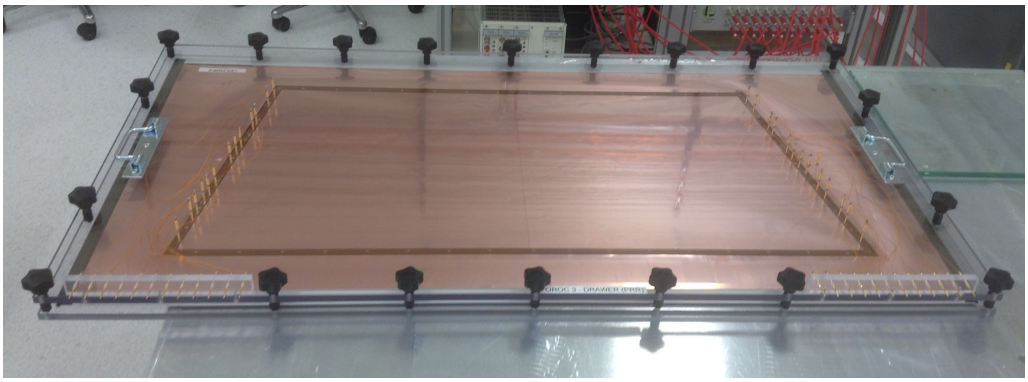

Figure 6.1: Drawer for the leakage current test of OROC3 foils. The vertical pins provide the connection of the individual segments to the HV supply.

The test box is flushed with nitrogen. The test start when the humidity drops below 10 %. In order to burn potential dust particles, the high voltage (500 V) is applied without ramping. The leakage current of the individual segments is recorded, while the foil is kept for 1000 s at this voltage.

The segments are connected to the HV path via loading resistors. The resistors are soldered already at the foilproduction site at CERN. Their presence affects leakage

current measurements because the current can flow to ground through two ways: via picoammeter (internal resistance of 10 MΩ) or via the loading resistor (5 MΩ). The actual leakage current, thus, is three times higher than the picoammeter reading.

A foil passes this test if the mean leakage current of all segments is below 167 nA. Any strange behavior, like excessive sparking during the measurement or increased current in one or more segments, triggers a detailed investigation. In many cases, additional treatment with the air gun or a sticky roller cures the affected segments. If the problem can not be solved, the foil sent back to CERN.

All steps, especially handling of the foils, have to be done with special care since pollution with dust or other particles could affect the properties of the foil. Special precautions should be taken to prevent metal dust. Metallic particles could fall inside the holes of a GEM and, unlike dust, will not be burned under voltage. This is why the drawer is cleaned with isopropanol after each measurement. Special attention is paid to the screws holding the drawer together. Those are put into an ultrasonic bath every four tests.

6.2 Results

QA tests of the GEM foils were an important part of my master thesis work. The majority of the foils passed the test without any noticeable problems. Some foils had an increased current of a few hundred pA in one of the segments. The leakage currents of one foil with a short are shown in Fig. 6.2. In most cases, the functionality of these foils could be restored by cleaning. The foils were once more cleaned with the nitrogen gun and treated with the sticky roller. The origin was obviously dust in the foil holes working as bypass. For one foil with a permanent short, all additional cleaning steps yielded no improvement, resulting in the QA status “failed”.

A second foil which had an abnormal behavior in one segment – the current was more than two times higher than in other segments – which did not lead directly to the exclusion of the foil because the leakage current of this segment was still below the limit. This foil was, nevertheless, excluded from further usage since no clear explanation was found for the effect. The precaution that the increased current of a single segment could be connected to a weak point causing problems in the future overruled the official limit. The leakage currents of this foil are shown in Fig. 6.3. For comparison, a typcial foils is shown in Fig. 6.4.

All in all, 43 OROC3 foils were tested in the preproduction phase and the regular production during this thesis. 27 of those were framed at GSI and thus tested twice. In addition, 28 framed OROC1 and OROC2 foils were tested after arriving from Munich and Bonn, respectively. Only two OROC3 foils had to be excluded from further use because of result in the leakage current test. Most “failed” foils drop out of the production cycle earlier. The leakage current is already measured at CERN after production, already existing damages or problems are therefore detected much earlier. The probability that a foil gets damaged during transport or framing is rather low.

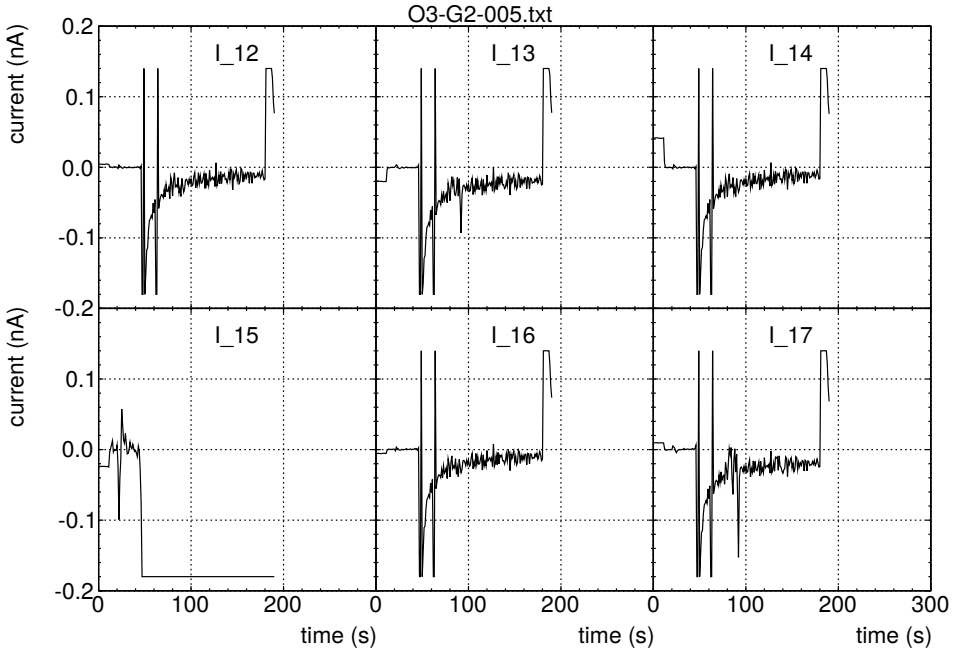

Figure 6.2: Bad foil: leakage current measurement of six segments of GEM foil O3-G2-005. Current of segment 15 is above threshold because of a short. The foil functionality could be restored by cleaning.

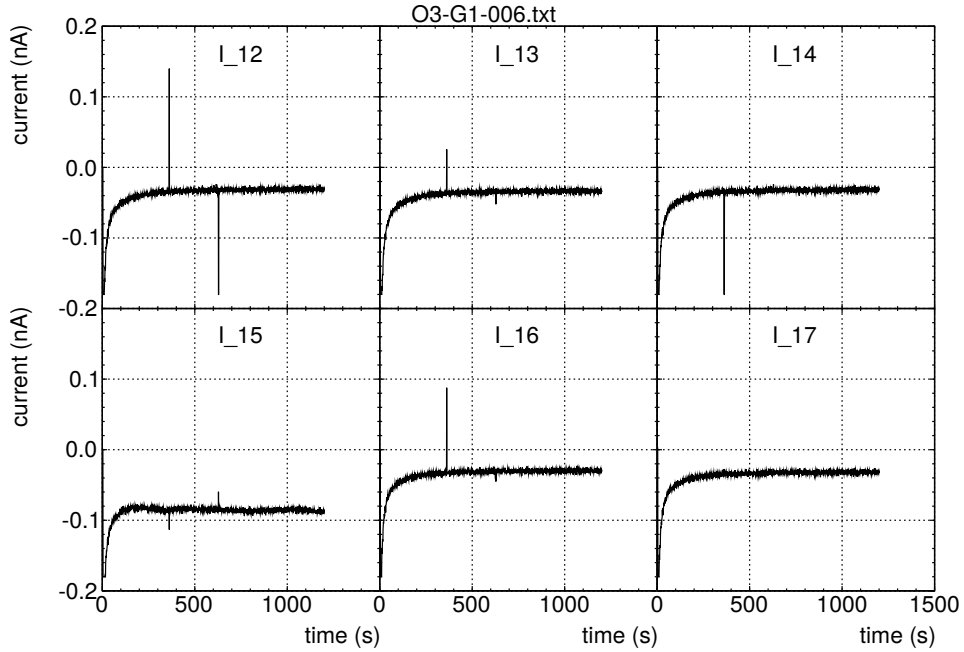

Figure 6.3: Bad foil: leakage current measurement of six segments of GEM foil O3-G1-006. Leakage currents of all segments are below limit of 0.167 nA, but current of segment 15 is increased compared to other segments. For this reason the foil was excluded

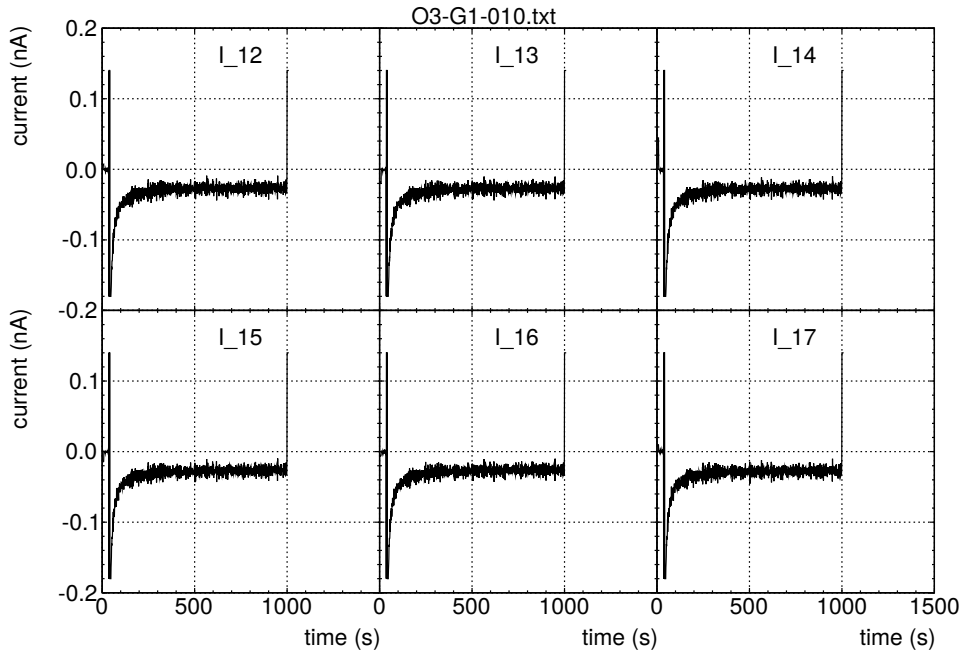

Figure 6.4: Good foil: leakage current measurement of six segments of GEM foil O3-G1-010. Leakage currents of all segments are well below the limit of 0.167 nA.

7 Gas tightness test

At the experiment, the readout chambers will constitute the end plates of the TPC cylinder, enclosing the gas volume. The requirement of gas tightness translates to a maximum leak rate of 0.5 mL/h per OROC. The gas tightness test is performed for every assembled chamber

The OROCs are put into a test box, the test box itself is sufficiently tight. For the test, the box is flushed with Ne-CO_2-N_2 (90-10-5). The oxygen and water level of the gas outlet is monitored and once the oxygen level reaches an asymptotic value the measurement can start. The relevant observable for this measurement is not the absolute oxygen level, it is the leak rate and thereby rather the ratio of the oxygen level and the gas flow. This results in different maximally acceptable oxygen levels depending on the gas flow (Table 7.1) .

Gas inflow	**Oxygen limit**
20 L/h	5 ppm
10 L/h	10 ppm
5 L/h	20 ppm
2 L/h	50 ppm

Table 7.1: Relation between gas inflow and oxygen limit

The chamber is flushed first with a high gas flow of 20 L/h. The oxygen and moisture content are monitored with a Rapidox or Orbisphere device (for technical details see [24] and [25]). Once a low oxygen content is reached, the flow can be reduced to save Ne. When the content reaches an asymptotic level (this takes several hours or even days) the oxygen content is compared to the limit in Table 7.1.

The measurements of the oxygen content inside the chambers were challenging since different devices provided different results. In the beginning, the oxygen measurement was performed by a Rapidox. The outflowing gas was connected to the device and a few meter long pigtail tube in parallel. The Rapidox displayed for a chamber with surrounding test box a value between 5–11 ppm at a gas flow of 4.5 L/h which is clearly within the limit of Table 7.1. During the scans of OROC/1, this Rapidox measurements were cross-checked by an Orbisphere device connected in front of the pigtail. The Orbisphere displayed a value above 100 ppm. Since the Rapidox had been recently calibrated with a nitrogenous calibration gas containing 100 ppm oxygen, the values of the Orbisphere seemed to be false. In addition, the Orbisphere sensor had not been regenerated for more than a year.

A systematic check of all Rapidox and Orbisphere devices accessible in the detector lab at GSI was performed by a colleague (Michael Träger) had a similar problem in his setup using an Ar gas mixture. All three Rapidoxes were once more calibrated with the nitrogenous calibration gas containing 100 ppm oxygen. Two recently regenerated and our Orbisphere were added to this study. All six devices were connected for several days to the same gas system providing a Ar-CO_2 mixture. Though, the Rapidoxes were all connected in series to the same input and calibrated with the same gas, the claimed oxygen contents differed. Two devices, including the one used in our tests, showed 5 ppm and 10 ppm which corresponds roughly to the expected contamination for the input gas (5 ppm). The third one, however, measured an oxygen content of around 40 ppm. The two regenerated Orbispheres showed as well appropriate values around 5 ppm. This applied as well to our Orbisphere which showed the same values.

The colleague suspected that the calibration of the Rapidox devices with a nitrogenous reference gas is not adequate when gas mixtures containing predominantly Ne or Ar are measured later. His suggestion was to get reference gases more similar to the gas mixtures used in the experiment. Concerning the high value measured by the Orbisphere in Ne-CO_2-N_2 (90-10-5), one possible explanation is that it was forgotten to enable the CO_2 measurement mode which is needed for gases containing CO_2. The Rapidox, on the other hand, should be calibrated with a Ne reference gas or be replaced by a well functioning Orbisphere.

8 OROC commissioning

8.1 Powering via voltage dividers

The electrical potentials of a stack are provided by voltage dividers. The powering of the OROCs was already outlined in section 4.3.

A test was performed to check if the voltages, provided by the voltage divider boxes, agree within $\pm 1\,\mathrm{V}$ with the nominal values (see Table 4.1). During the test it was noticed that for some resistors the respective power limits ($0.25\,\mathrm{W}$) were exceeded. This concerned mostly the transfer gaps. The resistors of the voltage divider were entirely exchanged keeping an eye on the acceptable power dissipation.

The new resistors were chosen such that for the transfer fields ($\Delta\mathrm{U} = 800\,\mathrm{V}$), two $330\,\mathrm{k}\Omega$ and two $470\,\mathrm{k}\Omega$ resistors are connected in series. This results in a maximal power dissipation of $< 0.2\,\mathrm{W}$ per resistor, considering $0.75\,\mathrm{mA}$ as the upper current limit of the system. With this powering setup the resistors should operate stably. However, one has to be careful with increasing the voltage to much higher values than the nominal one, e.g. for the gain curve measurements, to not exceed the power dissipation limit. The maximum allowed increase is $20\,\%$.

8.2 Charging up effect

The first time OROC/0 was operated, it was irradiated at different spots with a radioactive source while the pad current of the chamber was monitored. Keeping the source on one specific spot for several seconds resulted in a continuously increasing current. This test was also performed with OROC/1 (Fig. 8.1). After around two minutes, the pad current reaches an asymptotic value. Continuing the irradiation at the same spot after a short waiting time showed that the pad current started at the saturation level and was not rising much further. This observation was made for many spots.

This effect is expected for GEM foils and was already investigated by Alfonsi et al. [26]. The exposed Kapton inside the GEM holes is, as a dielectric, charging up at the surface. The electrical field lines get squeezed together by the space charges on the walls which result in a higher field and thus a higher gain. The relaxation of the charging process takes much longer. Hence, a chamber can be charged up by irradiation and remain in this state during a measurement. This implies for the test procedure of the OROCs, especially the uniformity scans, that the chambers should be pre-irradiated to keep the current during the measurement on the stable plateau.

Colleagues at other institutes observed that the duration of the charging is strongly correlated to the moisture in the gas – the higher the level, the sooner the asymp-

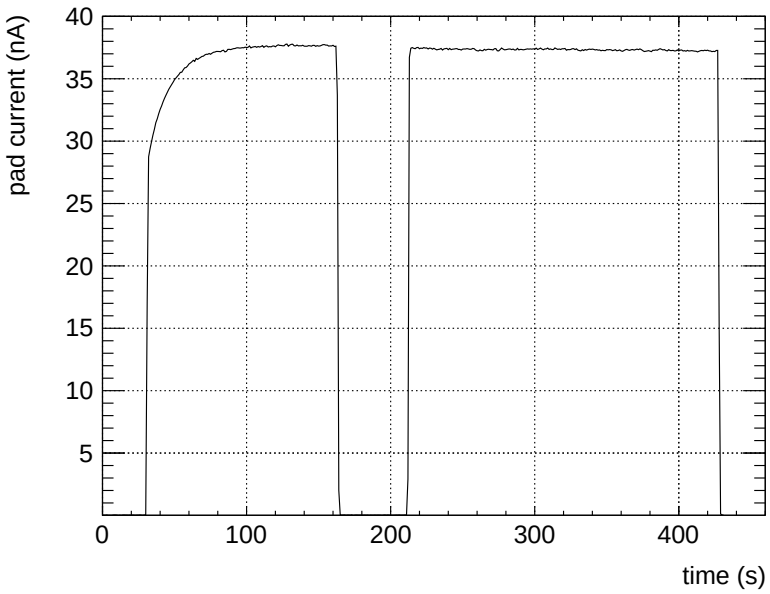

Figure 8.1: Evolution of pad current of the OROC/1 under irradiation of one spot of the OROC1 stack by an x-ray tube. The tube was turned off and on in the interim.

totic value is reached. During all tests presented in this thesis, the moisture level was rather high with around 1000 ppm.

8.3 Bad segment survey

In the OROC/0, the gain uniformity scan revealed that in the OROC3 stack two segments were not working properly (Fig. 10.2). These were segments 3 and 21 (cf. Fig. 4.3). To localize the reason of the defects without opening and disassembling the chamber, the GEMs were first examined for shorts by applying a voltage on the foils and a direct resistance measurement between top and bottom side of the foils. No indication of a short was found. Then, the individual GEM currents were recorded while the x-ray tube was moved across the stack. In fact, the GEM currents showed an anomalous behaviour in the two suspicious segments. The assumption is that for the examined area at least one foil in the stack is floating. If this is the case, it follows from the working principle of a GEM stack that a reduction of in the current is expected in the foil of the floating segment and in all foils following it. The prior foils, facing to the drift volume, should not show any unusual signals. The current measurement in Fig. 8.2 of the GEM1 Top showed clearly that the GEM1 currents drops at the position of segment 23. The same effect is observed for the other GEM foils at the position of segment 23. Regarding segment 3, only in measurements of the GEM4 currents a noticeable deviation from the working segments was observed (Fig. 8.3).

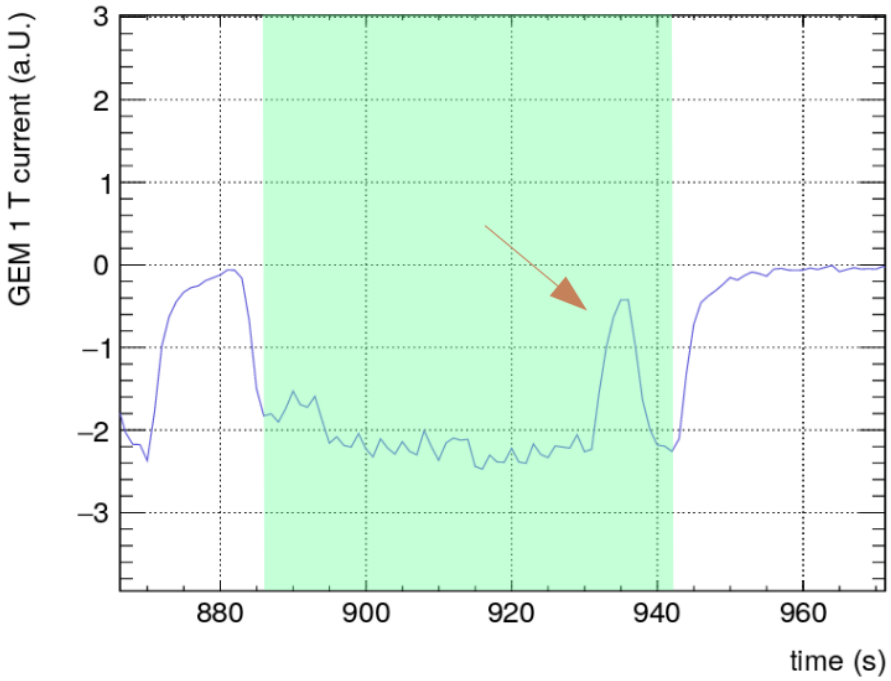

Figure 8.2: GEM1 Top current of the OROC/0 measured by moving source from outer to inner region. The green marked zone corresponds to the area of the OROC3 stack. The current drops at position of segment 21 (red arrow). No striking feature at position of segment 3 is seen.

After the completion of the full test procedure of the OROC/0, the test box was opened and the connectivity of each segment to the high voltage path (cf. Fig. 4.4) was checked for each foil successively. Surprisingly, every segment had a working connection to the HV path. Besides, it was cross-checked that there was no short in every segment.

After that, the resistors were optically examined. In GEM1, the soldering of the resistor actually looked imperfect for segment 21. With little mechanical force, the resistor got detached. The same happened for the resistor of segment 3 in the GEM4 foil (Fig. 8.4). The resistors of other segments, on the other hand, were firmly soldered.

Does the chamber work now?

The procedure shows that the source of a defect can be examined already on the test stand. In the case of the development of a short, the stack will draw more current than the others. Additionally, the resistance between top and bottom side can be checked. For floating segments, the test sequence described above is suitable where the GEM currents show which foil is malfunctioning.

This examination of the OROC/0 was done while no device was yet available in the clean room to measure the capacitance between segmented and unsegmented side sufficiently accurate. The deviation of the capacitance of one foil would tell whether one or more segments are floating. In the upcoming mass production of

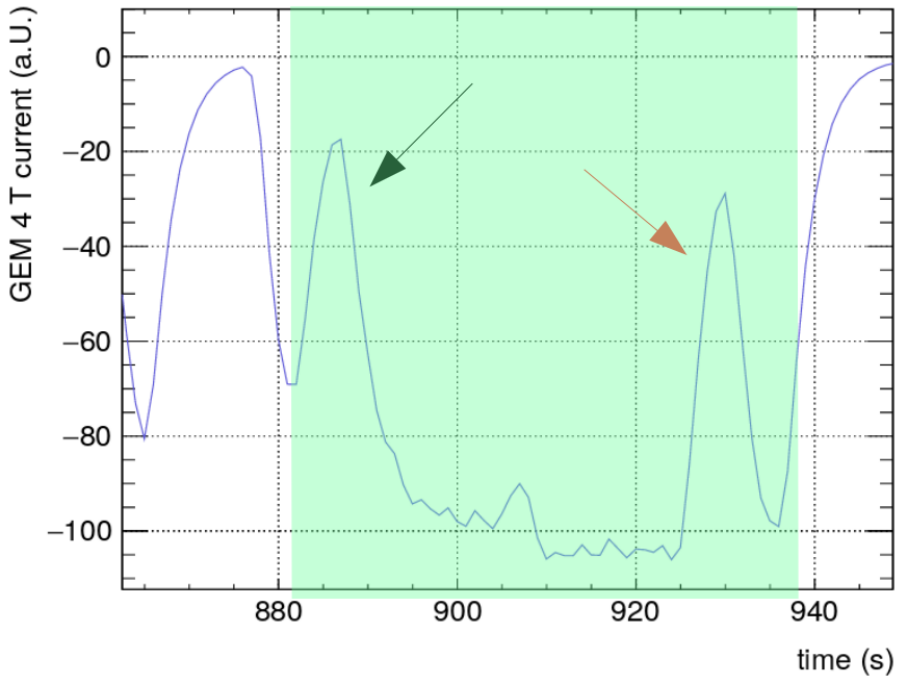

Figure 8.3: GEM4 Top current of the OROC/0 chamber measured by moving source from outer to inner region. The green marked zone corresponds to the area of the OROC3 stack. The current drops at positions of segment 3 (black arrow) and 21 (red arrow).

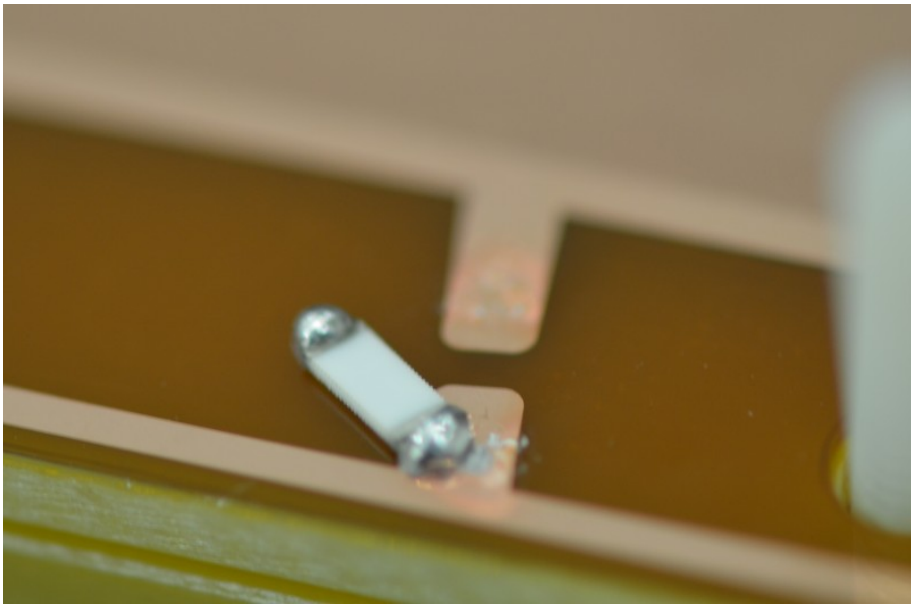

Figure 8.4: Resistor of segment 3 of GEM4 in the OROC/0 that was not properly soldered. It got detached after applying small mechanical force.

OROCs, a fast diagnosis of errors will be important and thus such a device was purchased.

One should pay attention to the fact that the missing connectivity of resistors can evolve after turning the chamber into the vertical position. Thus, it is advised to check the capacitance also after moving the chamber to the test stand. Besides, the finding of the floating segments at GSI resulted in the addition of the test of the mechanical strength of the solders. In the early QA stage, a small mechanical force is applied to the resistors by plastic tweezers.

9 Gain curve and energy resolution

9.1 Gain curves

The gain curve is measured for all chambers to provide the following informations. First of all, the actual absolute gain is obtained. In addition, the stability at high gains of the chamber can be checked. A deviation from the expected exponential shape of the curve would indicate some misbehavior. In the end, the nominal voltage can be adjusted to match to the nominal gain of 2,000. The following sections will discuss the measurement and present the gain curves of the chambers OROC/0 and OROC/1.

9.2 Measuring method

The absolute gain is estimated by irradiating the chamber in a distinct spot with a ^{55}Fe source. The pads in the irradiated area are connected to one individual shorting card which is shielded to minimize background effects. The card is connected to a spectroscopy amplifier chain, all other pads of the chamber are connected to ground. The OROC is set on the selected voltage. The background of the signal is suppressed by a discriminator by adjusting the threshold. This is done by looking at the histogram filled with the ADC counts of the signals.

The final measurement is done by recording the signal rate and the pad current. Every x-ray liberates on average 166 primary electrons in the chamber gas. Thus, the absolute gain of a stack is obtained by recording the corresponding pad current and assuming 166 primary electrons per x-ray.

$$\text{gain} = \frac{I_{\text{pad}}}{\text{rate} \cdot 166\, e} \tag{9.1}$$

The voltage is scanned such that a gain curve with values between 1,000 and 7,000 is obtained.

9.3 Gain curve of OROC/0

The gain curve for the OROC/0 was determined by applying voltages between 3907 V and 4507 V in steps of 100 V to all stacks. For every stack, a spot is chosen where no significant current fluctuations are visible by moving the source to the surrounding.

The obtained gain curve (Fig. 9.1) shows deviations of the absolute gain for the individual stacks. It suggests that the voltages should be adjusted for the stacks OROC1 and OROC2 to provide the nominal gain of 2,000. Since every stack is powered individually via an own voltage divider, the nominal voltages of the two stacks can simply be increased by +50 V and +100 V, respectively.

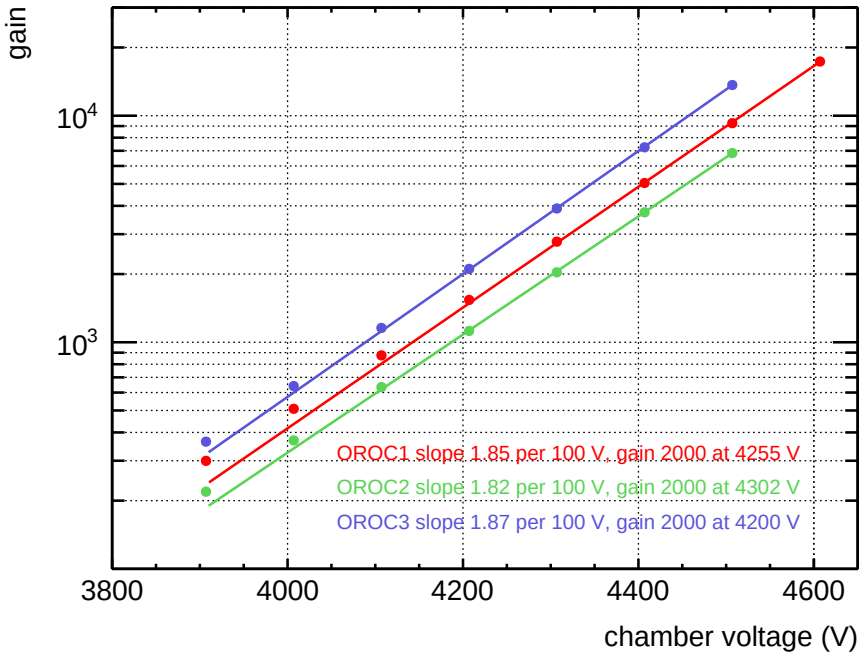

Figure 9.1: Gain curve of the OROC/0. The pad current and the signal rate is translated to the absolute gain for different voltages. To attain the nominal gain, the voltages of the stacks OROC1 and OROC2 have to be adjusted by +50 V and +50 V, respectively.

These value should be treated with care since the spots do not necessarily match to the mean gain of the stack. In the uniformity scans, described in the next chapter, the gain alignment of the stacks due to the suggested adjustments can be checked by comparing the mean values of the pad current.

In any case, the chamber shows a stable behavior at high gains around 7,000 and no significant deviations from the expected exponential rise of the gain. The exponential curve flattens slightly coming to smaller gains. This is related to the fact that the left flank of the spectrum reaches the range of the pedestal for voltages below 4100 V and small energy deposits can not be distinguished from the background anymore. The gain in the presented gain curve was calculated considering the rate measured at the highest gain.

9.4 Gain curve of OROC/1

The gain curve of the OROC/1 (Fig. 9.2) was measured the same way as the OROC/0. The gain curve shows that all stacks have nearly the same gain. The deviation from the nominal gain that corresponds to 2,000 at 4207 V are smaller than those of the OROC/1. The suggested adjustments are −40 V for OROC1 and OROC3 and −20 V for OROC2.

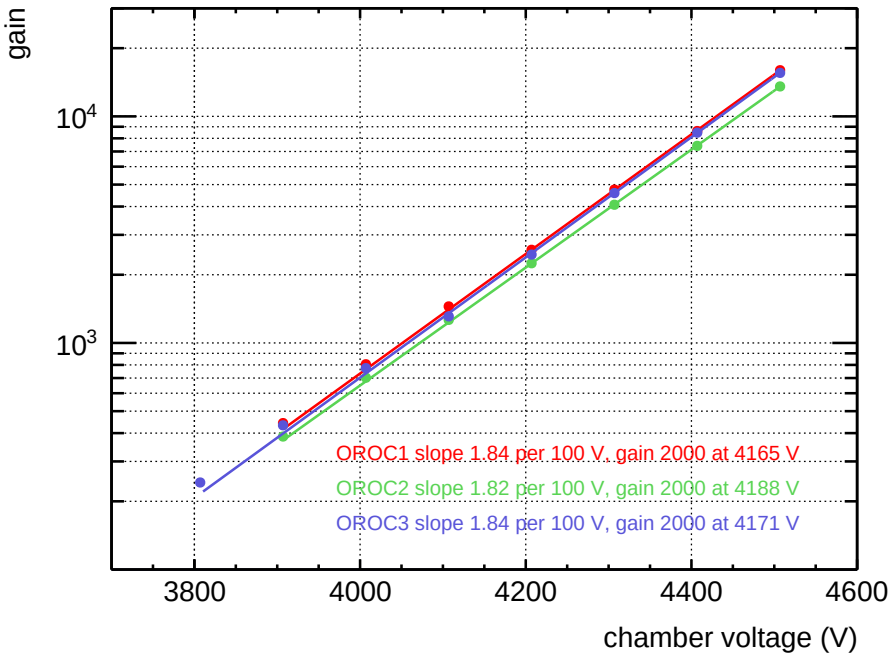

Figure 9.2: Gain curve of the OROC/1. The pad current and the signal rate is translated to the absolute gain for different voltages. To attain the nominal gain, the voltages of the stacks OROC1-3 have to be adjusted by −40 V, −20 V and −40 V, respectively.

The OROC/1 shows stable behavior up to high gains of 7,000 as the OROC/0. During this measurement, it was observed that also for higher voltages of 4100 V or higher the rate is not constant but slightly decreasing from higher to lower voltages. The next section will discuss this voltage dependence and its relevance.

9.5 Voltage dependence of rate

In the gain curve measurement of the OROC/1, the rate was measured in addition to the pad current. A trend of decreasing rate with decreasing voltage was observed. In general, a small decline is expected since for smaller voltages more and more signals fall below the threshold. Looking at the spectra in the next sections (Fig. 9.5 & 9.7), one sees that this accounts for signals in the tail left to the peak. To check how

much the decreasing rate is related to this effect, the missing area cut away by the threshold is estimated. For this purpose, a pedestal measurement was performed for each stack to determine the mean ADC count of the background. This value serves as the lower border of the missing area, the upper border is the threshold itself. The relative change of the overall integral of the spectrum after adding the missing area is equivalent to the correction factor that should be applied to the measured rate. For higher gains, an opposing effect can be observed, namely that parts of background are interpreted as signal because the pedestal peak extends above the threshold. This contribution was subtracted from the overall integral of the spectrum. The corrected rate, obtained this way, is decreasing less to lower voltages than the measured one (Fig. 9.3).

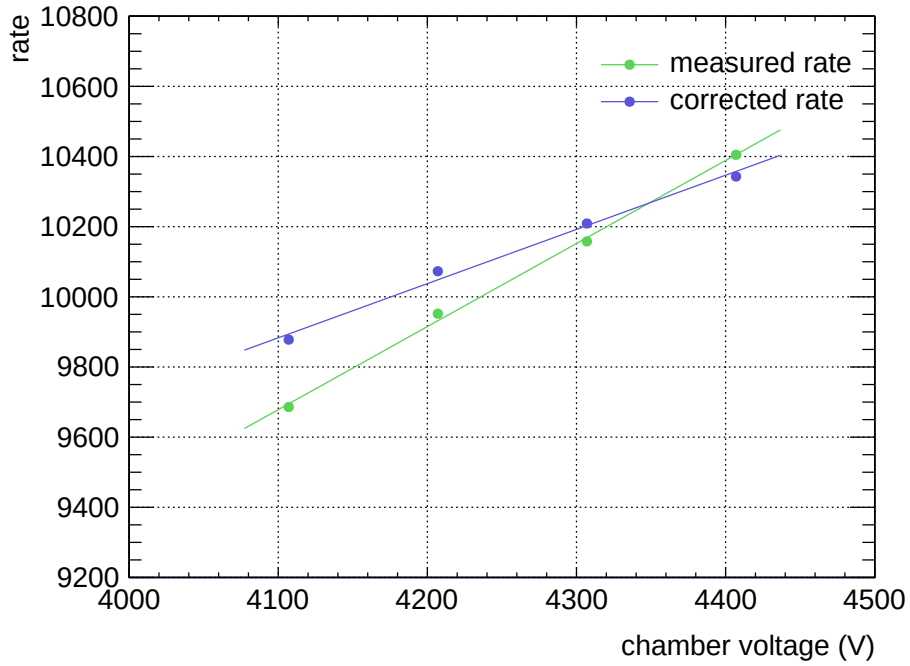

Figure 9.3: Voltage dependence of rate measured for OROC3 stack of the OROC/1. The measured rate is displayed in green, the corrected in blue. The corrections were performed by considering signals below the threshold but above the background. Nominal voltage = 4207 V

The true rate of x-rays coming from the source, however, is independent of the different voltage settings. The rate determined by the highest voltage settings with a threshold just above the pedestal peak should give the most accurate estimate.

Another assumption that is put to test is that on average 166 primary electron are released by absorbing an x-ray. This is valid for the energies deposited by x-rays inside the iron peak but not necessarily for signals in the tail. The measured current and rate however take all signals into account what leads then to an underestimate

of the gain. The gain is proportional to $I_{pad}/rate$ (Equation 9.1). The pad current corresponds to the sum of the ADC counts times the number of entries for all bins in the spectrum while the rate corresponds to the sum of number of entries.

$$I_{pad} \equiv X = \sum_i x_i n_i; \qquad rate \equiv N = \sum_i n_i \tag{9.2}$$

Using the above equations, one can simulate what would be the estimated gain if only the x-rays of the peak would give a signal. The area is divided into A and B corresponding to tail and peak, illustrated by Fig. 9.4.

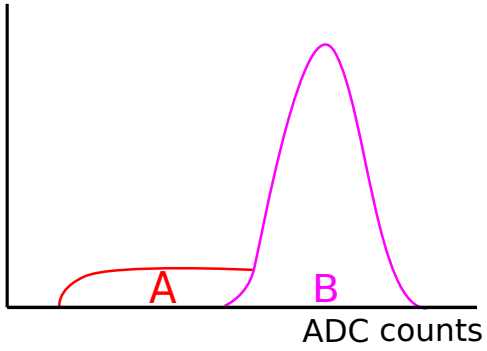

Figure 9.4: Shape of ^{55}Fe spectrum divided into tail and peak parts.

The virtual gain arising only from x-rays of area B is calculated by multiplying the real gain by a correction factor (Equation 9.3) derived from the shift of the mean value since the tail is gone.

$$\frac{X_A/X_{A+B}}{N_B/N_{A+B}} = \frac{\langle x \rangle_B}{\langle x \rangle_{A+B}} \tag{9.3}$$

Considering the OROC3 stack of OROC/1, this factor is 1.08 and 1.06 for 4407 V and 4307 V, respectively.

All in all, the small rate deviation at different voltages of the order of a few percent and the possible underestimate of the gain due to the tail of the spectrum are negligible within the scope of the tests at GSI. The gain curve in Fig. 9.2 shows that the gain is increased by the factor 1.84 per 100 V. A variations of ±10 % would correspond to adjustments of the voltage of only ∼10 V. For the functionality tests at GSI, this precision is not needed.

9.6 Energy resolution

The energy resolution is an important property of the chambers since the TPC is the central PID detector of the ALICE experiment and determines the particle identity by the energy loss. The deposited energy of traversing particle has to measured

accurate enough. The energy resolution and the ion backflow are two competing properties of the detector as outlined in section 4.3. Fortunately, quadruple GEM detectors can be operated with an energy resolution comparable to the current TPC with a sufficiently low IBF. The energy resolution is determined by the peak width of an ^{55}Fe source. The accepted limit is set for all chambers to $\sigma_E/E \leq 12\,\%$.

9.7 Measuring method

This measurement works mostly like the recording of a gain curve described in the previous section. The nominal voltage is applied to the stack and the signal of 40 pads is connected to an ADC. With this setup the spectrum is recorded in every stack with the voltage corresponding to a gain of 2,000. To correct for the background contribution to the peak position, a pedestal measurement without source is done. The width of the peak is corrected for the width of the pedestal. Thus, the energy resolution is obtained by:

$$\text{energy resolution} = \frac{\sqrt{\sigma^2_{\text{meas}} + \sigma^2_{\text{pad}}}}{\text{peak position} - \text{pedestal}} \tag{9.4}$$

9.8 Energy resolution of OROC/0

The spectra of the OROC/0 (Fig. 9.5) were recorded for every GEM stack before the gain curve measurements. For all stacks, the resolution is worse than the limit of 12 %. Particularly, OROC2 exceeds the limit by almost a factor two with around 25 %. Looking back to the gain curve (section 9.3), one sees that the stacks OROC2 and OROC1 were not operating with nominal gain at nominal voltage. OROC3 – close to nominal gain – is much closer to the limit with 14.4 %.

The resolution is related to the gain and by this to the voltage. Thus, a more meaningful resolution estimate for OROC2 would use the voltage correction suggested before of +100 V. The spectrum using this higher voltage is displayed in Fig. 9.6. In fact, the energy resolution improved to 16.1 %. This value is more comparable to the OROC3 stack, though passing the over the limit as well.

The measurements show that the energy resolution of the OROC/0 is not fulfilling the requirements to preserve the properties of the TPC. No conspicuity like increased moisture or problems in the GEM production were observed. Then again, it is important to mention that the energy resolution depends on the applied voltage. A voltage change of only 100 V decreased the energy resolution from 25 % to 16 %. This means that it is essential to operate in the range of the nominal gain for this measurement. This is best achieved by measuring the gain curve and the energy resolution in exactly the same spot. Then, the suggested voltage adjustments from the gain estimate is appropriate and should be sufficient for the resolution measurement.

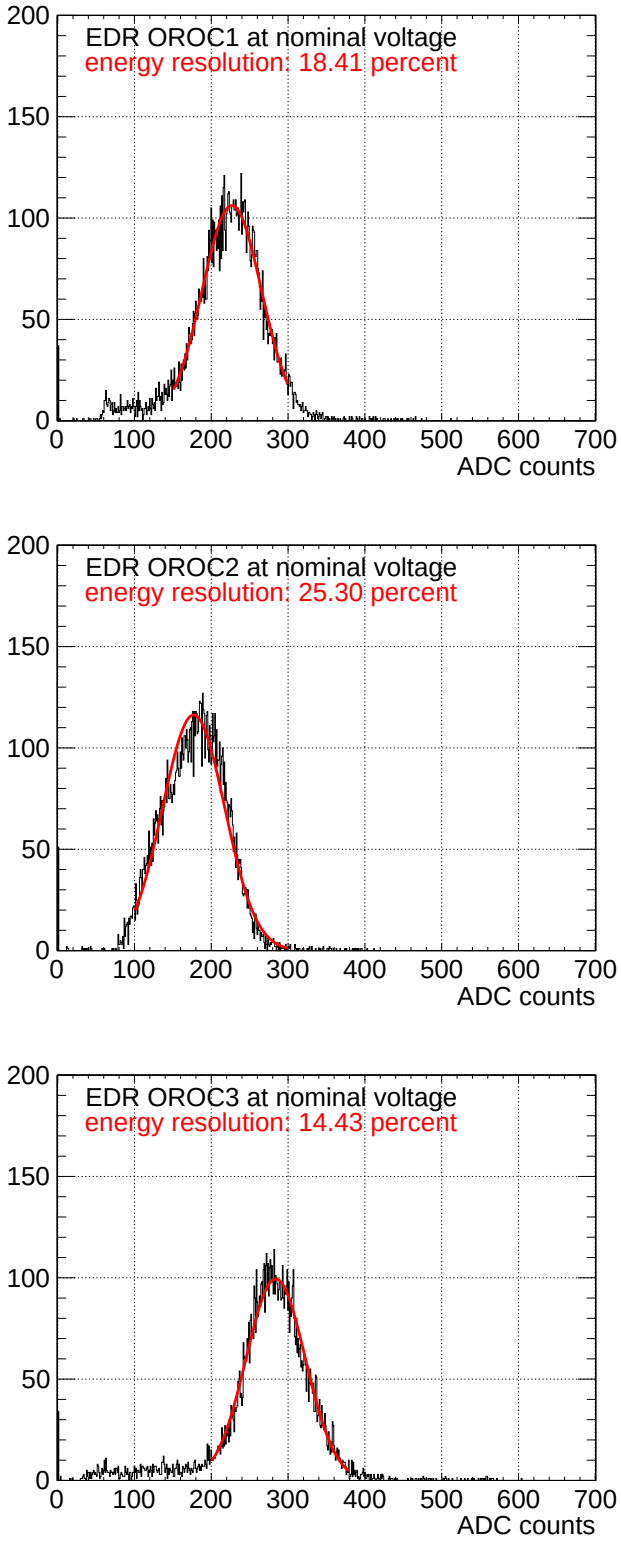

Figure 9.5: Spectra of ^{55}Fe source recorded with the three OROC stacks of OROC/0. Energy resolution calculated by dividing the width of the gauss fit by the pedestal corrected peak position.

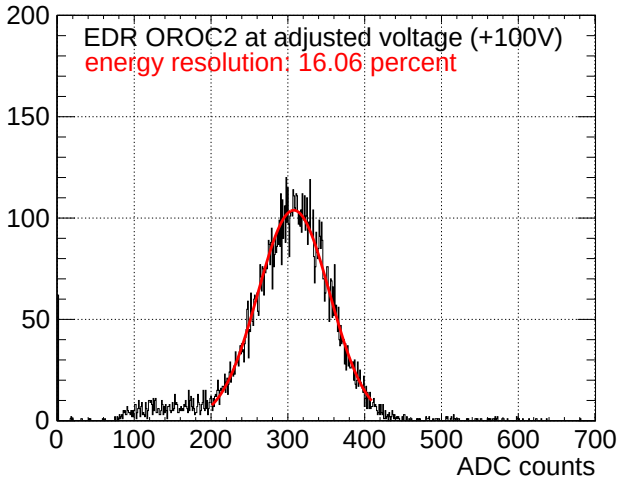

Figure 9.6: Spectrum of ^{55}Fe source recorded with OROC2 stacks of OROC/0 with adjusted voltage (+100 V). Energy resolution calculated by dividing the width of the gauss fit by the pedestal corrected peak position.

9.9 Energy resolution of OROC/1

The energy resolution measurements of the OROC/1 were performed the same way as the for the OROC/0, its spectra are shown in Fig. 9.7. The resolution of this chamber is better compared to the OROC/0 discussed before. The OROC2 stack fulfills the requirement with an energy resolution of 11.6 %, the OROC1 stack exceeds the limit only slightly by 0.5 %. The OROC3 stack has a worse energy resolution of 14 %. One attempt of explain the bad value of OROC3 employs the uniformity test measurement from the next chapter. In Fig. 10.5, the uniformity scan of this chamber is shown. The OROC3 stack has a distinct area with increased gain. This area smears the pad current distribution in Fig. 10.6 which is used to check the voltage adjustments suggested in the gain curve measurement. The area could have shift the mean value such that as a consequence of this the area with "normal" gain is operated with too low gain resulting in worse energy resolution.

In summary, the OROC/1 which underwent the complete QA procedure provides a satisfying energy resolution. Two of three stacks were operating below or close to the limit of 12 %. The violation of the limit of only 2 % by the third stack is probably related to gain nonuniformities caused by one foil. The optical scan data from Helsinki, revealing that the hole diameter deviates in one particular foil, was not yet accessible while mounting the chamber since the data base of the project was still under development in this time.

In case of the energy resolution of the next chamber would still have a slightly worse energy resolution than 12 %, the HV settings of the GEM stack could be adjusted. As outlined, the ion backflow and energy resolution are competing properties. In Chapter 10, the ion backflow is estimated, revealing that the value is well below its limit which leaves the door open for adjustment in favor of the resolution.

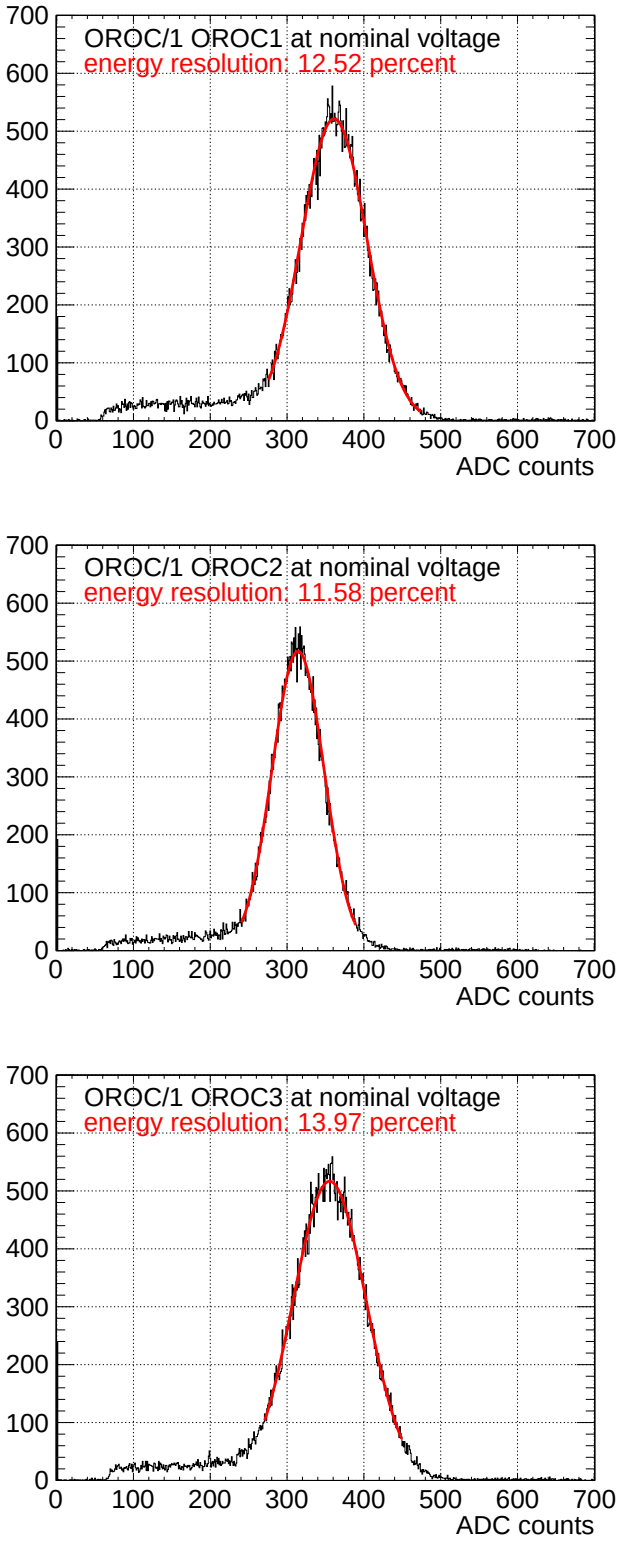

Figure 9.7: Spectra of ^{55}Fe source recorded with the three OROC stacks of OROC/1 chamber. Energy resolution calculated by dividing the width of the gauss fit by the pedestal corrected peak position.

10 Gain and ion backflow uniformity test

A charged particle traversing the TPC ionizes gas atoms. The ionization electrons drift to the readout chambers where the signal is amplified by a factor of ~ 2000. Spatial nonuniformities of this gain factor have to be calibrated and corrected for. At hardware level, they are required to be below 20 % (RMS). This is checked by measuring the response of every produced chamber to a collimated x-ray generator illuminating different areas.

The potentials of the 4 GEM foils are chosen such as to prevent ions (mostly produced in GEM4) from entering the drift volume. The residual ion back flow is required to be below 1 %. The backflow – and its postion dependence – can assessed by measuring the cathode current during the gain uniformity test.

10.1 Test setup

The gain and IBF uniformity are measured at the scanning test stand shown in Fig. 10.1 inherited from the TRD[1] [27] production for ALICE at GSI. It is an apparatus consisting of a rack holding the chamber in vertical position and a movable arm where an x-ray tube (Appendix A.2) or a radioactive source (Appendix A.1) can be mounted. The arm is controlled by a PC.

The arm can be moved to every point of the OROC. An automated scanning program drives the source from point to point and stores the coordinates and the values of the pad and cathode currents.

10.2 Measuring method

In the uniformity scans all pads are connected with each other by shorting cards. The pads and the cathode of the test box are connected to a picoammeter. The chamber is hanging on the test stand described above. The x-ray tube is then moved from point to point with a predefined step size. The tube can be equipped with collimators of different sizes defining the irradiated area. For each measurement point its location, pad and cathode current are stored. The pad current is proportional to the gain. The ion backflow is estimated by dividing the background-corrected cathode current by the pad current.

The standard scan procedure is to collimate the x-rays with a $\varnothing = 10\,\text{mm}$ collimator and to proceed from point to point with a step size of 25 mm in x- and

[1] Transition Radiation Detector

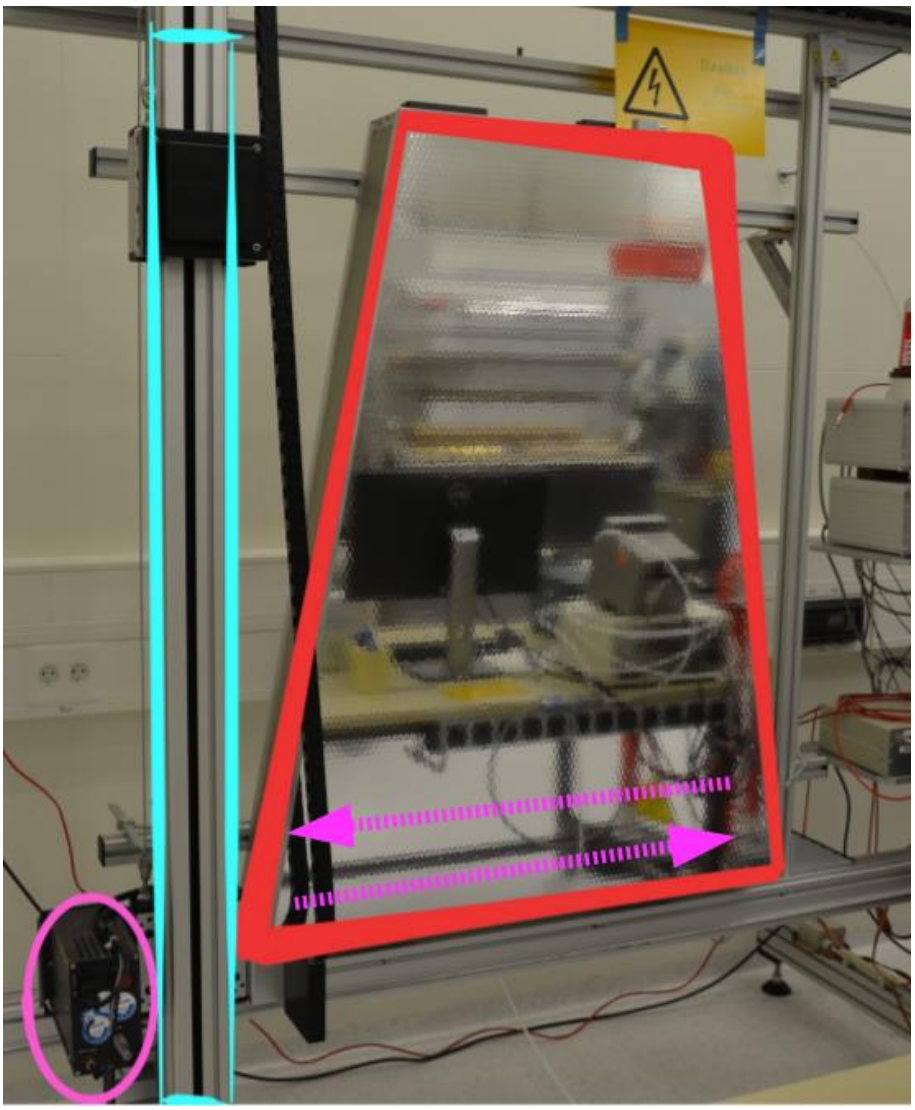

Figure 10.1: OROC (red) hanging vertically on the scanning test stand in the clean room. A radioactive source or an x-ray tube (pink) is mounted at the moveable arm (blue). The scan is performed by moving the source stepwise from one side to the other as indicated by the (pink) arrows.

y-direction. Optional finer scans are performed with steps of 10 mm, 5 mm, and 1 mm.

10.3 Gain uniformity measurements

The first two chambers, OROC/0 and OROC/1, were subject to several scans each in order to optimize the test procedure and to gain experience with the test setup. Table 10.1 lists all performed scans of these two chambers.

	Test No.	Step size	Colli-mator	Tube HV	source used	OROC1 ΔHV	OROC1 ΔHV	OROC3 ΔHV	Comment
OROC/0	1	50 mm	-	-	yes	+500 V	+500 V	+500 V	OROC gas: Ar-CO_2 (80-20)
	2	50 mm	none	5.5 kV	no	0 V	0 V	0 V	OROC gas: Ne-CO_2-N_2 (90-10-5)
	3	50 mm	none	6.4 kV	no	0 V	0 V	0 V	
	4/5	50 mm	none	7.0 kV	no	0 V	0 V	0 V	2 scans right after each other
	6	50 mm	none	6.4 kV	yes	0 V	0 V	0 V	Scan using tube and source
	7	50 mm	-	-	yes	0 V	0 V	0 V	
	8	25 mm	10 mm	10 kV	no	+50 V	+100 V	0 V	Scan with adjusted voltages
OROC/1	1	50 mm	none	6 kV	no	0 V	0 V	0 V	High O_2 level
	2	50 mm	10 mm	10 kV	no	0 V	0 V	0 V	Directly after scan above
	3	25 mm	10 mm	10 kV	no	+70 V	+100 V	+100 V	Voltage adjustments to match stack currents, high O_2 level
	4	25 mm	10 mm	10 kV	no	0 V	0 V	0 V	O_2 level under control
	5	25 mm	10 mm	10 kV	no	−50 V	−50 V	−50 V	
	6	25 mm	10 mm	10 kV	no	−50 V	−35 V	−50 V	
	7*	10 mm	5 mm	10 kV	no	−50 V	−25 V	−50 V	Only OROC3 scanned, striped pattern visible
	8	25 mm	10 mm	10 kV	no	−50 V	−25 V	−50 V	
	9	25 mm	10 mm	10 kV	no	0 V	0 V	0 V	New cathode, smaller drift gap, OROC rotated by 90°
	9s*	1 mm–25 mm	2.5 mm–10 mm	10 kV	no	0 V	0 V	0 V	Series of fine scans in OROC2 stack to analyze pattern
	10	20 mm	10 mm	10 kV	no	0 V	0 V	0 V	Modified step size to compare pattern
	11	25 mm	none	7 kV	no	0 V	0 V	0 V	No collimator to compare pattern
	12/13	25 mm	10 mm	10 kV	no	0 V	0 V	0 V	Waiting time of 1/2 s between steps

Table 10.1: Overview of all uniformity scans performed with OROC/0 and OROC/1. ΔHV reflect variations from nominal voltage applied to OROC stacks.
*: Scans that do not contain full chamber

Important findings of the tests concerned the need for precharging GEMs, the voltage adjustment for individual stacks to provide the same gain, the choice of proper step and collimator size and the design of a new cathode of the test box.

Based on the experience from these scan, a standard scan procedure was defined as follows. The scan should be performed with the x-ray tube HV of 10 kV, a collimator of $\varnothing = 10$ mm, and a step size of 25 mm. Before the first scan, the chamber should be precharged with the x-ray tube on 10 kV and without collimator.

Moreover, the timing details of curent measurement and the x-ray absorption in the test box will be discussed below.

The properties of the OROC/0 will be presented using the data of its 8th scan. It is the most detailed one and was performed with the later settled standard settings making it most comparable. In Fig. 10.2 the pad current for every measurement point is displayed in a 2-dimensional histogram.

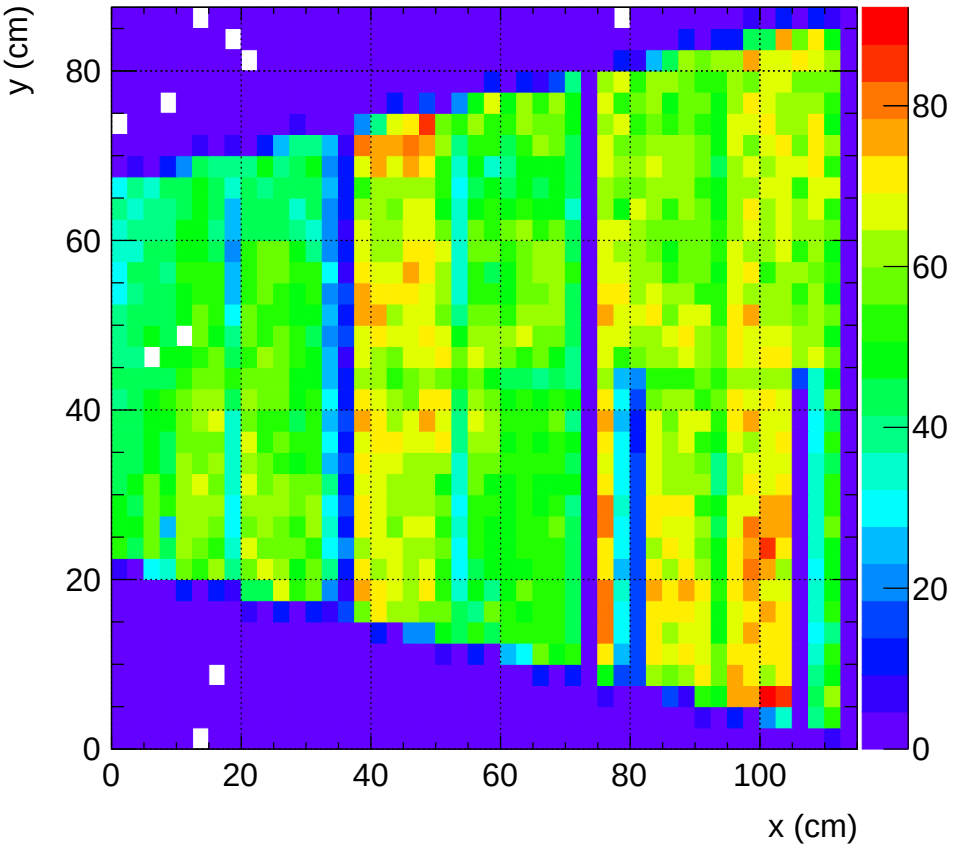

Figure 10.2: Gain uniformity scan of OROC/0. Pad current visualized in color scale given in nA. The two blue bars in OROC3 stack are caused by floating segments.

At first view, the gain is rather uniform except for some "hot" areas in the OROC2

and OROC3. In OROC3, there are two prominent blue bars which result from floating segments (see Section 8.3). The signal also vanishes at the stack bounderies, consisten with a 10 mm wide dead area resulting from the GEM frames. The reduced-gain stripes crossing the stacks in the middle come from the supporting frames of the foils (width 2 mm check this!).

To quantify the uniformity of the chamber, the pad current values are filled in one-dimensional histograms as shown in Fig. 10.3. This is done after applying a cut excluding values with a current below 35 nA to confine the analysis on functioning parts of the OROC and exclude the intermediate region and floating segments. The supporting cross, however, is tried to keep inside the values since it is a permanent intrinsic part of the chamber.

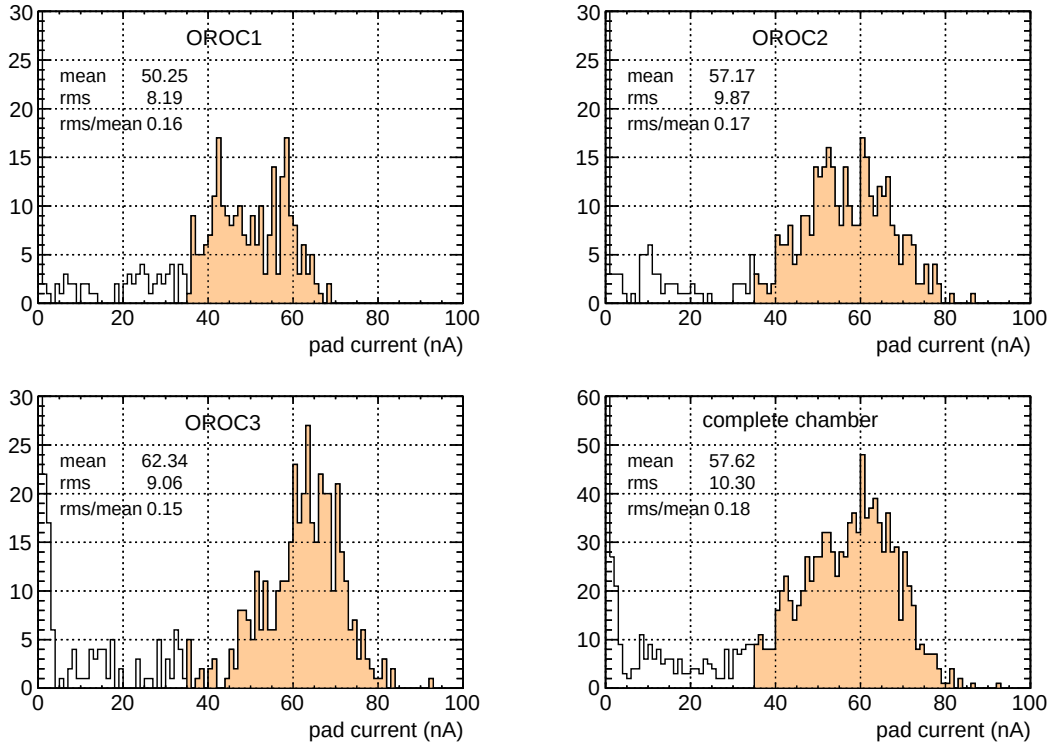

Figure 10.3: Pad current distribution of OROC/0 split into individual stacks and the complete chamber. The RMS is calculated for pad current > 35 nA.

The main result is that the nonuniformity of the chamber, quantified by the RMS/mean rato is below the critical value of 20 %. This chamber passes the uniformity test. The result of 18 % could be further improved by readjusting the applied voltages. As specified in Table 10.1, OROC1-2 were already operated with increased voltages. In particular, OROC1 requires a further increase to match the gain of OROC3. The previously defined adjustment depends on the point where the gain curve was measured. Hitting a spot with higher gain lead to an overestimate of the gain of the stack. For future tests, the stack voltages will be optimized iteratively.

The next step is the estimate of the IBF of the chamber. For this purpose, the cathode current is first corrected for the dark current. The correction is found by plotting measurement points which are outside of the chamber active area versus x- and y-axis and parametrizing for dependencies of first and second order. The mean dark current was around 5.7 nA. For the x-axis (corresponding to the inverse time axis since the test was performed from OROC3 to OROC1) the variation is 0.8 nA and thus higher than the extracted ion signal itself which is below 0.4 nA. The corrected IBF values are then again displayed in histograms shown in Fig. 10.4.

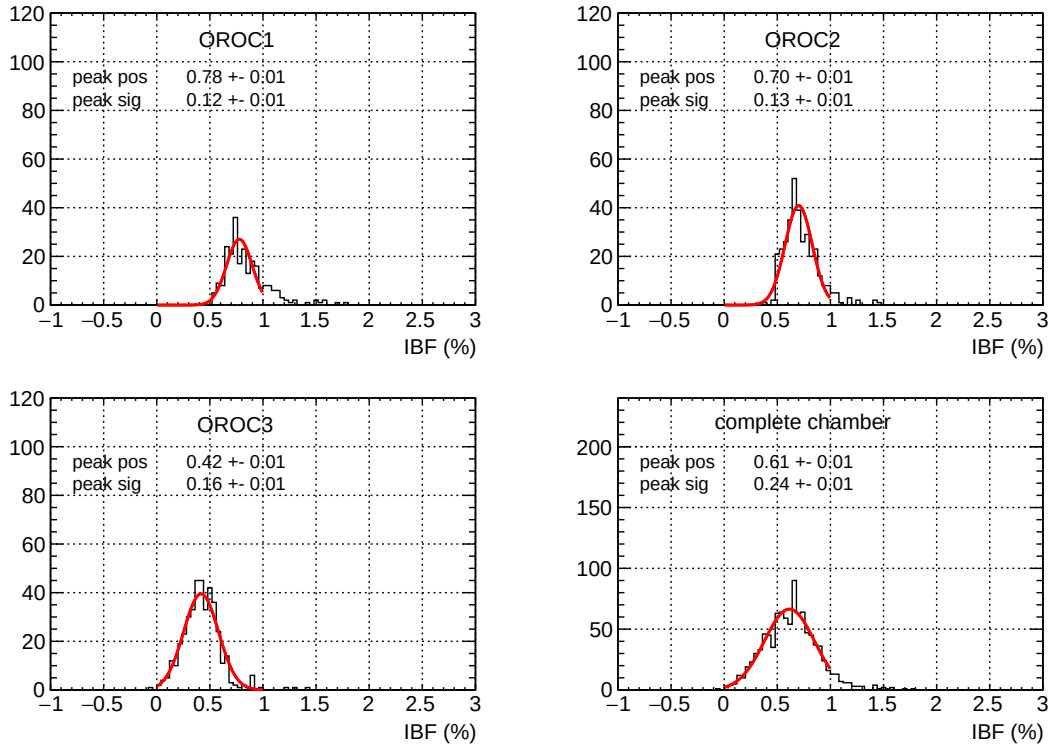

Figure 10.4: Ion backflow ($I_{cathode}/I_{pad}$) distribution of OROC/0. The same cut of pad current > 35 nA is applied. The cathode current is corrected for the dark current.

The GEM gain can be affected by large area fluctuations due to etching and is therefore not necessarily Gaussian. This does not apply to the IBF since for a higher gain, more electrons and ions are liberated in equal amounts. Thus, the position of the IBF peak is determined via a Gaussian fit. The mean IBF is around 0.6 %, clearly below the limit of 1 %. Besides, there are only few outlier exceeding this level. All in all, this is a promising result that confirms that the ion blocking in the GEM stacks works sufficiently well.

Next, the OROC/1 results will be presented. The measurement and analysis proceedure remained the same and will not be described in detail. The 8th scan (see

Table 10.1) of this chamber is chosen since it has the best voltage adjustments. Later tests, with the modified cathode, were performed without these adjustments because they were meant to optimize the test box or to investigate the x-ray absorptio only.

The gain uniformity scan is displayed in Fig. 10.5. The OROC3 stack shows increased gain in one half of the stack. A look into the data from optical scans in Helsinki showed a smaller hole diameter in one foil in the corresponding region.

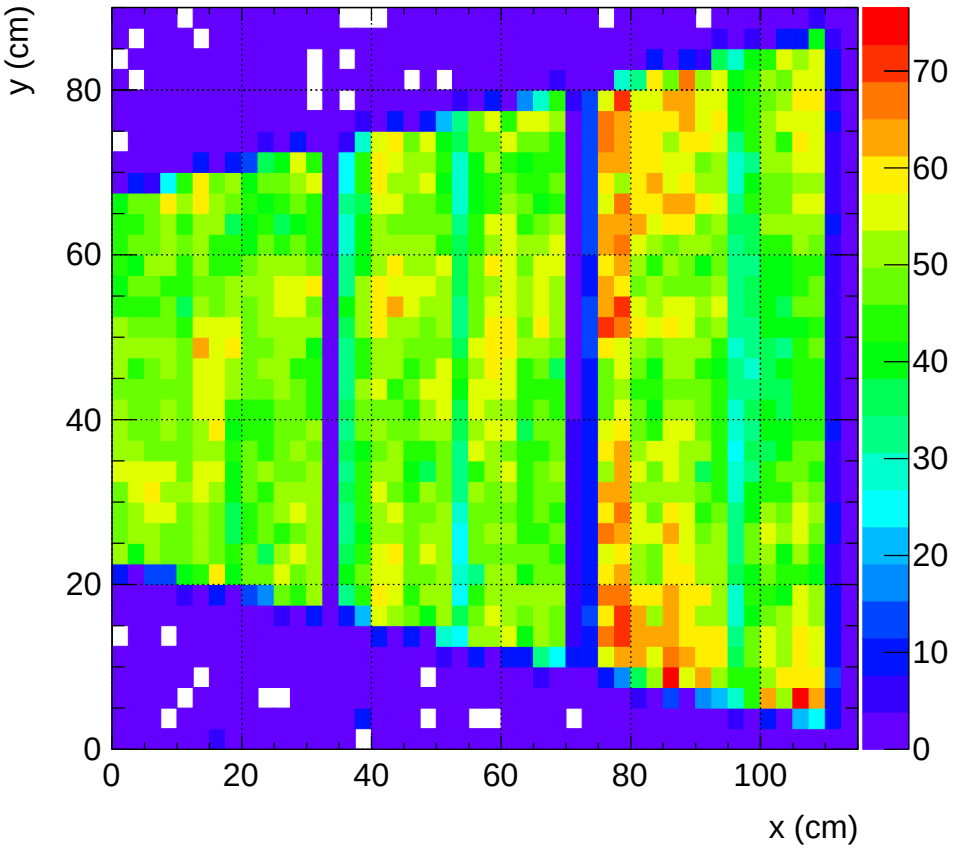

Figure 10.5: Gain uniformity scan of OROC/1. Pad current visualized in color scale given in nA.

The uniformity of OROC3 is strongly affected by the above mentioned "hot" area that broadens the signal distribution (Fig. 10.6). The optical data was not yet accessible while assembling this chamber which would potentially have led to the exclusion of the foil. The stack anyhow fulfills the requirement hitting the limit of 20 %. In OROC2, the separation of the bin entries that are affected by the supporting cross is rather prominent resulting in the small bump left of the main peak. The reason is probably that the measurement points and the cross happen to overlap for OROC2 while for the other stacks the 2 mm thin structure was not irradiated directly. The most uniform distribution is provided by the OROC1 stack

with an RMS/mean of only 10 %. The overall RMS/mean of the complete chamber is 17 %, fulfilling the requirements and comparable to the OROC/0.

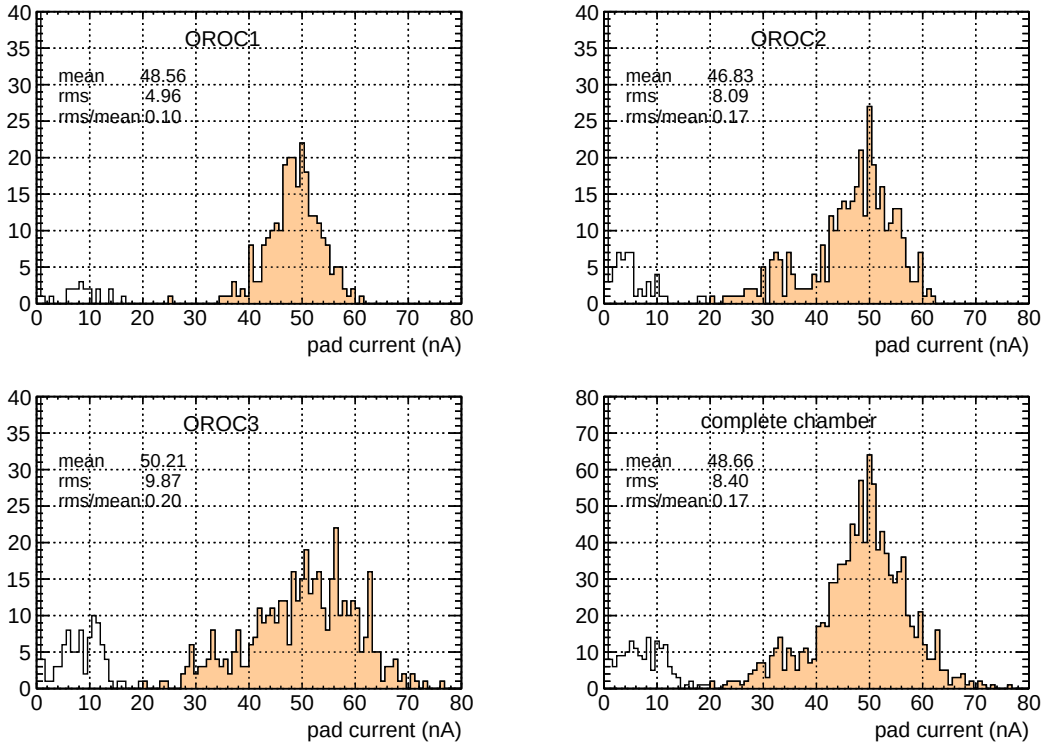

Figure 10.6: Pad current distribution OROC/1 split into individual stacks and the complete chamber. The RMS is calculated for pad current $> 20\,\mathrm{nA}$.

The IBF estimate for the OROC/1 has a comparable outcome as for the OROC/0. The IBF of the complete chamber is again around 0.6 % (Fig. 10.7). In case of the OROC/1, the IBF distribution was much sharper than for the OROC/0. This could be probably traced back to the correction of the cathode current which was smaller for the scan of the OROC/1.

Thus, the scans showed that both chambers, produced at GSI, fulfill the requirements with an RMS/mean of 18 % and 17 % and an IBF of 0.61 % and 0.63 %, respectively. The OROC/1 was also tested with the modified test box with two cathodes which led to eliminating dark current and a somewhat improved resolution of the IBF measurement. The settings demonstrated to suit for tests of OROCs and will be adopted for the tests during mass production.

10.4 Absorption of x-rays in the testbox wall

From the first uniformity scan on, the live monitoring of the current indicated that a periodic structure is present in the scanning data (Fig. 10.8).

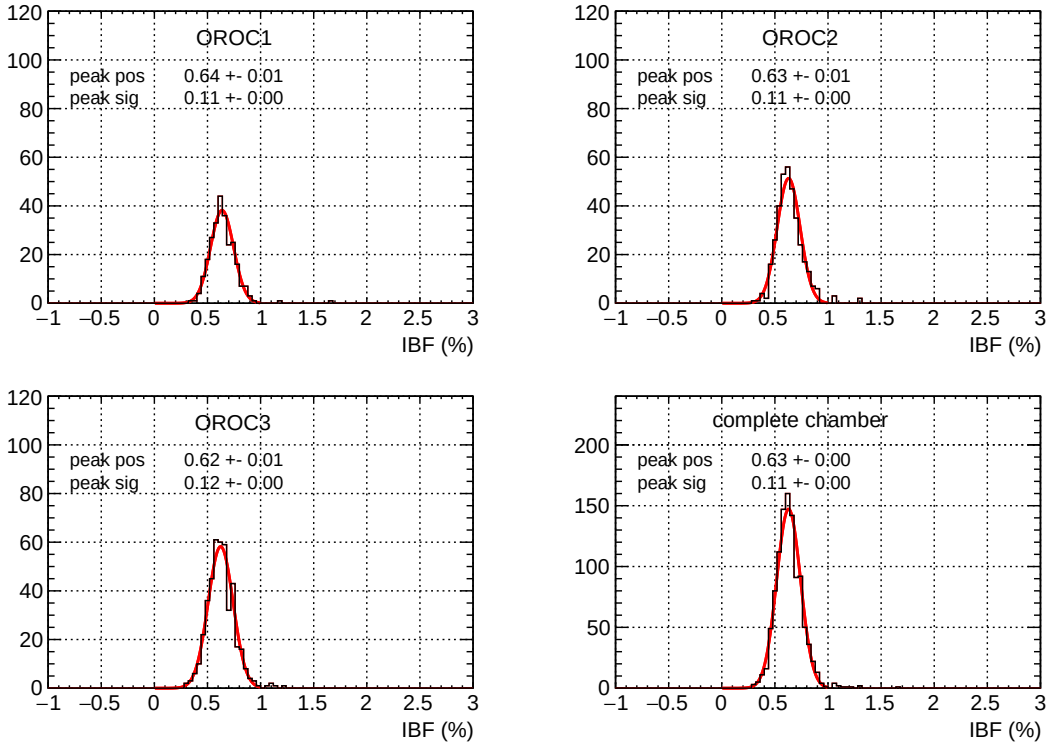

Figure 10.7: Ion backflow ($I_{cathode}/I_{pad}$) distribution of OROC/1. The same cut of pad current $> 20\,\text{nA}$ is applied. The cathode current is corrected for the dark current.

Both discussed uniformity scans were performed with the standard step size of 25 mm. In order to study the observed structure, a scan of OROC3 with smaller step size of 10 mm was performed for the outermost part of the OROC3 stack (No. 7 in Table 10.1). The result is displayed in Fig. 10.9 and shows very clearly the periodic substructure.

Following eddects were considered as a potential cause:

- strong irregularity in gain of GEM foils
- instability of x-ray tube
- movement of motor
- honeycomb structure of test box which absorbs radiation

It seems to be implausible that this structure results from intrinsic gain irregularities of the GEM foils. They pass through a detailed quality assurance procedure and the hole-size distribution of a GEM is not allowed to be too wide. Additionally, the observed fluctuations of the hole size were of large extension and not periodic.

The instability of the x-ray tube as a candidate is questionable as well. The changes occur rapidly (within a second) and the fluctuation is rather strong – the

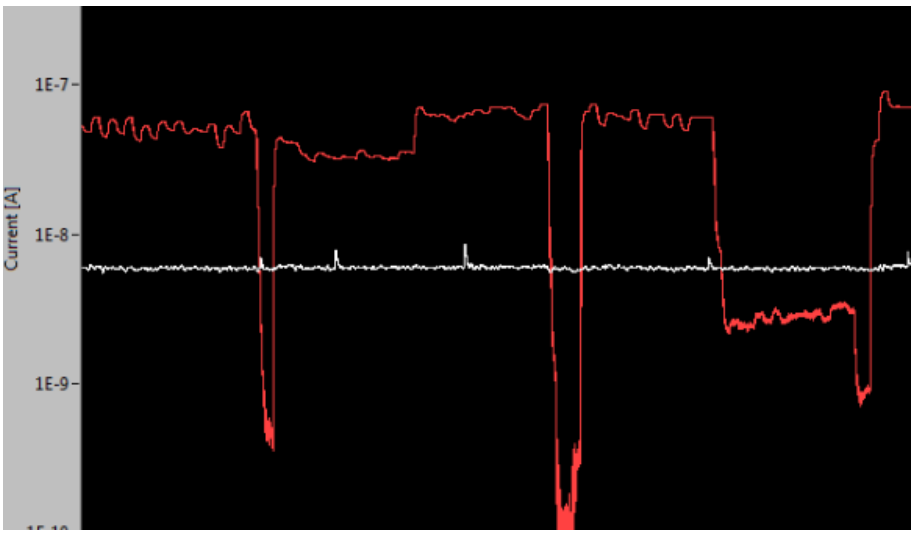

Figure 10.8: Pad current live-monitoring (red) during x-ray irradiation while moving the source. The different levels of the plateaus result from varying gain of the stacks. Inside the plateau, a substructure appears which is the topic of investigation.

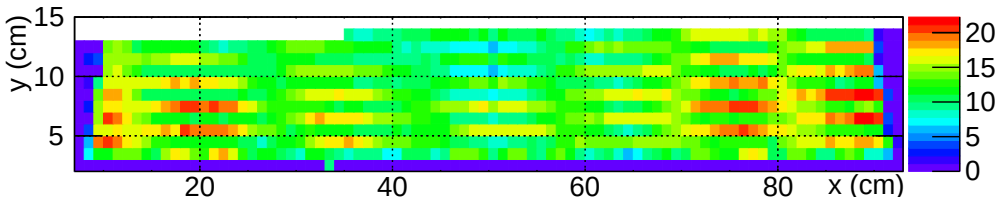

Figure 10.9: Fine uniformity scan of outermost part of OROC3 stack of OROC/1. Step size = 10 mm, collimator diameter = 5 mm.

pad current drops to half the value and jumps back to the original one. Moreover, the pattern changed with the step size which is not directly related to the x-ray source.

The influence of the motor was excluded because the result of the scan remained unchanged after the OROC was rotated by 90°. (This modification of the setup was dictated by mechanical and procedural reasons.) The measurement was repeated with the same scan settings. In Fig. 10.10 the pattern of the previous measurement reappears. The x-ray tube moves always horizontally and at the border of the scan region one step upwards. Anyway, the orientation of the pattern rotates like the chamber by 90°. There is clear evidence that the motion of the motor does not explain this effect.

Finally, the influence of the honeycomb structure of the entrance window was tested by further decreasing the step size and the diameter of the collimator. A first approach using a step size of 5 mm and a 5 mm collimator (Fig. 10.12) shows already a regular pattern of spots with high current.

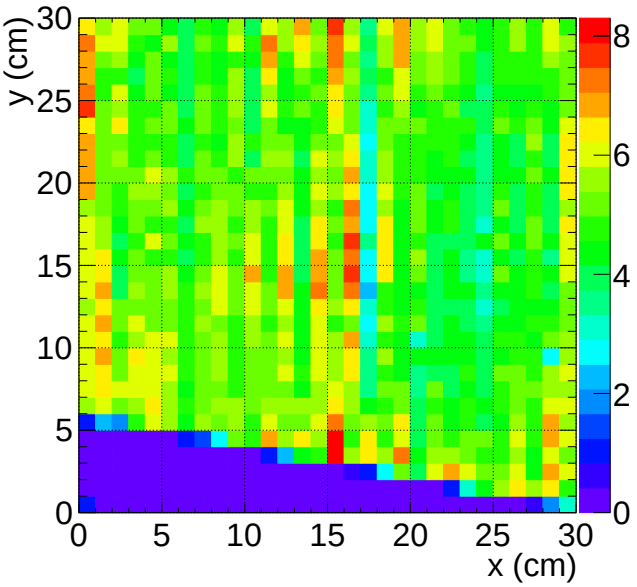

Figure 10.10: Uniformity scan of part of OROC2 stack of the rotated (90°) OROC/1. Step size = 10 mm, collimator diameter = 5 mm. Pattern from Fig. 10.9 reappears but is rotated.

Figure 10.11: Carbon fibre honeycomb plates of different size between two Rohacell plates.

The suspicion is that these spots represent the cells of the honeycomb while the rest of the area has a reduced current due to x-ray absorption in the walls of the honeycomb. A closer look with a step size of 1 mm and an even smaller collimator of 2.5 mm diameter reveals a detailed image of the structure (Fig. 10.13). The image corresponds to the convolution of the hexagonal structure. The maxima appear nearly circular but the hexagonal shape is still recognizable through the light blue spots with lowermost gain.

This shows that the entrace wall of the test box has an underlying structure which influences the signal strength. With a small collimator (2.5 mm) the signal is decreased by more than a factor 2 at the area of the walls. The relevant question

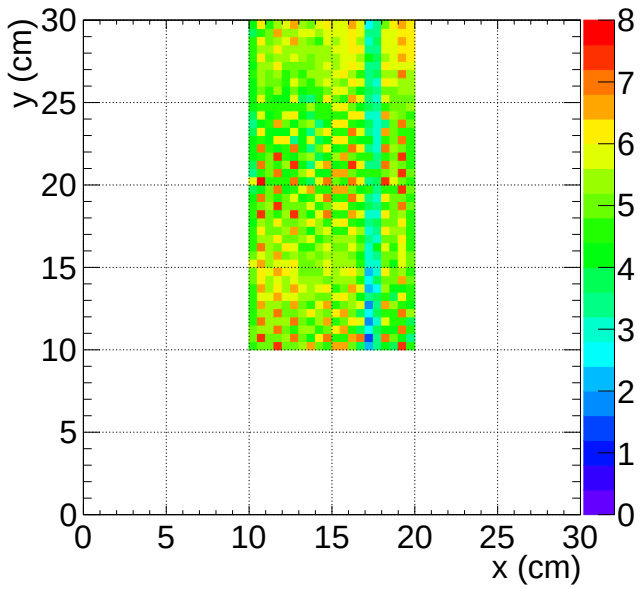

Figure 10.12: Uniformity scan of part of OROC2 stack of OROC/1.
Step size = 5 mm, collimator diameter = 5 mm. Regular spots with increased current visible.

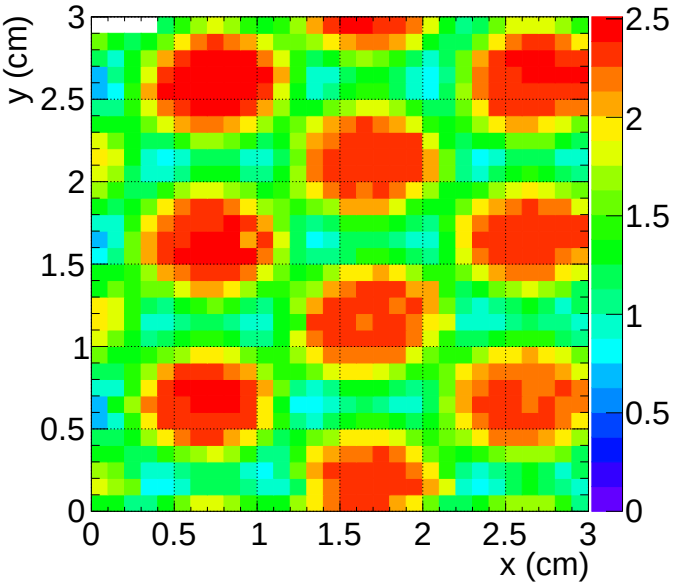

Figure 10.13: Uniformity scan of OROC/1 that resolves the honeycomb structure.
Step size = 1 mm, collimator diameter = 2.5 mm.

is now if and how this affects the final scan with its larger step size and collimator diameter. A potential problem could be that, since the step size and the size of a unit cell of the structure do not fit, a beating effect occurs. The consequence

would be that there are "hot" regions where the collimator is centering a hexagon and "cold" region where the collimator faces a honeycomb wall. This effect and its influence on the result of the RMS measurement of the chamber will be analyzed in detail in the next section (10.5).

10.5 Simulation of the signal deterioration by the test box

The uniformity scan in Fig. 10.13 reveals that the honeycomb structure of the test box entrance wall absorbs a significant amount of x-rays. The main question is how strong the influence of this structure is on the uniformity measurement. In particular one expects a beating effect caused by the difference between the honeycomb period and the step size of our scans. The scans were performed with a step size of 25 mm in case of a standard scan or 10 mm for a fine scan. The unit cell of the hexagonal structure of the honeycomb is (19 mm,9.5 mm).

To estimate the effect, the hexagonal pattern and a collimator were simulated in ROOT [28]. A first step is to model the honeycomb cell which can easily be multiplicated. This approach led to a pixeled honeycomb structure on graph paper which was then transferred into a 2D histogram. This structure can be multiplicated and filled into an arbitrarily large histogram (Fig. 10.14). Every bin corresponds to a $0.5 \times 0.5\,\mathrm{mm}^2$ large area. The bin content of wall-free area is set to 1 (no absorption), for walls it can be adjusted by comparing to the measurement.

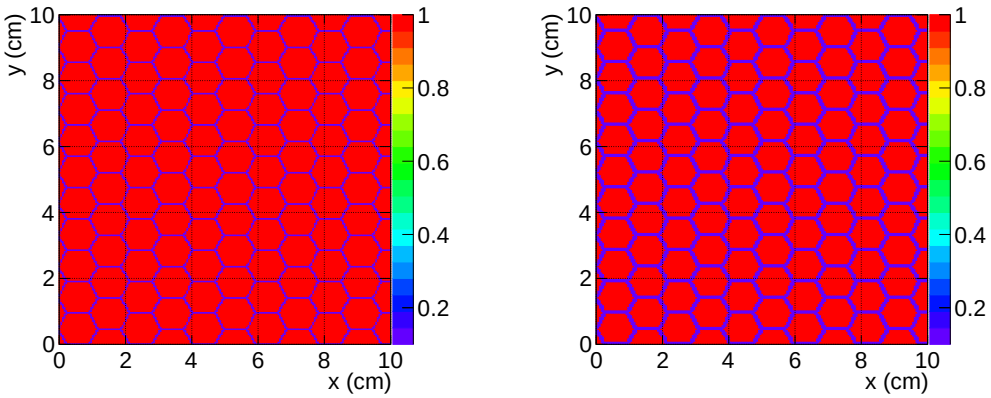

(a) wall thickness ≈ 0.5 mm

(b) wall thickness ≈ 1 mm

Figure 10.14: Simulated hexagonal structure with different wall thicknesses, with transmission factor of the wall of 10 %.

Different collimators can be defined to study how their size influences the signal. The collimator is simply defined in another histogram by setting the bin content covering its area to unity (Fig. 10.15). The simulation works as follows:

The pattern histogram is scanned by a collimator (size can defined arbitrarily). The bin content of the pattern is summed up for the area covered by the collimator. This number is stored as a bin at the position of the collimator in a result histogram. The collimator is moved then by the defined step size. This results in a map of convolution of the hexagonal pattern which depends on shape and size of the collimator. Each bin corresponds to a measurement point which was irradiated after moving the source.

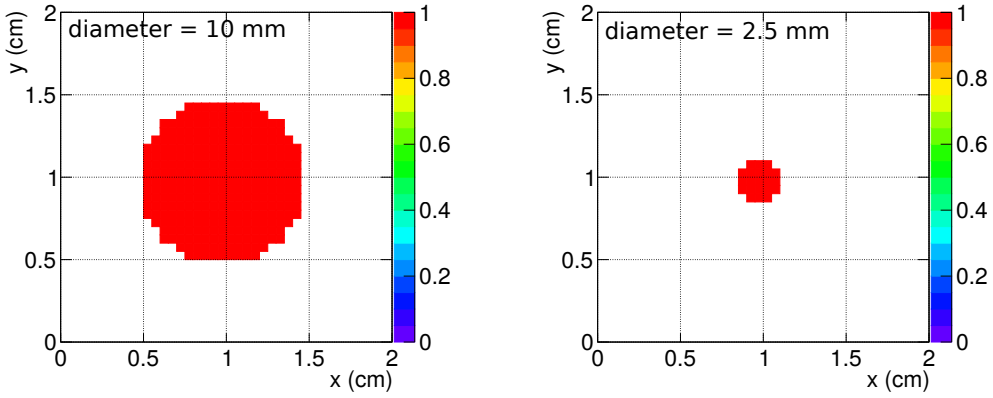

Figure 10.15: Simulated circular collimators of different diameters.

This simulated scan can be performed for a small $10 \times 10\,\mathrm{cm}^2$ model area with a small step size of 1 mm. In principle, the simulation moving the collimator always by two bins (2 bins $\equiv$ 1 mm) should generate approximately the same result as the fine scan shown in Fig. 10.13. This simulation allows to adjust the transmission factor of the walls to match the measurement.

In the next step, the simulation is performed for a full size chamber ($\mathcal{O}$(m)). This will give an idea of how strong the effect of the honeycomb structure is. The pattern histogram itself has no gain irregularities. This means that the RMS/mean of the simulated scan gives the contribution of the entrance wall of the test box on the RMS/mean value of the gain uniformity measurement.

The aim is to get simulation and measurement into agreement. Parameters which are adjustable are the transmission factor of the walls and the wall thickness – the latter implies a remake of the hand drawn sketch.

The first approach shown in Fig. 10.14(a) represents a honeycomb structure with a wall thickness of one pixel (0.5 mm) and a transmission factor set arbitrarily to 0.1 for the wall. The best suitable comparative measurement is the fine scan with collimator size of 2.5 mm diameter and step size of 1 mm, again displayed in Fig. 10.16(a). The comparison of simulation and measurement in Fig. 10.16(b) suggests that the simulated walls are too thin. The thickness of the honeycomb paper was estimated by our colleagues from Bucharest to be below 0.3 mm. The honeycomb, however, is glued on both sides to Rohacell plates. This glue joint increases the effective

thickness. This motivated the remake of the hexagonal pattern with walls of 1 mm thickness (Fig. 10.14(b)).

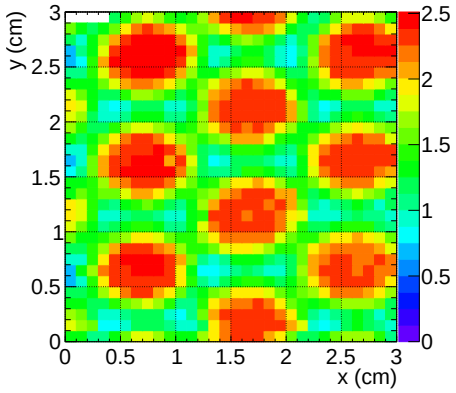

(a) Measurement

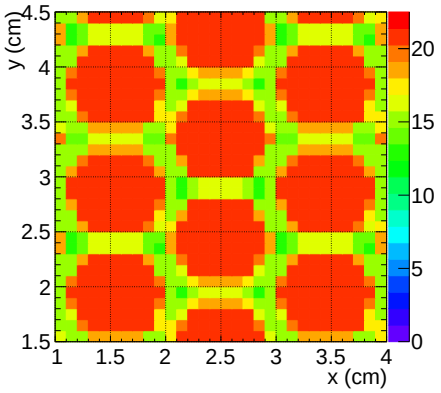

(b) Simulation with 0.5 mm thick walls and 10 % transmission

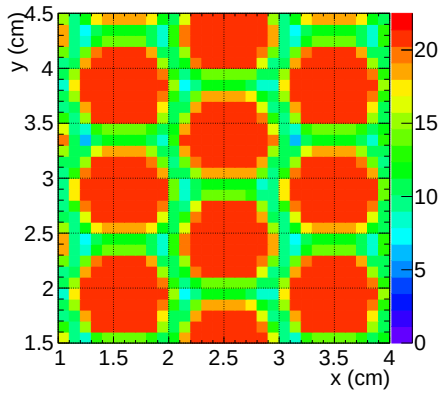

(c) Simulation with 1 mm thick walls and 10 % transmission

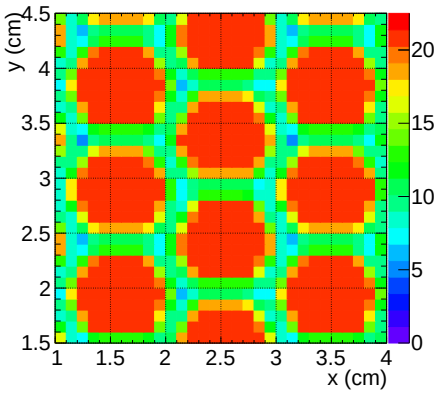

(d) Simulation with 1 mm thick walls and 0 % transmission

Figure 10.16: Comparison of measurement (a) and simulations (b-d) of fine scan resolving honeycomb structure. The simulations have as input different wall thicknesses and transmission factors for the wall.

The simulation was repeated with the remade hexagonal pattern with thicker walls. The outcome, displayed in Fig. 10.16(c), closely resembles the measurement. The gain is reduced by a factor two in the region of the walls. The bright blue corner points of the hexagon and the rounded red area are clearly reproduced. However, the size of the red spots is larger and the gain reduction is slightly too low compared to the measurement. This lead me repeat the simulation with a transmission factor of 0.0 for the walls (Fig. 10.16(d)). This simulation is consistent to the measurement exept for the size of the red spots. The size, however, can at least be partly explained by the shape of the simulated collimator. In Fig. 10.15 one sees that for such small sizes, the simulation does not represent a “good” circle. The area is 7 %

larger than of a circle of 2.5 mm diameter. Decreasing the bin size would would cause a disproportional computing time. Besides, this effect will carry less weight for the scan simulation using a 10 mm collimator.

The next part is the simulation of an actual scan of a complete chamber. The honeycomb structure designed previously is multiplicated over an area of $100 \times 100\,\mathrm{cm}^2$ (corresponding roughly to the extent of an OROC; cf. chapter 4). The working principle of the convolution is kept, the only change is the larger overall size and the fact that only distinct spots are calculated.

The simulation was performed as the normal scan with a step size of 25 mm and a 10 mm collimator. The output (Fig. 10.17(b)) shows indeed a vertically striped pattern where stripes with high transmission recur every 75 mm. This is silimar compared to the real scan in Fig. 10.17(a). Stripes with increased gain seem to reappear after 100 mm which would be consistent with the simulation.

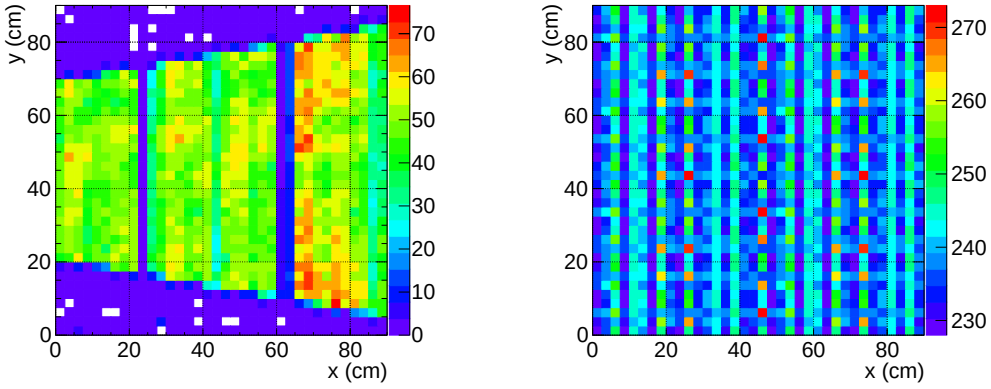

(a) Measurement (b) Simulation

Figure 10.17: Measurement (a) and simulation (b) of uniformity scan. Step size = 25 mm, collimator diameter = 10 mm.

The validity of the hypothesis of the honeycomb as the origin of the pattern becomes even more evident looking at a finer scan with a step size of 10 mm (Fig. 10.18). The simulated scan performed with the same settings shows a comparable outcome. The stripes recur every second bin. Additionally, there are centers of increased gain every 200 mm.

Turning now to the quantification of the effect of the honeycomb structure on the uniformity extracted from the scans. The simulated standard scan with a step size of 25 mm and a 10 mm collimator has an RMS/mean of 3.31 %. In contrast, the measurements had an RMS/mean of 17–18 %. An exemplary calculation shows that, for an intrinsic contribution of the chamber of 18 %, the honeycomb structure would increase the measured value only to 18.3 %, a relative change of less than 2 %. The influence of the honeycomb structure thus seems to be negligible compared to the actual nonuniformities of OROCs.

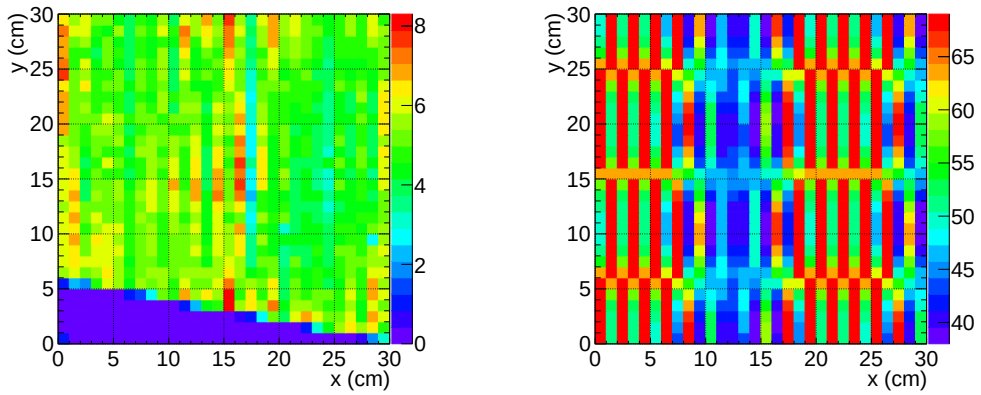

(a) Measurement (b) Simulation

Figure 10.18: Simulation (a) and measurement (b) of uniformity scan. Step size = 10 mm, collimator diameter = 5 mm.

To get an overview of the dependence on the step size, the simulations were also performed with varying step size from 10–30 mm to check if there are more optimal settings or some which should definitely be avoided. In Table 10.2 the RMS/mean values for step size variation are contained. The variations are not strong. The choice of step size could be motivated by a more esthetical question meaning if one wants to avoid the prominent striped pattern like e.g. for 10 mm. The RMS/mean, the measure of non-uniformity, is not affected in the end. Larger step sizes have the advantage of much shorter measurement time. Thus, the step size of 25 mm seems to be the preferable choice. The effect on the uniformity is low and the duration of a scan is much shorter than for smaller step sizes which will be relevant for mass production.

step size	$\Delta y = 10$ mm	15 mm	20 mm	25 mm	30 mm
$\Delta x = 10$ mm	3.41 %	3.30 %	3.29 %	3.30 %	3.40 %
15 mm	3.39 %	3.28 %	3.29 %	3.29 %	3.38 %
20 mm	3.41 %	3.29 %	3.32 %	3.31 %	3.40 %
25 mm	3.41 %	3.29 %	3.31 %	3.31 %	3.39 %
30 mm	3.42 %	3.31 %	3.30 %	3.31 %	3.41 %

Table 10.2: RMS/mean values (in %) for simulated uniformity scans varying the step size (columns with same x-, rows with same y-coordinate).

One additional part of the simulation series was the survey of how much the RMS/mean value depends on the collimator size. Since the overall effect on the nonuniformity of the scans is negligible, this part is presented briefly and only for the defined standard settings of 25 mm in x- and y-direction. In Table 10.3, the

RMS/mean values for this collimator size variation are contained. The used collimator with $\varnothing = 10\,\text{mm}$ was an appropriate choice since its contribution to RMS/mean is already small. For smaller collimators, this is not the case. Already a collimator with $\varnothing = 7.5\,\text{mm}$ has a non-negligible RMS/mean value of 9.6 %. For even smaller collimators, the non-uniformtity induced by the test box entrance window and the collimator exceed the values of the performed scans. On the other side, the change of RMS/mean going to larger collimators carries no weight. Besides, collimators that are larger than the step size would falsify the measurement since the measurment points would get correlated.

The simulations showed that the $\varnothing = 10\,\text{mm}$ collimator is satisfying for our purposes. The measured uniformity with smaller collimators is deteriorated strongly and should not be used for uniformity estimates of a chamber.

$\varnothing$ collimator	**RMS/mean**
2.5 mm	30.5 %
5 mm	19.4 %
7.5 mm	9.6 %
10 mm	3.3 %
15 mm	3.5 %
20 mm	1.2 %

Table 10.3: RMS/mean values (in %) for simulated uniformity scans varying the colimator diameter. Step size was kept constant to 25 mm in x- and y-direction

11 Irradiation test

All chambers have to demonstrate their high-irradiation capability before operating them in the TPC. The respective test will be performed already in the clean room at GSI. Each chamber will be illuminated for several hours with x-rays producing a pad current of 10 nA/cm^2 which corresponds to the maximal expected dose rate in ALICE in Run 3 as discussed in section 4.5.

11.1 Test setup

The irradiation tests are performed in a lead-coated shielding box (Fig. 11.1) developed to test modules for the PANDA experiment[1] and adapted by the ALICE group. Two x-ray tubes of type Mini-X (Fig. 11.3; specifications in App. A.3), mounted inside the box, irradiate the whole area of the OROC. The chamber is attached horizontally on the door of the shielding box (Fig. 11.2). The GEM stacks are connected to the HV supply via voltage dividers. The gas supply and monitoring is provided by the same devices as used for the measurements discussed in chapters 9 and 10.

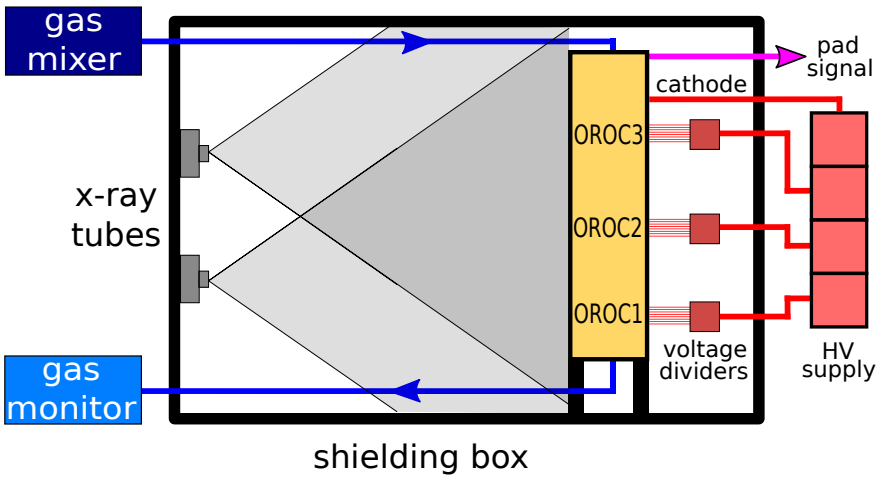

Figure 11.1: Functional sketch of the x-ray irradiation test setup. The OROC (orange) is irradiated by two x-ray tubes (grey). The chamber is connected to the gas system (blue). Each stack is connected via voltage dividers and the cathode directly to the HV supply (red).

[1] Anti-**P**roton **AN**nihilation at **DA**rmstadt

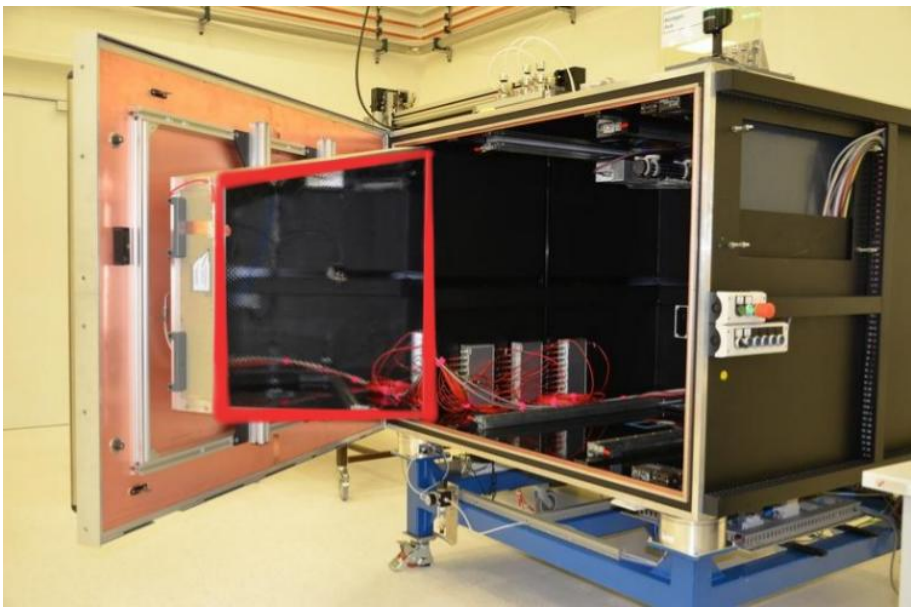

Figure 11.2: Lead-coated shielding box for x-ray irradiation tests in the clean room. The OROC (marked red) is mounted on front door. Two x-ray tubes are placed in the back (cf. Fig. 11.3).

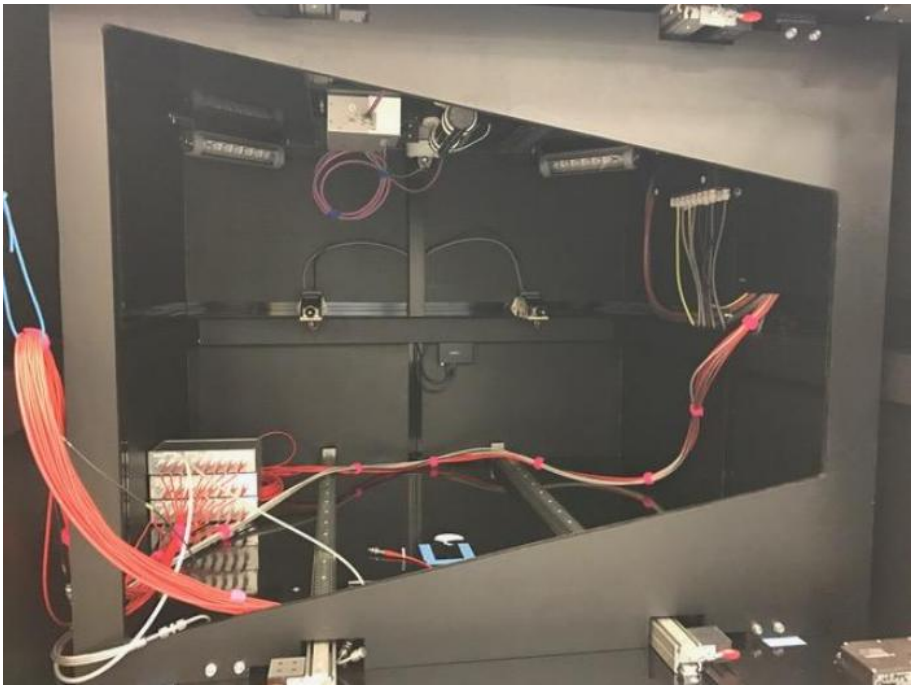

Figure 11.3: View from the door to inside of shielding box. Optional trapezoidal passepartout can be used to protect the edges of the OROC test box. In the back, the two x-ray tubes are mounted.

11.2 Measurement method

The nominal voltage is applied to the OROC. First, the functionality of the three stacks is checked with a ^{55}Fe source. The spectrum is measured and the resolution of the chamber is determined. Then the shielding box is closed and the x-ray generators are turned on slowly and their intensity is increased until a pad current of $\sim 70\,\mu A$ is reached[2]. This corresponds to a current density of $10\,nA/cm^2$. The test is allowed to run for several hours during which the pad and cathode current are being monitored. After the test is finished, the resolution of the chamber is checked again.

11.3 Results

A first test run with OROC/0 showed stable conditions. However, the chamber had to be operated with increased voltage by 200 V to attain $10\,nA/cm^2$ despite full power of x-ray tubes. It was found that the illumination region of the tubes was restricted to two circles of 50 cm diameter due to screw-on nickel plated brass covers. The test was repeated without those covers. The required current was now reached with the generators operating at 75 % of their maximum power. This change, however, was followed by the appearance of many spikes in the pad current with a rate of 10–50 per hour.

The origin of the effect seemed to be linked to the larger illuminated area and not to the OROC itself. In the first test, the irradiated part of the chamber held even stronger irradiation without instabilities. It was conjectured that the spikes were induced by the irradiation of the border area of the test box or the voltage dividers.

To study if discharges inside the GEM stacks could be excluded as the origin, a test run with full cathode voltage and decreased GEM voltage was performed. The GEM voltage was around 70 % of the nominal one. Again, spikes appeared with a comparable frequency. At this voltage, there should be no noteworthy amplification in the GEMs. This indicates that indeed the effect originates from a different source.

The next investigation step was the installation of a passepartout (Fig. 11.3) to ensure that only the OROC is irradiated. With the wood-lead passepartout, the spikes disappeared. Removing the passepartout resulted in the reappearance of the spikes.

This measurement showed that the OROC is stable under the required irradiation but the test box is not. For the tests planned in the ALICE cavern and the CERN Proton Synchrotron (PS), the passepartout solution is not sufficient and the test box had to be modified. The suspicion is that in the border area charges accumulate provoking discharges between cathode and ground. The solution was to use a suspended cathode in the 16 mm drift gap. The old cathode remained on the wall of the test box (Fig. 11.4).

[2]The active area covered by pads is $6873.6\,cm^2$ for an OROC; 6656 pads with $6\times10\,mm^2$ and 3200 pads with $6\times15\,mm^2$ area [14].

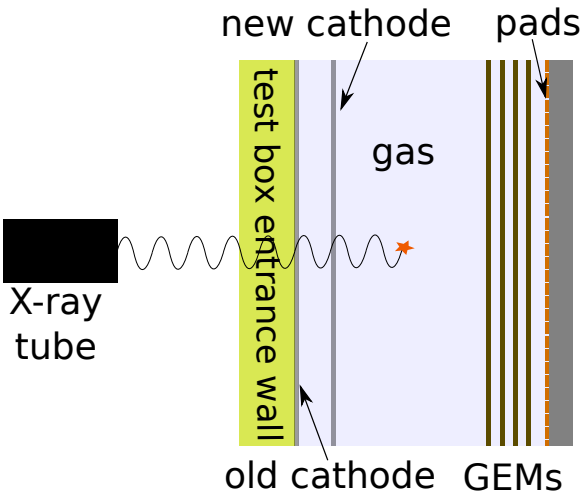

Figure 11.4: Sketch of test box with two cathodes. Old cathode is attached directly on the entrance wall of the test box, new cathode is suspended in gas volume.

The first positive side-effect was that the high dark current of the old cathode of several nA disappeared. Thus, the accuracy of the ion backflow measurement, where the current appears as an offset value, could be improved.

In the irradiation test, the new cathode proved its functionality. Still, aew spikes (Fig. 11.5) appear when the new reduced nominal voltage (smaller drift gap) is applied to both cathodes without passepartout.

Reducing the voltage of the old cathode to half the value, let the spikes in the measurement without passepartout vanish (Fig. 11.6). The current of the old cathode still showed regular spikes but neither the new cathode nor the pad current are affected by this.

According to that, employing the modified test box, OROCs can be checked for their ability to sustain the conditions expected in ALICE. The already existing chambers showed the capability to hold the corresponding irradiation. However, an advanced version of this test is to put the chamber into the ALICE cavern close to the beam line. This was done with this chamber and is discussed in the next chapter.

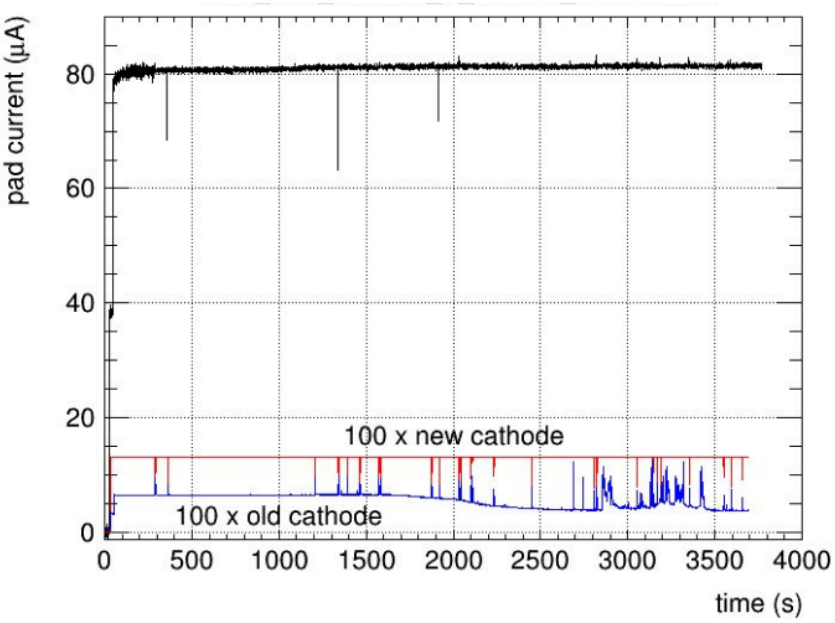

Figure 11.5: Pad current of the OROC/1 (black) and current of both cathodes (colored) monitored under irradiation in shielding box. Current of new cathode in saturation of device (130 µA). New suspended and old cathode on 3960 V. Few spikes are visible in pad current.

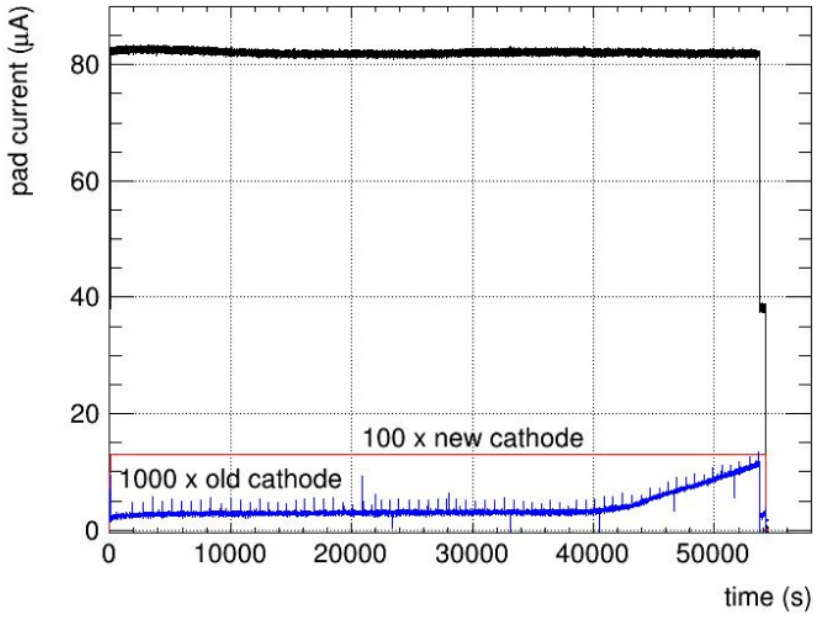

Figure 11.6: Pad current of the OROC/1 (black) and current of both cathodes (colored) monitored under irradiation in shielding box. Current of new cathode in saturation of device (130 µA). New suspended cathode on 3960 V. The voltage of the old cathode is reduced to 50 %. No spikes in pad current are seen.

12 Operation in the ALICE cavern

Charged particles traversing GEMs nearly perpendicularly to their surface produce an excessively high charge density which may lead to a discharge. To test the stability of the produced OROCs it is foreseen to install some of them at the experiment at Point 2 of the LHC. The first OROC, OROC/1, was transported to CERN after the measurements at GSI, moved down into the pit and placed close to the beam line (Fig. 12.1). According to the current estimates, the rate of charged particles traversing GEMs at this location at the nominal p-p interaction rate of 160 kHz, is 5-10 times higher than the one expected in the TPC in Run 3.

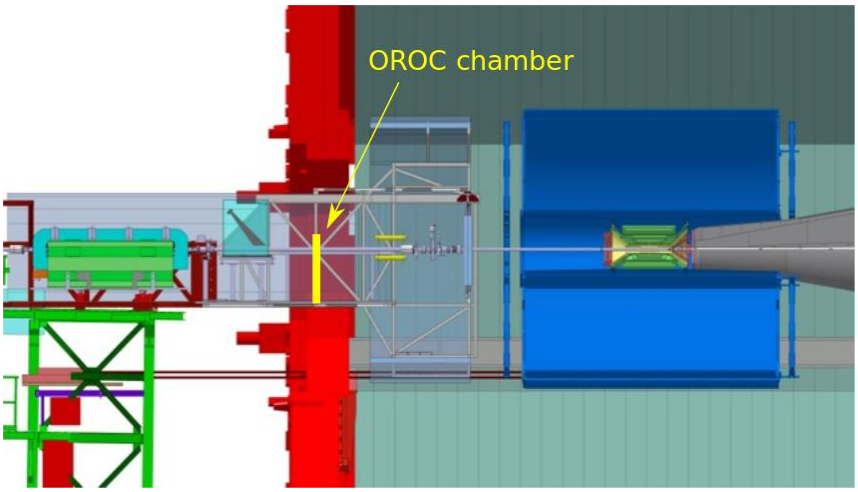

Figure 12.1: OROC (yellow) placed in miniframe of ALICE experiment. The TPC is displayed in blue on the right side, the vertical red structure is the L3 magnet [29].

The chamber was powered by power supplies located in counting room 4. Several different powering options were tried, including voltage dividers and cascaded power supplies from two different producers. The different voltage sets A and B (Table 12.1) were compared. In the beginning, the HV settings B with lower fields and powering via voltage dividers were chosen. The chamber was first ramped up to a moderate voltage – around 90 % of the nominal voltage. The chamber was filled with air instead of Ne and the p-p collision rate in ALICE was 150 kHz. In other words, no amplification was expected at this voltage in air. This precaution stage serves to check if all components hold the high voltage. Under these conditions, no sparks or discharges were detected.

Electrode	Voltage	Electrode	Voltage
Drift	400 V cm^{-1}	Drift	400 V cm^{-1}
GEM1	270 V	GEM1	270 V
Transfer 1	800 V	Transfer 1	700 V
GEM2	230 V	GEM2	230 V
Transfer 2	800 V	Transfer 2	700 V
GEM3	288 V	GEM3	320 V
Transfer 3	20 V	Transfer 3	20 V
GEM4	359 V	GEM4	320 V
Induction	800 V	Induction	700 V

Table 12.1: Voltage settings A (left) and B (right) of the OROC [23, 30].

The chamber was then filled with Ne-CO_2-N_2 (90-10-5) and ramped up in steps to 85 %, 90 %, 95 %, 98 % and 100 %. The chamber ran during the first week stable without sparking, then switched to the cascaded power supply. The chamber was again operated without any problems and was further ramped up to 102 %. However, after 5 days, a current of 1 µA appeared in the GEM2 foil of OROC3 which decreased after some time to constant 500 nA, compared to several nA for the other foils. The increased current was attributed to a short induced by a small spike.

The test series continued since most parts of the chamber were still fully functioning. After changing from settings B to settings A with higher fields and increasing the ramping speed, the excessive current of OROC3 GEM2 vanished gradually with each ramping step. This was attributed to a better burning of dust during fast ramping. On the other hand, the operation of the OROC with settings A was only performed up to 98 % of the nominal voltage since at this level OROC1 and OROC3 started to show several spikes. After changing back to settings B, the chamber was again running stably.

The last test of the chamber within the scope of this thesis was the operation during high interaction rate. The rate of ionizing particles in the OROC was increased by a factor of 30. The chamber did not show a current spike in 1/2 h of operation until it was ramped down for safety reasons since the interaction rate was further increased. This proved that the OROC is able to sustain very high rates with settings B.

All in all, the operation of OROC/1 was successful. The chamber was running stably using settings B under nominal conditions and even high interaction rates. The stability issue of settings A is now under investigation. The test in the ALICE pit is planned to be performed for as many OROCs as reasonably possible.

13 Test beam campaign of an IROC

In June 2017, a test beam campaign was executed at the Proton Synchrotron (PS). The aim was to test one GEM based readout chamber under high-rate irradiation of hadrons. For this purpose, an Inner ReadOut Chamber (IROC) of final design, mounted and tested at Yale, was transported to CERN. The main focus was to test the readout electronics for the future GEM TPC and the different powering schemes of the chamber.

The experimental setup consisted of a Cherenkov counter as a reference for the particle identification, two scintillators for the trigger and the IROC in a test box. The incoming particles, pions and electrons with momenta between 1-5 GeV/c, traversed the gas volume parallel to the GEM foils and the pad plane. Since only six fron-end cards were available, only 960 pads were connected to the readout electronics. During the test beam around 260 runs collecting around 2.6 million events were recorded. The data analysis was performed for the first time with the O^2 framework which is the Upgrade of the ALICE Offline Online Computing [31]. One analysis part was the generation of a gain map of the detector, another part was the energy resolution analysis. The gain map did not revealed any unexpected result, the normalized gain had a σ of 5-6 % in two different configurations of the frond-end cards. In the energy resolution analysis, the incoming particles were identified by the Cherenkov counter. Their energy loss was recorded by the IROC. This resulted in two Gaussian distributions of the energy loss for pions and electrons that could be separated by $3.65\,\sigma$.

My contribution in this campaign was the preparation of the power supplies, guiding the power and signal cables and testing the powering system for its high voltage stability up to 5.5 kV. During the beam time, I took shifts to keep the experiment running.

The beam campaign showed the functionality of the GEM based readout chambers in combination with their readout electronics as well as the O^2 framwork which was used the first time for real data analysis. The energy resolution of the IROC was sufficient to separate pions from electrons and the signal uniformity was good as well. The results are promising with regard to the operation in the ALICE TPC since the campaign was the most accurate simulation, yet.

Part III

Conclusion

14 Conclusion

The main achievements of the work during the master thesis were the setting of the test procedure of the readout chambers at GSI and the installation of the test setups in the clean room. Furthermore, two chamber were tested. OROC/0 showed stable behavior and sufficient gain and ion backflow uniformity. However, its energy resolution was worse than required for the operation in the TPC. OROC/1 showed a good performance. The uniformity was satisfying and the stability under high rate was confirmed at LHC, placing the chamber close to the beam line. The energy resolution of the chamber was slightly above the limit.

In the following sections, the key results of the thesis are summarized.

14.1 GEM quality assurance

The GEM foils tested at GSI were working fine for the most part, showing no anomalies in the leakage current measurement. Only two OROC3 foils had to be excluded because of a short or an increased leakage current in one segment. During the thesis, the testing procedure was slightly modified to decrease the risk of a foil damage. The voltage is applied directly without ramping to burn dust. The cleaning of the metallic screws and the surrounding area was standardized to assure that the probability of contamination is set to a minimum.

14.2 Test setup

The scanning test stand inherited from the TRD production is working well for the OROC tests. A remaining issue is the gas monitoring. The two devices used to measure the oxygen content in the gas showed inconsistent values. The problem can be potentially explained by an improper calibration gas for the Rapdidox and a wrong measurement mode of the Orbisphere. The gas monitoring will be approach as soon as the new test boxes are mounted.

14.3 Floating Segments

The localization of a floating segment inside a stack was performed by measuring the current of the individual foils while moving a source along the stack. The foils show an anomaly, mostly a decrease of current, if their segment or one from an overlying foil is floating. In the regular production, however, this method will be replaced by a multimeter capable to measure the foil capacitance sufficiently accurate. The

experience of the first assembled OROCs showed that the resistors on the foils can be damaged during transport or mounting and loose contact without obvious visible indication. This lead to the implementation of to capacitance measurement as an inherent part of the test procedure.

14.4 Energy resolution

The energy resolution of the GEM-based OROC is required to be as good as the resoltion of the current MWPCs. This corrsponds to $\sigma_E/E \leq 12\,\%$. OROC/0 could not fulfill this requirement with energy resolution values for the individual GEM stack between 14 % and 25 %. The gain estimate of OROC/0 revealed that the chamber should be operated at higher gain to provide the nominal gain of 2,000. Less gain results in worse energy resolution. The resolution improve after the adjustment for the OROC2 stack from 25 % to 16 %. The energy resolution of OROC/1 was 11.5 % to 14 %. The problem of the insufficient energy resolution could be potentially addressed adjusting the fields since the ion backflow and the energy resolution of a chamber are competing parameters. This is allow by the good ion-backflow result of around 0.6 %.

14.5 Gain and ion backflow uniformity

The signal uniformity of both chambers was satisfying. The limit of the maximum RMS/mean value of 20 % was never approached. OROC/0 and OROC/1 had an RMS/mean of 18 % and 17 %, respectively. The ion backflow of the OROCs has to be below 1 % for the operation in the ALICE TPC. OROC/0 and OROC/1 had an mean ion backflow of around 0.6 % fulfilling the requirements.

The underlying substructure of the 2-dimensional gain uniformity scans could be explained by the composition of the entrance window of the test box made of honeycomb structure. Simulations studies showed striped pattern in the gain map comparable to the measurements for step sizes of 10 mm and 25 mm, respectively. For a collimator of 5 mm radius, the step sizes do not disturb the signal uniformity in a significant manner. However, one has to be careful using smaller collimators. The simulation studies showed that the contribution to the RMS/mean, coming from the honeycomb, could exceed the intrinsic nonuniformities of the chamber using a collimator with $\varnothing \leq 5\,\text{mm}$.

All in all, the tests showed that both chambers fulfill the requirements. Despite of the appearance of the pattern, the used collimator ($\varnothing = 10\,\text{mm}$) and step size (25 mm in both directions) are preferable for the regular tests. The duration of a test is acceptable and the beating effect of collimator and the structure of the entrance window is negligible. Additionally, our step size is by chance comparable to 1 inch which corresponds to 25.4 mm, the step size used by the US colleagues.

14.6 Stability at high rates

The two chambers proved their capability to sustain high rates. Both chambers were operated successfully in the irradiation tests at GSI where they were irradiated with x-rays to simulated the expected current in the TPC during Run 3. The required $10\,\mathrm{nA/cm^2}$ of induced current at the pad plane could be managed for several hours. However, the test box had to be modified to allow the stable operation. The cathode of the box was discharging to ground and had a high dark current of a few nA. This led to the production of new test boxes for the both assembly institutes and CERN with lift-off cathodes which proved their functionality at GSI. OROC/1 was then tested with the modified test box in the ALICE cavern, placing the chamber close to the beam line. The chamber was operated with HV settings B without discharges, also during high interaction rates . The operation with HV settings A led to some discharges. The instability using these settings is yet not understood and is under investigation.

Part IV

Appendix

A Appendix

A.1 Radioactive source

For the energy resolution and some uniformity tests in chapters 9-11, a collimated ^{55}Fe source was used. ^{55}Fe decays by electron capture to ^{55}Mn and has a half-life of roughly 2.7 yr. It emits x-rays with an energy of around 5-6 keV. The decay rate of the used source was 1.85 GBq.

A.2 Specification of x-ray tube "Svetlana"

These are the specifications of the x-ray tube "Svetlana" used in the gain uniformity test outlined in chapter 10:

Target:	Silver (Ag)
Maximal tube voltage:	10 kV
Power:	0.5 W
Maximal filament voltage:	1.5 V
Maximal filament current:	3.2 A

Table A.1: Specifications of x-ray tube "Svetlana" given by the producer [32].

A.3 Specification of x-ray tube "Mini-X"

These are the specifications of the two x-ray tubes used in the full x-ray irradiation tests outlined in chapter 11:

Target:	Gold (Au)
Output spectrum:	See Fig. A.1
Tube voltage:	10 to 50 kV
Tube current:	min. 5 µA; max. 200 µA
Dose rate:	2.2 Sv/h at 30 cm on axis, 50 kV and 80 µA
Approximated flux:	2.2×10^6 $(\mathrm{s} \cdot \mathrm{mm}^2)^{-1}$
Continous output power:	4 W at 100 % duty cycle
Output cone angle	120° (Fig. A.2)

Table A.2: Specifications of x-ray tube "Mini-X" given by the producer [33].

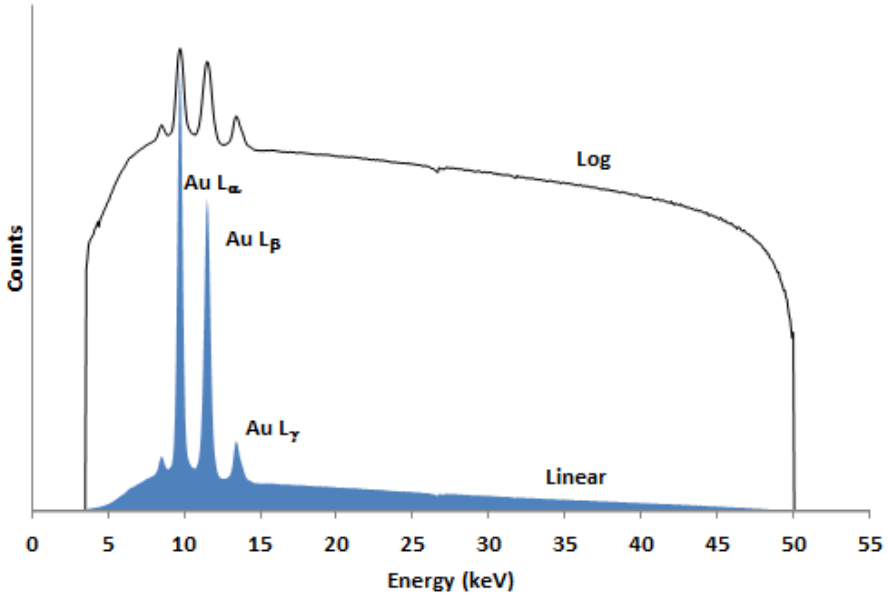

Figure A.1: Output spectrum of Mini-X given by producer [33].

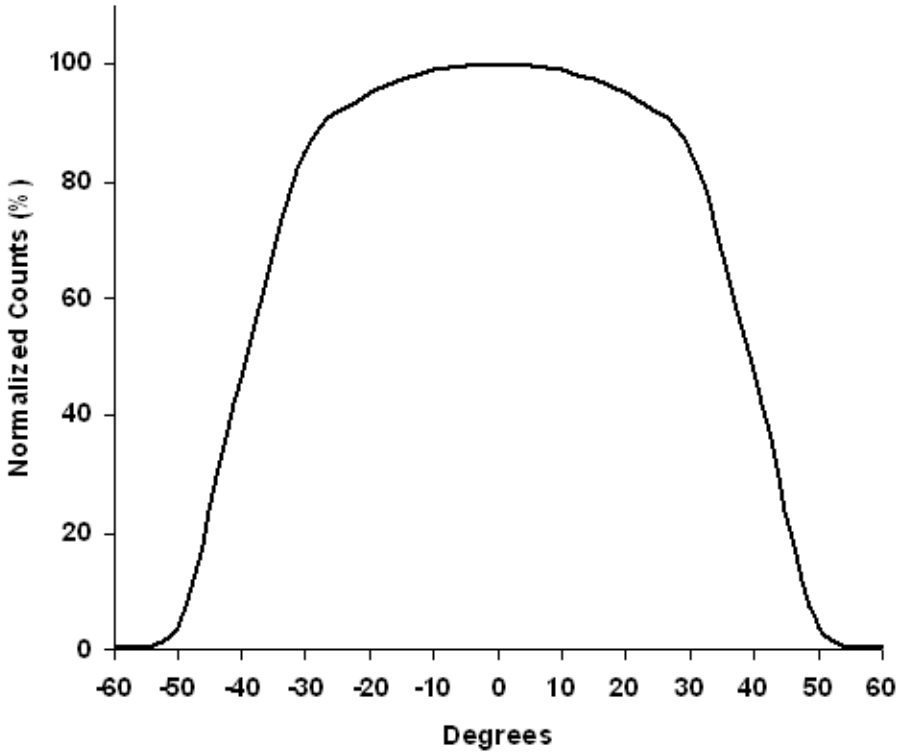

Figure A.2: Angular response of Mini-X given by producer [33].

B Bibliography

[1] J. Adams, M.M. Aggarwal *et al.* *Experimental and theoretical challenges in the search for the quark–gluon plasma: The STAR Collaboration's critical assessment of the evidence from RHIC collisions.* Nuclear Physics A, **757**, 1: pp. 102 – 183, **2005**.

[2] A. Andronic. *The study of quark-gluon matter in high-energy nucleus-nucleus collisions.* In *EXOTIC NUCLEI AND NUCLEAR/PARTICLE ASTROPHYSICS (IV): FROM NUCLEI TO STARS*, volume 1498 of *AIP Conference Proceedings*, (pp. 125–133). **2012**.

[3] A. Bazavov, T. Bhattacharya *et al.* *The chiral and deconfinement aspects of the QCD transition.* **2011**. arXiv:1111.1710.

[4] E. Iancu. *Theory summary for ISMD2000.* In *Proceedings, 40th International Symposium on Multiparticle Dynamics (ISMD 2010): Antwerp, Belgium, September 21-25, 2010*, (pp. 411–437). **2011**. arXiv:1105.0751.

[5] J. Adam, D. Adamová *et al.* (ALICE Collaboration). *Centrality Dependence of the Charged-Particle Multiplicity Density at Midrapidity in Pb-Pb Collisions at* $\sqrt{s_{NN}} = 5.02$ TeV. *Phys. Rev. Lett.*, **116**, **2016**.

[6] *Performance of the ALICE experiment at the CERN LHC.* International Journal of Modern Physics A, **29**, 24, **2014**.

[7] A. Andronic. *Experimental results and phenomenology of quarkonium production in relativistic nuclear collisions.* **2014**. arXiv:1409.5778.

[8] M. Connors, C. Nattrass *et al.* *Review of Jet Measurements in Heavy Ion Collisions*, **2017**. arXiv:1705.01974.

[9] *CERN Accelerator Complex.* http://www.stfc.ac.uk/research/particle-physics-and-particle-astrophysics/large-hadron-collider/cern-accelerator-complex/. Accessed: 2017-08-01.

[10] *3D ALICE Schematic - with Description.* https://aliceinfo.cern.ch/Figure/sites/aliceinfo.cern.ch.Figure/files/Figures/General/jthaeder/2012-Aug-02-ALICE_3D_v0_with_Text.jpg. Accessed: 2017-09-08.

[11] P. Cortese *et al.* (ALICE). *ALICE technical design report on forward detectors: FMD, T0 and V0.* **2004**.

[12] R. Schicker (ALICE). *Overview of ALICE results in pp, pA and AA collisions. EPJ Web Conf.*, **138**, **2017**. arXiv:1701.04810.

[13] M. Floris. *Overview of ALICE Results. Journal of Physics: Conference Series*, **668**, 1, **2016**.

[14] *Upgrade of the ALICE Time Projection Chamber.* Technical report, **2013**.

[15] C. Lippmann and ALICE TPC Collaboration. *A continuous read-out TPC for the ALICE upgrade. Nuclear Instruments & Methods in Physics Research Section A-Accelerators Spectrometers and Associated Equipment*, **824**: pp. 543–547, **2016**.

[16] H. Kolanoski and N. Wermes. *Teilchendetektoren.* Springer Spektrum, **2016**.

[17] R. Veenhof. *Choosing a gas mixture for the ALICE TPC.* **2003**.

[18] G. CHARPAK and F. SAULI. *High-resolution electronic particle detectors. Annual Review of Nuclear and Particle Science*, **34**: pp. 285–349, **1984**.

[19] F. Sauli. *The gas electron multiplier (GEM): Operating principles and applications. Nuclear Instruments and Methods in Physics Research Section A: Accelerators, Spectrometers, Detectors and Associated Equipment*, **805**: pp. 2 – 24, **2016**.

[20] M. Blatnik, K. Dehmelt *et al. Performance of a Quintuple-GEM Based RICH Detector Prototype.* **2015**. arXiv:1501.03530.

[21] C. Altunbas, M. Capéans *et al. Construction, test and commissioning of the triple-gem tracking detector for compass. Nuclear Instruments and Methods in Physics Research Section A: Accelerators, Spectrometers, Detectors and Associated Equipment*, **490**, 1: pp. 177 – 203, **2002**.

[22] The ALICE collaboration. *Space-charge distortion measurements and their calibration in the ALICE TPC.* https://indico.cern.ch/event/587756/attachments/1370525/2078384/TPC_distortions_summary_Nov_11.pdf, **2016**. Internal document, accessed: 2017-09-28.

[23] The ALICE collaboration. *Readout chamber production, Part I, Final Readout Chambers characterization.* https://indico.cern.ch/event/617818/contributions/2493327/attachments/1422943/2186698/gasik_PRR_PART_I.pdf, **2017**. Internal document, accessed: 2017-08-21.

[24] *Rapidox 3100 Multigas Analyser*. http://www.cambridge-sensotec.co.uk/products/rapidox-3100-gas-analyser/. Accessed: 2017-10-02.

[25] *3600 Analyzer for Oxygen Operator's Manual*. http://apps.watersurplus.com/techlib/Orbisphere/Orbisphere_Analyzer_3600_om_D803.pdf. Accessed: 2017-10-02.

[26] M. Alfonsi, G. Croci *et al.* *Simulation of the dielectric charging-up effect in a GEM detector*. *Nuclear Instruments and Methods in Physics Research Section A: Accelerators, Spectrometers, Detectors and Associated Equipment*, **671**: pp. 6 – 9, **2012**.

[27] ALICE Collaboration. *The ALICE Transition Radiation Detector: construction, operation, and performance*, **2017**. arXiv:1709.02743.

[28] R. Brun and F. Rademakers. *ROOT — An object oriented data analysis framework*. *Nuclear Instruments and Methods in Physics Research Section A: Accelerators, Spectrometers, Detectors and Associated Equipment*, **389**, 1: pp. 81 – 86, **1997**.

[29] T. Caudron for the ALICE collaboration, **2017**.

[30] The ALICE collaboration. *Testbeam May 2017 – Pedestal, noise and pulser analysis*. https://indico.cern.ch/event/653116/contributions/2701891/attachments/1513895/2362265/Testbeam_may_2017_-_pedestals_and_noise.pdf, **2017**. Internal document, accessed: 2017-10-04.

[31] P. Buncic, M. Krzewicki and P. Vande Vyvre. *Technical Design Report for the Upgrade of the Online-Offline Computing System*. Technical report, **2015**.

[32] *Svetlana X-Ray: X-ray spectroscopy tubes with transmitting target design*. http://www.svetlana-x-ray.ru/production-list-eng.html?cid=15. Accessed: 2017-08-12.

[33] *Amptek - Mini-X X-Ray Tube System for XRF*. http://amptek.com/products/mini-x-ray-tube/#4. Accessed: 2017-08-10.

B.1 List of Figures

1.1 Collision of two nuclei in space-time picture [4]. 8

2.1 CERN accelerator complex [9]. 10
2.2 The ALICE detector system [10] 11
2.3 Particle Identification by the energy loss dE/dx in the ALICE TPC [12]. 12
2.4 Schematic view of the ALICE TPC [14]. 14

3.1 Schematic representation of a TPC [16] 17
3.2 MWPC based readout of an OROC in the ALICE TPC. In an IROC the distance between pads and anode wires, as well as between anode and cathode wires is reduced to 2 mm. (Adopted with kind approval from Julius Gronefeld) 18
3.3 Electrical field inside GEM holes and a microscope image of a cut GEM [19] 19

4.1 One full sector of the ALICE TPC (IROC and OROC) is equipped by four GEM stacks [15]. 23
4.2 Cross section of a GEM foil where holes are etched with single-mask technique. 24
4.3 Segmentation of a OROC3 foil into 24 segments. 24
4.4 Segmented side of GEM foil of an OROC3 stack. 25
4.5 Exploded view of an OROC [14]. 26
4.6 GEM frame for OROC1 foil with supporting cross. 27
4.7 Shorting cards connecting all pads of the OROC. 28
4.8 Relation between ion backflow and energy resolution for a quadruple GEM stack in Ne-CO_2-N_2 (90-10-5) [14]. 29

5.1 Material flow for the readout chambers in the ALICE TPC upgrade project 31

6.1 Drawer for the leakage current test of OROC3 foils. 33
6.2 Leakage current measurement of a bad GEM foil (one segment with a short). 35
6.3 Leakage current measurement of a bad GEM foil (one segment with increased current). 35
6.4 Leakage current measurement of well functioning GEM foil. 36

8.1 Evolution of pad current under irradiation 40
8.2 Measurement of GEM1 Top current of the OROC/0 to find floating segments. 41
8.3 Measurement of GEM4 Top current of the OROC/0 to find floating segments. 42
8.4 Loose resistor of segment 3 of GEM4 in the OROC/0. 42

9.1 Gain curve of the OROC/0. 45
9.2 Gain curve of the OROC/1. 46
9.3 Voltage dependence of rate 47
9.4 Shape of ^{55}Fe spectrum 48
9.5 Energy resolution of the three GEM stacks of OROC/0. 50
9.6 Energy resolution of OROC2 of the OROC/0 with adjusted voltage . 51
9.7 Energy resolution of the three GEM stacks of OROC/1 chamber. . . 52

10.1 OROC on test stand for uniformity and resolution measurements. . . 54
10.2 Gain uniformity scan of OROC/0. 56
10.3 Pad current distribution of OROC/0. 57
10.4 Ion backflow distribution of OROC/0. 58
10.5 Gain uniformity scan of OROC/1. 59
10.6 Pad current distribution of OROC/1. 60
10.7 Ion backflow distribution of OROC/1. 61
10.8 Substructure pad current revealed in live-monitoring 62
10.9 Fine uniformity scan of outermost part of OROC3 stack of OROC/1. 62
10.10 Fine uniformity scan of part of OROC2 stack of OROC/1 after rotation. 63
10.11 Honeycomb plates of different size. 63
10.12 Fine uniformity scan of OROC/1, decreased step size (5 mm). 64
10.13 Uniformity scan of OROC/1 resolving honeycomb. 64
10.14 Simulated hexagonal structure with different wall thicknesses 65
10.15 Simulated circular collimators of different diameters. 66
10.16 Comparison of measurement and simulations of fine scan resolving honeycomb structure. 67
10.17 Measurement and simulation of uniformity scan. Step size = 25 mm, collimator diameter = 10 mm. 68
10.18 Simulation and measurement of uniformity scan. Step size = 10 mm, collimator diameter = 5 mm. 69

11.1 Functional sketch of the x-ray irradiation test setup. 71
11.2 Shielding box for x-ray irradiation tests. 72
11.3 Optional passepartout to restrict irradiation area. 72
11.4 Sketch of test box with two cathodes. 74
11.5 Pad current of the OROC/1 during irradiation test with suspended current. 75
11.6 Pad current of the OROC/1 during irradiation test with suspended current and reduced voltage for old cathode. 75

12.1 OROC placed in miniframe of ALICE experiment. 76

A.1 Output spectrum of Mini-X given by producer [33]. 86
A.2 Angular response of Mini-X given by producer [33]. 86

B.2 List of Tables

4.1 Voltage settings A of the OROC. 27

7.1 Relation between gas inflow and oxygen limit 37

10.1 Overview of all uniformity scans performed with OROC/0 and OROC/1. 55
10.2 RMS/mean values for simulated uniformity scans varying the step size. 69
10.3 RMS/mean values for simulated uniformity scans varying the collimator diameter. 70

12.1 Voltage settings A and B of the OROC. 77

A.1 Specifications of x-ray tube “Svetlana” given by the producer [32]. . . 85
A.2 Specifications of x-ray tube “Mini-X” given by the producer [33]. . . . 85

Erklärung:

Ich versichere, dass ich diese Arbeit selbstständig verfasst habe und keine anderen als die angegebenen Quellen und Hilfsmittel benutzt habe.

Heidelberg, den 16.10.2017 .....